5-2022

Synthesis and characterization of organometallic complexes for biological imaging

Emily Stumbo
University of Tennessee at Chattanooga, zcx624@mocs.utc.edu

Recommended Citation

Stumbo, Emily, "Synthesis and characterization of organometallic complexes for biological imaging" (2022). *Honors Theses.*

Synthesis and Characterization of Organometallic Complexes for Biological Imaging

Emily Stumbo

Departmental Honors Thesis
University of Tennessee at Chattanooga
Department of Chemistry and Physics

Examination Date: April 11, 2022

Jared A. Pienkos	John P. Lee
Assistant Professor of Chemistry	Associate Professor of Chemistry
Thesis Director	Department Examiner

Tom Rybolt
UC Foundation Professor of Chemistry
Department Examiner

Abstract

Luminescent transition metal complexes are of interest for biological imaging applications due to their unique photophysical properties including large Stokes shift, long fluorescence lifetimes, and tunable emission. Altering ligand structure is a useful way to manipulate the charge transfer (CT) and mixed character states that give these complexes their photophysical properties. A series of organometallic complexes containing ligands with externally facing nitrogens has been prepared and synthesized. Complexes of the form Pt (II)(^{t}bbpy)(C_2-py), $Re(CO)_3$(N^N), Ir(C^N)$_2$(N^N), and Ir(C^N)$_2$(N^O) have been studied for their potential application as biological imaging agents. The goal of this project is to compare the properties of these complexes to analogs where the external nitrogen has bonded to an oxygen to assess their potential as ratiometric hypoxia (low oxygen concentration) probes. Two cyclometalated iridium complexes, Ir(ppy)$_2$(5-Me-pz-COO) and Ir(dfppy)$_2$(5-Me-pz-COO) were synthesized along with their N-oxide congeners. It was found that the presence of an N-oxide caused a 140 mV cathodic shift in the reduction potential. For Ir(ppy)$_2$(5Me-pz-COO), the N-oxide caused a 20 nm red-shift in emission and a significant quenching of emission intensity. These data show promising results for the ability of the N-oxide to tune the properties of the complexes. This report details the successful synthesis of several additional complexes that show potential for this application.

Table of Contents

Glossary

^{t}bbpy	4,4’-*tert*-butyl-2,2’-bipyridine
dmap	4-dimethylamino pyridine
pz	pyrazine
bpz	bipyrazine
phen	1,10’ phenanthroline
dfppy	difluorophenyl pyridine
ppy	phenyl pyridine
biq	biquinoline
5-Me-pz-2-COOH	5-methyl pyrazine 2-carboxylic acid
5-Me-pzO-2-COOH	5-methyl-4-oxo pyrazine 2-carboxylic acid
4-NMe$_2$-pzO-2-COOH	4-dimethylamino pyrazine 2-carboxylic acid
pz-COO	pyrazine-2-carboxylic acid
$C_2$3-py	3-ethynyl pyridine
$C_2$2-py	2-ethynyl pyridine
m-CPBA	*meta*-Chloroperoxybenzoic acid

Chapter 1: Hypoxia Imaging and the Design of Organometallic Imaging Agents

1.1 Hypoxia Imaging

An important aspect of medicine is the diagnosis of conditions and detection of harmful substances within the body in a noninvasive manner. Common imaging techniques such as X-ray and magnetic resonance imaging allow us to visualize larger conditions in a clinical setting but not subcellular dynamics.[1] There are many subcellular dynamics that are indicators or causative agents of disease, but they can be difficult to identify before the problem is widespread and irreversible (e.g., cancer). Synthesis of small molecule probes is a large field of chemistry, and fluorescence is a common mechanism used to visualize intracellular processes such as the movement of small molecules, metabolites, and enzyme interactions.[2] These probes typically function through measurement of fluorescent intensity, reflecting a concentration or by changing emission via intermolecular interactions.

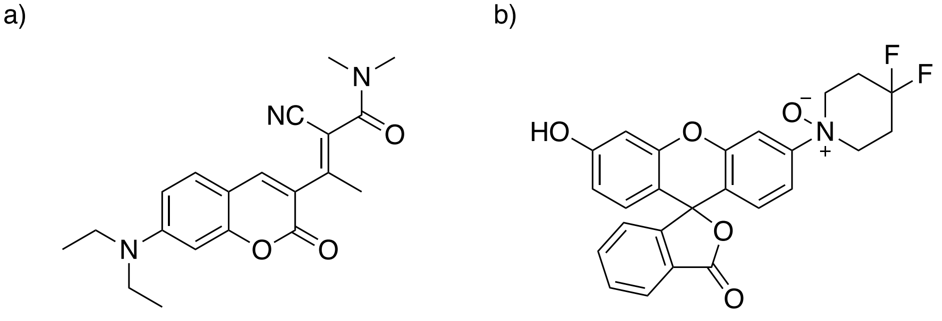

QG-1

H-FluNox

Figure 1: Fluorescent Probes for in vivo imaging. a) Reversible ratiometric probe to monitor Glutathione (GSH) via Michael addition-elimination.[3] b) Probe for labile heme that fluorescence upon N-oxide cleavage.[10]

A field that encompasses the wide range of uses for *in vivo* imaging is the study of heme biosynthesis and trafficking.[4] This ubiquitous macromolecule consisting of Fe(II) chelated to a protoporphyrin IX ring is an essential protein cofactor and signaling molecule, and many diseases are associated with disruption or upregulation of heme biosynthesis. Thus, researchers have been developing methods to image heme for decades to understand its dynamics on a subcellular level.[5] This is often accomplished through genetically encoded protein-based fluorescent sensors.[6, 7] Fluorescent small molecule probes allow for direct cellular uptake. These probes are often reaction-dependent where fluorescence is either quenched or “turned on” by a reaction with the desired biomarker (e.g., H-FluNox sensor or labile heme [Figure 1]).[8-10]

Similar in importance to heme, oxygen is vital for cells; it acts as a signaling molecule and plays a role in much of the redox chemistry inside cells. Hypoxia (i.e., low oxygen) is a common marker of potentially cancerous cells or tumor malignancy.[11] Growing tumors have complex but disordered vascular networks that inherently decrease the transport of O_2 throughout the tumor, causing hypoxia. These conditions select for cells that have several enhanced hypoxia-survival mechanisms, including the inactivation of some regulatory mechanisms controlling growth transcription factors, which increases the probability of malignancy and tumor proliferation.[12] Hypoxia also presents a clinical concern because of its ability to limit the effectiveness of cancer therapy through characteristics like resistance to apoptosis (i.e. cell death) and genomic instability.[13] Thus, there are many reasons we want to be able to detect hypoxic conditions within cells.

There are currently few ways to image hypoxia in clinical settings. Fluorine-labeled nitroimidazoles can be transported to a tumor by the blood stream and imaged with Positron Emission Tomography (PET). Similarly, a contrast agent can be distributed throughout the tumor and imaged by Magnetic Resonance (MR) or Computed Tomography (CT).[11] The problem with these methods is there is no way to ensure sufficient and uniform distribution throughout the tumor, it can take hours to obtain a useful image, and they are often not directly measuring intracellular oxygenation.[11] Thus, small-molecule probes and alternative imaging techniques such as fluorescence and photoacoustic imaging present a possibly more sensitive and reliable way to detect hypoxia for both diagnostic and treatment monitoring applications. Of particular interest to this project is the report of an aza-BODIPY probe that employs an N-oxide functional group to detect hypoxic conditions within tumor cells [Figure 2].[14]

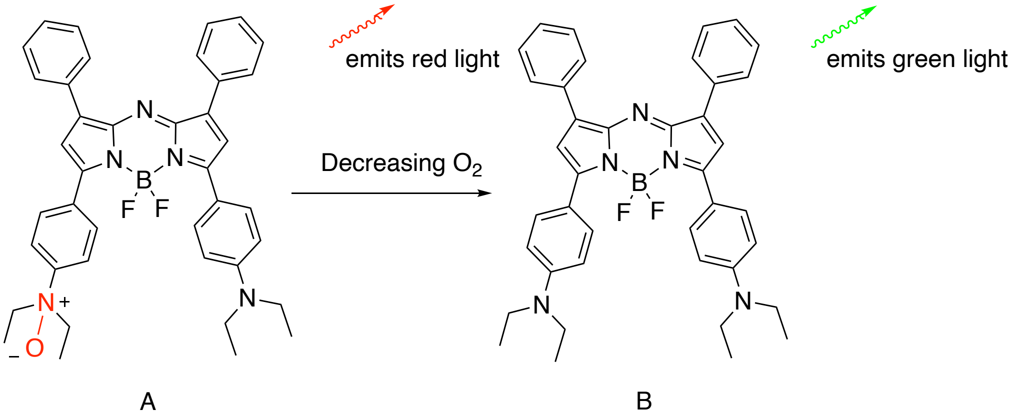

Figure 2: Altered emission of aza-BODIPY probe in response to decreasing oxygen.

Under hypoxic conditions, some heme-bound proteins will cleave the N-O bond, resulting in a change in emission from red to green and an enhanced photoacoustic signal (PA). Oxygen inside the cells competitively binds to these proteins, and so normoxic conditions will leave the probe relatively unchanged. This study used ratiometric photoacoustic imaging, a technique that has grown in popularity with respect to biological imaging due to the excellent resolution of signal it can produce and its ability to penetrate deeper in tissue.[15] Imaging techniques will be covered in more detail in a later section.

There are many factors to consider when designing a fluorescent probe for *in vivo* imaging even before clinical applications are considered. If the target biomarker is inside a cell, the probe must be permeable to a membrane, which requires balancing hydrophilic and hydrophobic structural elements. There are many reactive species in cells, so the probe needs to be selective for the specific biomarker and resistance to degradation inside the cell. The fluorescent heme probe discussed previously, for example, reacts selectively with labile heme rather than Fe (II) alone or protein-bound heme, making it an effective probe for monitoring trafficking of a specific form of the molecule.[9] For the N-oxide based probe [Figure 1], groups around the N were necessary to prevent the probe from being reduced by other reactive species.[14] Toxicity, the interference with cell viability, is also an important consideration. In addition to cellular considerations, the photophysical properties such as absorbance and emission wavelengths suitable for the type of instrumentation and fluorescence lifetimes are integral to functionality. Screening a series of probes with small variations in ligand structure that may tune its properties is often the best way to find a viable probe.

1.2 Organometallic Imaging Applications

Transition metal compounds are of interest in biological imaging due to the ability to tune their photophysical properties. Organometallic compounds containing heavy metals have several characteristics that make them promising fluorescent probes. Stokes shift, the phenomenon in which a compound emits at a longer wavelength than the wavelength it absorbs due to energy loss during non-radiative transitions such as vibrational relaxation and intersystem crossing (ISC). A large Stokes shift is beneficial for imaging applications because prevents self-quenching (reabsorption of emitted light), which will result in weaker fluorescence signal.[14] Organometallic complexes exhibit large Stokes shifts, usually into the visible region, because of the complex mixture of excited states controlling their photophysical properties.[15, 17]

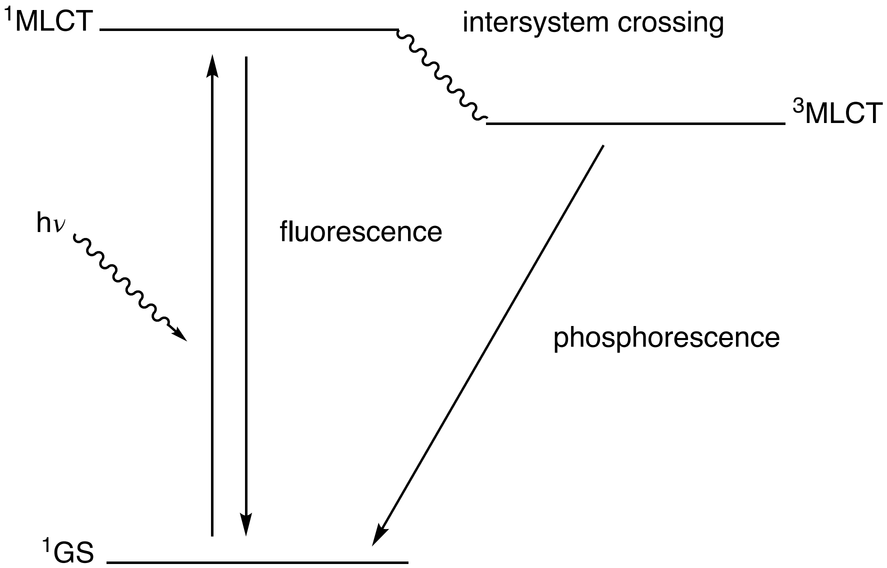

Figure 3: Qualitative Jablonski diagram for MLCT transitions in organometallic complexes.

Relaxation from a triplet metal-to-ligand charge transfer (^{3}MLCT) excited state is usually responsible for the Stokes shift because energy is lost during intersystem crossing (change in spin states); this transition also occurs more slowly, resulting in longer fluorescent lifetimes.[16] [Fig. 3] This is useful for imaging because it allows for time-gated measurement, which can filter out background signal caused by the autofluorescence of other cell components.[17]

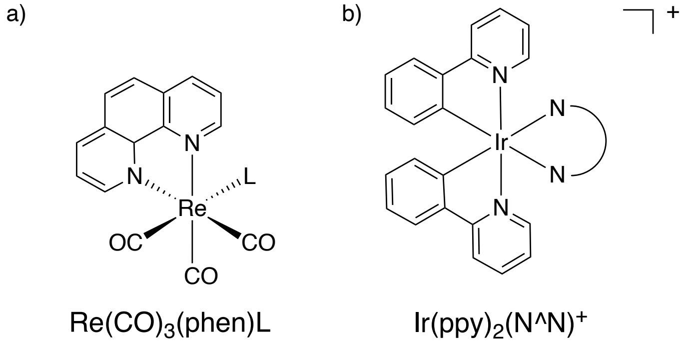

a) $Re(CO)_3(phen)L$ b) $Ir(ppy)_2(N^\wedge N)^+$

Figure 4: Representative structures of luminescent Ir(III) and Re(I) Complexes

Changing or altering the ligands attached to the metal center presents a simple way to tune the properties of ligands because in addition to MLCT states, these complexes also exhibit ligand-to-ligand charge transfer (LLCT), intraligand (IL), and ligand field (LF) transitions.[18] This report will focus on the change in electronics and optical properties of iridium and rhenium compounds caused by various ligands.[Fig. 4] The photophysics of organometallic complexes containing these metals have been studied extensively for various applications, but d^6 *fac*-$Re(CO)_3(N^\wedge N)Cl$ and cyclometalated iridium complexes [Fig. 4] have been the focus of biological imaging interest.[19] The covalency of the metal-carbon prevents reactive species in the cell from attacking the heavy metal, which has large cytotoxic potential when it is not saturated.[20] It has been shown that multiple ligands on the metal center influence the absorption and emission profiles of these compounds, which mean there are multiple places on the molecule that could be used to tune the emission. It should be noted that the correct term for a radiative transition from a triplet state is phosphorescent; however, since fluorescence spectroscopy is the technique used and the exact states involved in emission is not precisely know, the term fluorescence will be used for clarity throughout this report. The main goal of this project is to analyze the change in properties caused by the addition of an oxygen to uncoordinated nitrogens on the ligands of the organometallic complexes shown in Figure 5.

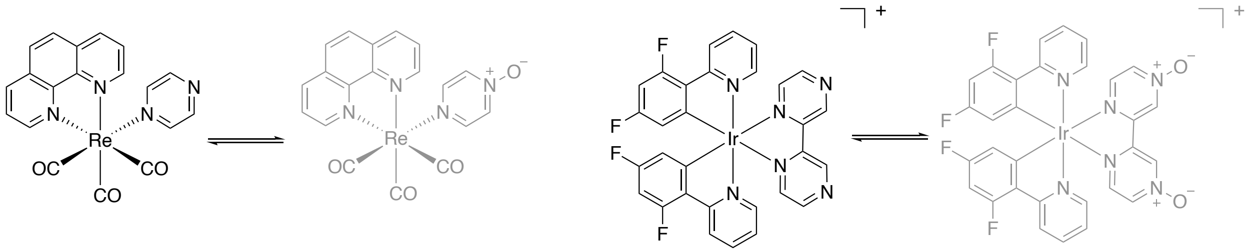

$Re(CO)_3(phen)(pz)$ $Re(CO)_3(phen)(pzO)$ $Ir(dfppy)_2(bpz)$ $Ir(dfppy)_2(bpzO)$

Figure 5: Theoretical Re(I) and Ir(III) N-oxide probes.

1. 3 *Utility of N-oxide and ligand design.*

Since their first reported synthesis in 1926, pyridine N-oxides have been extensively studied.[21] Their electrophilic and nucleophilic properties are useful for efficient synthesis of substituted pyridines (e.g., amination[22], sulfurylation[23], alkylation[24], etc.) and natural products and therapeutic agents used for the treatment of anxiety disorders, alopecia and cancer.[25] [Fig. 6] Since nitric oxide is an essential molecule for cells, these compounds act by mimicking NO to competitively bind to inhibitors The complex design of these drugs is outside the scope of this project, but the plethora of biologically active molecules containing N-oxides show its utility. Although not an imaging agent, Tirapazamine [Fig. 6c] provides a conceptual link between N-oxides and hypoxia in tumor cells; in low oxygen environments, the N-oxide triggers reductases that convert the drug into a radical species that damages DNA.[26] Being able to image hypoxia in tumor cells would allow for more targeted drug delivery.

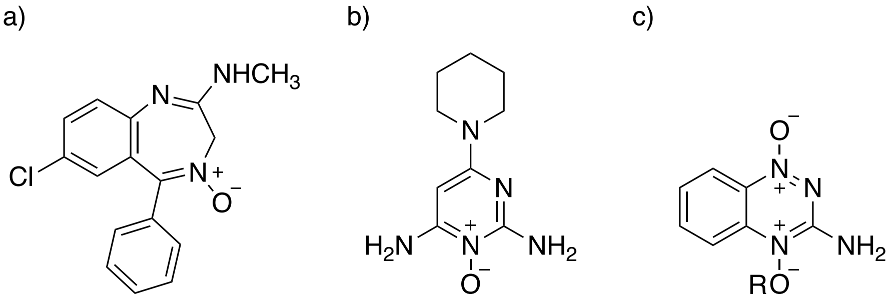

Chlorodiazepoixde Minoxidil Tirapazamine

Figure 6: N-oxide therapeutic agents

When designing a biological probe rather than a therapeutic, it is important the molecule not be converted into a radical, cytotoxic species. As discussed previously, N-oxide bonds have been utilized for imaging applications. Both the H-FluNox heme probe [Fig.1] and aza-BODIPY hypoxia probe [Fig. 2] use the reduction of a tertiary amine oxide to change the fluorescent signal.[8, 9, 14] The goal of this project is to combine the utility of N-oxides with the ideal photophysical properties of the organometallic transition metal discussed in the previous sections to make a probe that will be tuned in hypoxic conditions. Subsequent chapters will detail the synthesis and characterization of these complexes containing ligands with an external, uncoordinated nitrogen to which an oxygen can bind. Many of the ligands used for this project contained pyridine-like components. A typical synthetic route to pyridine oxides is through oxidation via *meta*-Chloroperoxybenzoic acid (*m*-CPBA).[24] [Fig. 7]

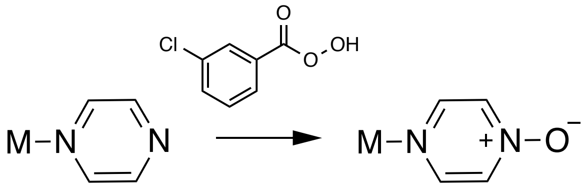

Figure 7: Synthetic approach for organometallic N-oxide formation.

This general approach was attempted with both of the TM complexes shown in Figure 4. We can determine the viability of these complexes as probes through the comparison of the photophysical properties of the non-N-oxide complex and its N-oxide congener.

4. Ratiometric Imaging

Measuring fluorescence is an ideal method for biological imaging because it is sensitive and relatively simple. The long history of research involving fluorescence of molecules provides a library of fluorophores to utilize when designing a fluorescent probe, but it is also important to consider what kind of signal will be measured and its functionality *in vivo*. Measuring fluorescent intensity at one wavelength is easy, but the signal does not account for interferences such as light scattering, microenvironments within the cell, and variations from the excitation source)[27]. Additionally, the concentration of the probe must be known to make quantitative measurements, which can be difficult *in vivo*. Ratiometric imaging involves measuring the fluorescence intensity at two wavelengths. It is useful because it is self-referencing, meaning one signal acts as an internal reference; this improves sensitivity and quantification.[15] Ratiometric measurements can be accomplished through several strategies. The probe can contain subunits where one unit is sensitive to the target biomarker and the other signal is independent of the biomarker. Alternatively, the signal of the probe be altered in response to the analyte through proton transfer, conformation changes, chemical reactions, etc, creating two emission wavelengths to measure or an on/off signal due to quenching.[9, 27-29] Combined with a sensitive cell imaging technique such as confocal fluorescence microscopy, variations in biomarker concentrations across cells can be visualized.[8]

Another promising use of ratiometric imaging *in vivo* is the measurement of photoacoustic signals. Photoacoustic imaging (PAI), which involves excitation of a chromophore that absorbs in the near-IR; that energy causes thermoelastic expansion, which is released in the form of ultrasound waves, producing an acoustic signal.[30] This imaging method is useful for biological imaging because there is less optical scattering and deeper tissue penetration.[30, 31]PAI has been utilized for cancer imaging for many years, including aza-BODIPY probe discussed earlier, which used PAI for sensitive hypoxia imaging.[14] Although the probes discussed in this project would not be suitable for PAI, the problems it addresses are important considerations for any *in vivo* probe. Recently, multi-modal approaches combining fluorescence and photoacoustic imaging to detect biomarkers show promising results.

References

1. Kherlopian, A. R.; Song, T.; Duan, Q.; Neimark, M. A.; Po, M. J.; Gohagan, J. K.; Laine, A. F., A review of imaging techniques for systems biology. *BMC Syst Biol* **2008,** *2*, 74-74.10.1186/1752-0509-2-74
2. Jiao, X.; Li, Y.; Niu, J.; Xie, X.; Wang, X.; Tang, B., Small-Molecule Fluorescent Probes for Imaging and Detection of Reactive Oxygen, Nitrogen, and Sulfur Species in Biological Systems. *Analytical Chemistry* **2018,** *90* (1), 533-555.10.1021/acs.analchem.7b04234
3. Liu, Z.; Zhou, X.; Miao, Y.; Hu, Y.; Kwon, N.; Wu, X.; Yoon, J., A Reversible Fluorescent Probe for Real-Time Quantitative Monitoring of Cellular Glutathione. *Angew Chem Int Ed Engl* **2017,** *56* (21), 5812-5816.10.1002/anie.201702114
4. Poulos, T. L., Heme Enzyme Structure and Function. *Chemical Reviews* **2014,** *114* (7), 3919-3962.10.1021/cr400415k
5. Yuan, X.; Rietzschel, N.; Kwon, H.; Nuno, A. B. W.; Hanna, D. A.; Phillips, J. D.; Raven, E. L.; Reddi, A. R.; Hamza, I., Regulation of intracellular heme trafficking revealed by subcellular reporters. *Proceedings of the National Academy of Sciences* **2016,** *113* (35), E5144-E5152.doi:10.1073/pnas.1609865113
6. Hanna, D. A.; Harvey, R. M.; Martinez-Guzman, O.; Yuan, X.; Chandrasekharan, B.; Raju, G.; Outten, F. W.; Hamza, I.; Reddi, A. R., Heme dynamics and trafficking factors revealed by genetically encoded fluorescent heme sensors. *Proceedings of the National Academy of Sciences* **2016,** *113* (27), 7539-7544.doi:10.1073/pnas.1523802113
7. Song, Y.; Yang, M.; Wegner, S. V.; Zhao, J.; Zhu, R.; Wu, Y.; He, C.; Chen, P. R., A Genetically Encoded FRET Sensor for Intracellular Heme. *ACS Chemical Biology* **2015,** *10* (7), 1610-1615.10.1021/cb5009734
8. Xu, S.; Liu, H.-W.; Chen, L.; Yuan, J.; Liu, Y.; Teng, L.; Huan, S.-Y.; Yuan, L.; Zhang, X.-B.; Tan, W., Learning from Artemisinin: Bioinspired Design of a Reaction-Based Fluorescent Probe for the Selective Sensing of Labile Heme in Complex Biosystems. *Journal of the American Chemical Society* **2020,** *142* (5), 2129-2133.10.1021/jacs.9b11245
9. Kawai, K.; Hirayama, T.; Imai, H.; Murakami, T.; Inden, M.; Hozumi, I.; Nagasawa, H., Molecular Imaging of Labile Heme in Living Cells Using a Small Molecule Fluorescent Probe. *Journal of the American Chemical Society* **2022,** *144* (9), 3793-3803.10.1021/jacs.1c08485
10. Hirayama, T., Development of Chemical Tools for Imaging of Fe(II) Ions in Living Cells: A Review. *Acta Histochem Cytochem* **2018,** *51* (5), 137-143.10.1267/ahc.18015
11. Lyng, H.; Malinen, E., Hypoxia in cervical cancer: from biology to imaging. *Clin Transl Imaging* **2017,** *5* (4), 373-388.10.1007/s40336-017-0238-7
12. Vaupel, P., The Role of Hypoxia-Induced Factors in Tumor Progression. *The Oncologist* **2004,** *9* (S5), 10-17.10.1634/theoncologist.9-90005-10
13. Wilson, W. R.; Hay, M. P., Targeting hypoxia in cancer therapy. *Nature Reviews Cancer* **2011,** *11* (6), 393-410.10.1038/nrc3064
14. Knox, H. J.; Kim, T. W.; Zhu, Z.; Chan, J., Photophysical Tuning of N-Oxide-Based Probes Enables Ratiometric Photoacoustic Imaging of Tumor Hypoxia. *ACS chemical biology* **2018,** *13* (7), 1838-1843.10.1021/acschembio.8b00099
15. Gui, R.; Jin, H.; Bu, X.; Fu, Y.; Wang, Z.; Liu, Q., Recent advances in dual-emission ratiometric fluorescence probes for chemo/biosensing and bioimaging of biomarkers. *Coordination Chemistry Reviews* **2019,** *383*, 82-103.https://doi.org/10.1016/j.ccr.2019.01.004

16. Ruggiero, E.; Alonso-de Castro, S.; Habtemariam, A.; Salassa, L., The Photochemistry of Transition Metal Complexes and Its Application in Biology and Medicine. In *Luminescent and Photoactive Transition Metal Complexes as Biomolecular Probes and Cellular Reagents*, Lo, K. K.-W., Ed. Springer Berlin Heidelberg: Berlin, Heidelberg, 2015; pp 69-107.
17. Fluorescence Sensing. In *Principles of Fluorescence Spectroscopy*, Lakowicz, J. R., Ed. Springer US: Boston, MA, 2006; pp 623-673.
18. Kumar, A.; Sun, S.-S.; Lees, A. J., Photophysics and Photochemistry of Organometallic Rhenium Diimine Complexes. In *Photophysics of Organometallics*, Lees, A. J., Ed. Springer Berlin Heidelberg: Berlin, Heidelberg, 2010; pp 37-71.
19. Lo, K. K.-W., Exploitation of Luminescent Organometallic Rhenium(I) and Iridium(III) Complexes in Biological Studies. In *Photophysics of Organometallics*, Lees, A. J., Ed. Springer Berlin Heidelberg: Berlin, Heidelberg, 2010; pp 73-114.
20. Thorp-Greenwood, F. L.; Balasingham, R. G.; Coogan, M. P., Organometallic complexes of transition metals in luminescent cell imaging applications. *Journal of Organometallic Chemistry* **2012,** *714*, 12-21.https://doi.org/10.1016/j.jorganchem.2012.01.020
21. Belova, N. V.; Pimenov, O. A.; Kotova, V. E.; Girichev, G. V., Molecular structure and electron distribution of 4-nitropyridine N-oxide: Experimental and theoretical study of substituent effects. *J Mol Struct* **2020,** *1217*, 128476-128476.10.1016/j.molstruc.2020.128476
22. Londregan, A. T.; Jennings, S.; Wei, L., Mild Addition of Nucleophiles to Pyridine-N-Oxides. *Organic Letters* **2011,** *13* (7), 1840-1843.10.1021/ol200352g
23. Prachayasittikul, S.; Doss, G.; Bauer, L., Deoxydative substitution of pyridine 1-oxides by thiols. Part XX. Reactions of (2, 3, and 4-phenyl)-, 3-acetamido-, 3-bromo-, 3-acetoxy-, 3-ethoxypyridine 1-oxides with 1-adamantanethiol in acetic anhydride. *Journal of Heterocyclic Chemistry* **1991,** *28* (4), 1051-1060.https://doi.org/10.1002/jhet.5570280437
24. Kellogg, R. M.; Van Bergen, T. J., Reactions of aryl Grignard reagents with pyridine 1-oxide. Structure of the addition products. *The Journal of Organic Chemistry* **1971,** *36* (12), 1705-1708.10.1021/jo00811a034
25. Mfuh, A. M.; Larionov, O. V., Heterocyclic N-Oxides - An Emerging Class of Therapeutic Agents. *Curr Med Chem* **2015,** *22* (24), 2819-2857.10.2174/0929867322666150619104007
26. Delahoussaye, Y. M.; Evans, J. W.; Brown, J. M., Metabolism of tirapazamine by multiple reductases in the nucleus. *Biochem Pharmacol* **2001,** *62* (9), 1201-9.10.1016/s0006-2952(01)00784-5
27. Jin, H.; Yang, M.; Sun, Z.; Gui, R., Ratiometric two-photon fluorescence probes for sensing, imaging and biomedicine applications at living cell and small animal levels. *Coordination Chemistry Reviews* **2021,** *446*, 214114.https://doi.org/10.1016/j.ccr.2021.214114
28. Lee, M. H.; Kim, J. S.; Sessler, J. L., Small molecule-based ratiometric fluorescence probes for cations, anions, and biomolecules. *Chem Soc Rev* **2015,** *44* (13), 4185-4191.10.1039/c4cs00280f
29. Yoshihara, T.; Yamaguchi, Y.; Hosaka, M.; Takeuchi, T.; Tobita, S., Ratiometric Molecular Sensor for Monitoring Oxygen Levels in Living Cells. *Angewandte Chemie International Edition* **2012,** *51* (17), 4148-4151.https://doi.org/10.1002/anie.201107557
30. Liu, C.; Gong, X.; Lin, R.; Liu, F.; Chen, J.; Wang, Z.; Song, L.; Chu, J., Advances in Imaging Techniques and Genetically Encoded Probes for Photoacoustic Imaging. *Theranostics* **2016,** *6* (13), 2414-2430.10.7150/thno.15878

31. Attia, A. B. E.; Balasundaram, G.; Moothanchery, M.; Dinish, U. S.; Bi, R.; Ntziachristos, V.; Olivo, M., A review of clinical photoacoustic imaging: Current and future trends. *Photoacoustics* **2019,** *16*, 100144.https://doi.org/10.1016/j.pacs.2019.100144

Chapter 2: Synthesis and Characterization of Platinum Alkynyl Complexes

Introduction

The photophysical properties square-planar platinum(II) alkynyl complexes have been studied for decades.[32] The heavy platinum center facilitates spin-orbit coupling that increases the frequency of the intersystem crossing (ISC), resulting in a triplet lowest excited state.[32, 33] Complexes with these energy transitions are often strong emitters, a desirable propertied for devices such as OLEDs.[34, 35] The absorption and emission profiles of these compounds are highly tunable with substituents on the alkynyl ligands or the attachment of chelating ligands (e.g., ^{t}bbpy).[36, 37] Luminescence intensity can be improved with strong donor ligands (e.g. acteylides) and an aromatic π^*acceptor ligands on which the LUMO is located.[36] In addition to synthesizing Pt(II) alkynyl complexes with different ligand motifs to tune the photophysical properties, post-synthetic modifications such as Lewis acid-base interactions with electron-withdrawing groups tunes the emission different based on the location of the interaction.[38]

Despite their luminescent qualities, there are few examples of the Pt(II)(N^N)(alkynyl)$_2$ utilized for biological imaging.[39] Several complexes of this type were synthesized and characterized by previous members of our lab group using a 2-pyridyl acetylene ligand to form a trans-bidentate ligand.[40] Using Pt(II)(^{t}bbpy)Cl$_2$ and 3-pyridyl acetylene, we synthesized a Pt (II) complex to use in our N-oxide approach to oxygen sensing. [Fig. 1]

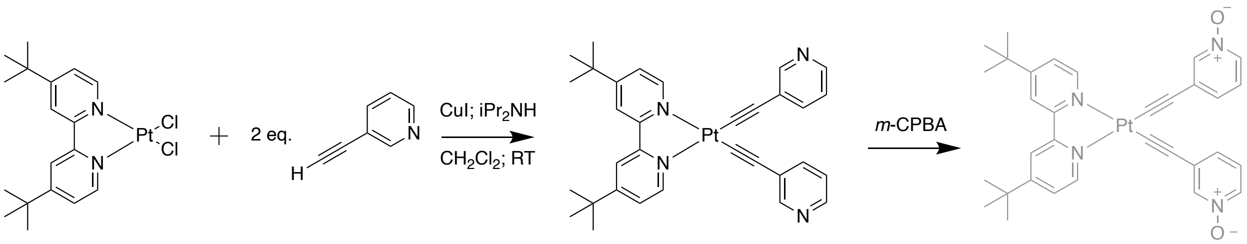

Figure 1: General synthesis of Pt (II) alynyl complexes and N-oxide congener.

Experimental

Materials

All reactions performed under a fume hood. $K_2[PtCl_4]$ and acetylene ligands were used as purchased and stored according to label instructions. Solvents were used as received. Unless otherwise noted, all glassware used for synthetic reaction was dried in an oven. Solvent was evaporated with a Buchi Rotovapor. Pt(^{t}bbpy)Cl_2 and other complexes were synthesized according to reported procedure.[41]

Measurements

NMR spectra were obtained on a JEOL ECX 400 MHz spectrometer and referenced against TMS using residual proton signals (^{1}H NMR) or the ^{13}C resonances of the deuterated solvent (^{13}C NMR). Single crystal X-ray diffraction was used to determine crystal structures, and the structures were refined using the Bruker SHELXTL Software Package.

Preparation of Pt(^{t}bbpy)Cl_2 [41]

K_2PtCl_4 (0.416g, 1.00 mmol) and 4,4'-tert-butyl-2,2'-bipyridine (0.270g, 1.02 mmol) were added to dry flask attached to reflux condenser with H_2O (30 mL) and 4.0 M HCl (2.0 mL). Mixture heated to 155 °C and refluxed for 2 h. Yellow, heterogenous mixture cooled and vacuum filtered, washing with 2x30 mL H_2O, 35 mL MeOH, and 30 mL Et_2O. Yellow solid was dried *in vacuo*. Yield: 0.4940g; 92% ^{1}H NMR (400 MHz, Chloroform-*d*) δ 9.5 (d, J = 6.2 Hz, 1H), 7.9 (d, J = 2.1 Hz, 1H), 7.5 (dd, J = 6.3, 2.2 Hz, 1H), 1.5 (s, 9H).

Preparation of Pt(^{t}bbpy)(C_2-3-py)$_2$ [42]

Pt(^{t}bbpy)Cl_2 (0.0908g, 0.170 mmol), 3-ethynyl pyridine (0.0516g, 0.506 mmol), and CuI (0.0025g; 0.013 mmol) were added to flask. CH_2Cl_2 (15 mL) was added, and the reaction flask was sealed with rubber septa. *i*Pr_2NH (1.5 mL) was added with a syringe. Reaction flask was left to stir in the dark for 24 h. Solvent was evaporated from yellow, heterogenous reaction mixture. Yellow solid redissolved in in CH_2Cl_2 (15 mL) and extracted with 3x50 mL Na_2CO_3 washes followed by 50 mL H_2O wash and 50 mL NaCl wash. The organic layer was dried with $MgSO_4$ and filtered through a Celite plug, and the solvent was evaporated. CuI removed using AlO_2 plug eluted with 5% MeOH/CH_2Cl_2. Eluent was collected, and solvent was evaporated. Yellow solid dried *in vacuo*. Yield: 0.0793g; 70% ^{1}H NMR (400 MHz, Chloroform-*d*) δ 9.7 (d, *J* = 6.0 Hz, 1H), 8.8 (s, 2H), 8.4 (s, 2H), 8.0 (d, *J* = 2.0 Hz, 2H), 7.8 (m, 2H), 7.6 (dd, *J* = 6.0, 2.0 Hz, 2H), 7.2 (m, 2H), 1.5 (s, 17H).

Attempted Preparation of Pt (^{t}bbpy)(C_2-3-pyO)$_2$

Pt(^{t}bbpy)($C_2$3-py)$_2$ (0.0413g, 0.062 mmol) was dissolved in CH_2Cl_2 (20 mL) and chilled to 0°C. *m*-CPBA (0.0209g, 0.121 mmol) was added, and the mixture stirred for 3h. Saturated $NaHCO_3$ (50 mL) added to separation funnel with reaction mixture, and the product was extracted with CH_2Cl_2 (3x30 mL). Organic layer dried over $MgSO_4$, and the solvent was evaporated. TLC in 5% MeOH/CH_2Cl_2 showed distinct band from starting material. Product purified using Prep TLC in 5% MeOH/CH_2Cl_2. The band from 1-3.5 cm (Rf 0.655-0.229) was removed and vacuum filtered, washing with MeOH/CH_2Cl_2. Solvent was evaporated to produce yellow solid. Subsequent analysis showed this product to be starting Pt(^{t}bbpy)($C_2$3-py)$_2$ material.

Results and Discussion

Several Pt(II) complexes were obtained using previously reported procedures as shown in Figure 4.[40-42] The ^{1}H NMR spectrum of a new complex, Pt(^{t}bbpy)(C_2-3py)$_2$ is shown in Figure 8 showing the expected number of peaks with appropriate shift values for the aromatic and *tert*-butyl protons. A crystal structure of Pt(^{t}bbpy)(C_2-3py)$_2$ was obtained showing a structure consistent to complexes previously in the lab group. [Fig.10] The bond angles around the Pt(II) do deviate slightly from the expected values of a square planar complex, but the reason for this is un known. Table 2 shows the standard crystallographic data for this complex. A stirring reaction was performed with *m*-CPBA and Pt(II)(^{t}bbpy)(C_2-3-py)$_2$ to convert the nitrogens on the ethynyl pyridine ligands to N-oxides. The ^{1}H NMR spectrum for the resulting products shows different shift values from the original complex [Fig. 9], which led to the initial conclusion that the reaction was successful. A crystal structure was also obtained of an attempted oxidation of Pt(^{t}bbpy)(C_2-4py)$_2$ using *m*-CPBA [Fig.11]; this showed that the desired N-oxide product was not achieved. Instead, OH and Cl groups attached to the metal center. This suggests the square planar Pt (II) center is more easily oxidized by the *m*-CPBA than the nitrogen atoms in the pyridine. It is likely that the Cl and OH groups are transferred from *m*-CPBA to the Pt center during the reaction.

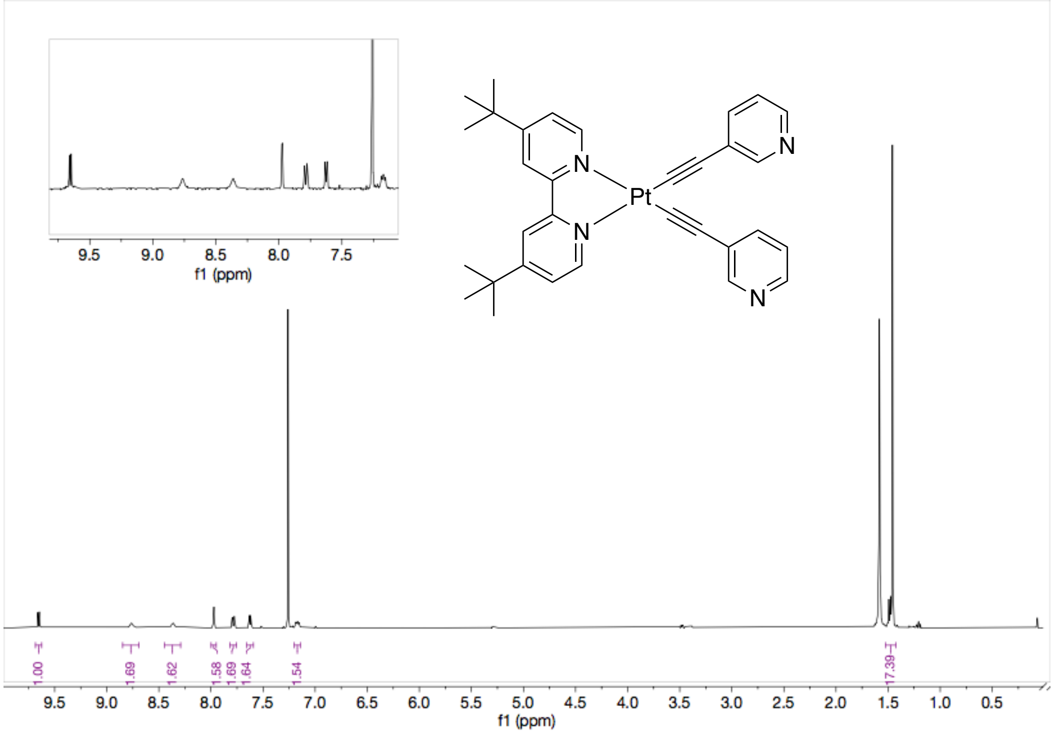

Figure 2: ^{1}H NMR of Pt (^{t}bbpy)(C_2-3-py)$_2$ in $CDCl_3$

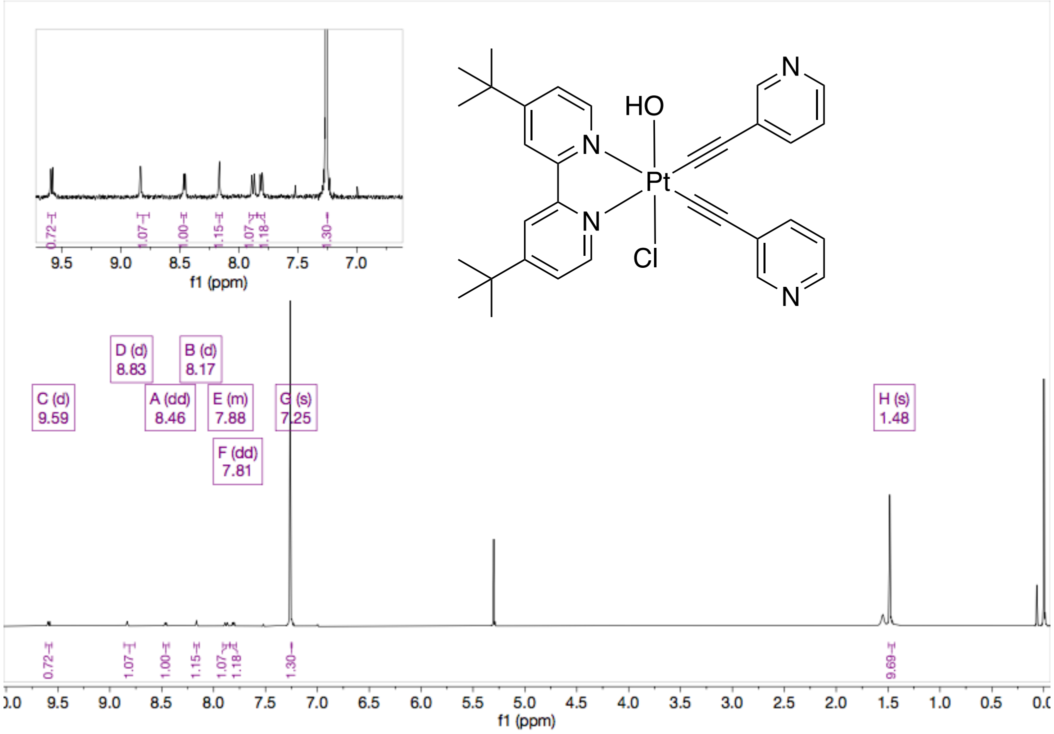

Figure 3: 1H NMR of Pt (^{t}bbpy)(C$_2$-3-pyO)$_2$ in CDCl$_3$

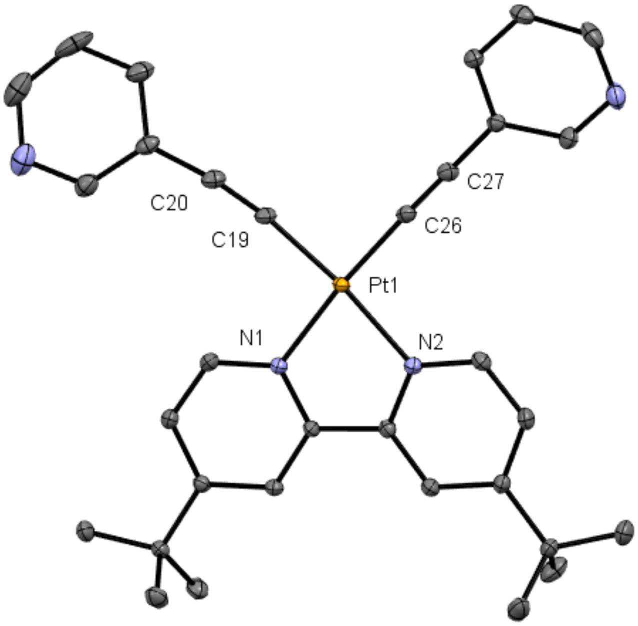

Figure 4: Single-crystal X-ray crystal structure of Pt(II)(^{t}bbpy)(C$_2$-3-py)$_2$. Hydrogen atoms and solvent molecules omitted for clarity.

Table 1. Pt(II) Bond Angles for Pt(II)(^{t}bbpy)(C_2-3-py)$_2$

C19-Pt1-C26	90.74(7)	C19-Pt1-N1	94.17(6)
C26-Pt1-N1	174.78(6)	C19-Pt1-N2	172.63(6)
C26-Pt1-N2	96.50(6)	N1-Pt1-N2	78.63(5)

Table 2: Crystal data and structure refinement for Pt(II)(^{t}bbpy)(C_2-3-py)$_2$

Identification code	d8-4736_a-C32H32N4Pt-polymorph-CIF
Empirical formula	$C_{32}H_{32}N_4Pt$
Formula weight	667.70
Temperature/K	100(2)
Crystal system	triclinic
Space group	P-1
a/Å	10.4840(4)
b/Å	10.8922(5)
c/Å	13.3467(6)
α/°	82.608(2)
β/°	69.4890(10)
γ/°	68.6830(10)
Volume/Å^3	1329.82(10)
Z	2
ρ_{calc}g/cm^3	1.668
μ/mm^{-1}	5.304
F(000)	660.0
Crystal size/mm^3	0.360 × 0.190 × 0.170
Radiation	MoKα (λ = 0.71073)
2Θ range for data collection/°	4.844 to 60.178
Index ranges	$-14 \leq h \leq 14, -15 \leq k \leq 15, -18 \leq l \leq 18$
Reflections collected	66988
Independent reflections	7761 [R_{int} = 0.0365, R_{sigma} = 0.0185]
Data/restraints/parameters	7761/0/340
Goodness-of-fit on F^2	1.070
Final R indexes [I>=2σ (I)]	R_1 = 0.0150, wR_2 = 0.0364
Final R indexes [all data]	R_1 = 0.0155, wR_2 = 0.0367
Largest diff. peak/hole / e Å^{-3}	1.07/-1.30

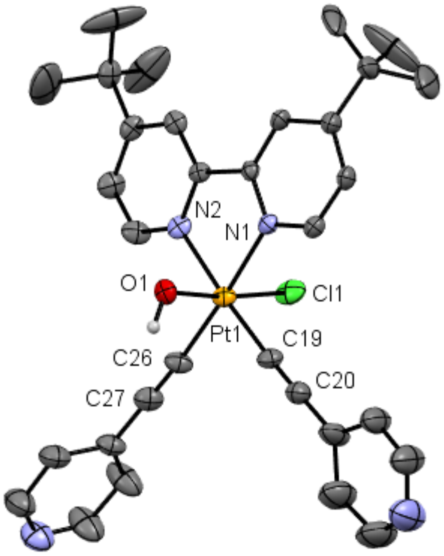

Figure 5: Single-crystal X-ray crystal structure of attempted Pt (^{t}bbpy)(C_2-3-pyO)$_2$. Hydrogen atoms and solvent molecules omitted for clarity.

Table 2: Crystallographic Data for attempted Pt (^{t}bbpy)(C_2-3-pyO)

Identification code	D8_4958_SM_2_105	
Chemical formula	$C_{32}H_{33}ClN_4OPt$	
Formula weight	720.16 g/mol	
Temperature	100(2) K	
Wavelength	0.71073 Å	
Crystal size	0.042 x 0.089 x 0.246 mm	
Crystal system	orthorhombic	
Space group	P b c a	
Unit cell dimensions	a = 11.6110(5) Å	α = 90°
	b = 20.2091(9) Å	β = 90°
	c = 26.7825(11) Å	γ = 90°
Volume	6284.5(5) Å^3	
Z	8	
Density (calculated)	1.522 g/cm^3	
Absorption coefficient	4.580 mm^{-1}	
F(000)	2848	

Conclusions

Although a minor component of this overall project, results from the Pt (II) alkynyl complexes were essential for directing this project towards the synthesis of saturated metal complexes. It is important to note that while the crystal structure for the failed N-oxide experiment shows pyridine ligands in the 4 positions while Figure 4 shows the same complex with 3-ethynyl pyridine ligands; however, it is expected that *m*-CPBA reaction with Pt(II*)*(^{t}bbpy)(C_2-3-py)$_2$ would produce a similar result. Although the data was not available for this project, anecdotal experiments with ethynyl pyridine ligands already containing the N-oxide group show a cleavage of the N-oxide during the reaction, resulting in complexes similar to Figure 4. These complexes have many potential applications including the addition of electron-withdrawing or donating groups on the ligands to tune emission, but no future work will be done with these complexes for oxygen sensing in cells using an N-oxide mechanism.

References

32. Muro, M. L.; Rachford, A. A.; Wang, X.; Castellano, F. N., PlatinumII Acetylide Photophysics. In *Photophysics of Organometallics*, Lees, A. J., Ed. Springer Berlin Heidelberg: Berlin, Heidelberg, 2010; pp 1-35.
33. Li, W.; Wang, J.; Yan, X.; Zhang, H.; Shen, W., Electronic structures and photophysical properties of phosphorescent platinum (II) complexes with tridentate C^NN cyclometalated ligands. *Applied organometallic chemistry* **2018,** *32* (1), e3929-n/a.10.1002/aoc.3929
34. Kong, F. K.-W.; Tang, M.-C.; Wong, Y.-C.; Ng, M.; Chan, M.-Y.; Yam, V. W.-W., Strategy for the Realization of Efficient Solution-Processable Phosphorescent Organic Light-Emitting Devices: Design and Synthesis of Bipolar Alkynylplatinum(II) Complexes. *Journal of the American Chemical Society* **2017,** *139* (18), 6351-6362.10.1021/jacs.7b00479
35. Rausch, A. F.; Homeier, H. H. H.; Yersin, H., Organometallic Pt(II) and Ir(III) Triplet Emitters for OLED Applications and the Role of Spin–Orbit Coupling: A Study Based on High-Resolution Optical Spectroscopy. In *Photophysics of Organometallics*, Lees, A. J., Ed. Springer Berlin Heidelberg: Berlin, Heidelberg, 2010; pp 193-235.
36. Stengel, I.; Strassert, C. A.; Plummer, E. A.; Chien, C. H.; De Cola, L.; Bäuerle, P., Postfunctionalization of Luminescent Bipyridine PtII Bisacetylides by Click Chemistry. *European journal of inorganic chemistry* **2012,** *2012* (11), 1795-1809.10.1002/ejic.201200061
37. Wei, L.; Bao-Xiu, M.; Chan, M. C. W.; Zheng, H.; Chi-Ming, C.; Zhu, N.; Lee, S.-T., Light emitting tridentate cyclometalated platinum complexes containing sigma-alkynyl auxiliaries: tuning of photo- and electrophosphorescene. *Journal of the American Chemical Society* **2004,** *126* (15), 4958
38. Na, H.; Maity, A.; Teets, T. S., Postsynthetic Systematic Electronic Tuning of Organoplatinum Photosensitizers via Secondary Coordination Sphere Interactions. *Organometallics* **2016,** *35* (13), 2267-2274.10.1021/acs.organomet.6b00332
39. Thorp-Greenwood, F. L., An Introduction to Organometallic Complexes in Fluorescence Cell Imaging: Current Applications and Future Prospects. *Organometallics* **2012,** *31* (16), 5686-5692.10.1021/om3004477
40. Jaques, L. D.; McDarmont, S. L.; Smart, M. M.; McMillen, C. D.; Neglia, S. E.; Lee, J. P.; Pienkos, J. A., Structural characterization of the metalloligand tbpyPt(C22-py)2 and its interaction with Pd(OAc)2. *Inorganic chemistry communications* **2020,** *112*, 107722.10.1016/j.inoche.2019.107722
41. Zhong, F.; Zhao, J., An N^N Platinum(II) Bis(acetylide) Complex with Naphthalimide and Pyrene Ligands: Synthesis, Photophysical Properties, and Application in Triplet–Triplet Annihilation Upconversion. *European Journal of Inorganic Chemistry* **2017,** *2017* (44), 5196-5204.https://doi.org/10.1002/ejic.201700656
42. Wong, W. L. C. W. C. Z.-M. C. H. K.-Y., Structural Basis for Vapoluminescent Organoplatinum Materials Derived from Noncovalent Interactions as Recognition Components. *Chemistry – A European Journal* **2003,** *9*, 11

Chapter 3: Synthesis and Characterization of Iridium (III) Complexes

Introduction

Cyclometalated iridium(III) complexes have been utilized for a wide variety of applications. These complexes are powerful light-emitters, with high quantum efficiencies and photostability in addition to highly tunable optical and photophysical properties.[43] For these reasons, these complexes have been explored extensively for use in organic light-emitting devices (OLEDs)[33, 35, 44] and light-emitting electrochemical cells (LEECs)[45], which are important for the improved efficiency and quality of many technological applications such as full-color displays. Much of the literature on cyclometalated complexes studies the effect of structural modifications on the photophysical and optoelectronic properties to improve quantum efficiency or color purity.[46] Current challenges with these light emitting devices are long-lasting blue emission and white light generation, problems which cyclometalated iridium complexes have been utilized to address. [44-48]. Other applications include the detection of volatile organic compounds (VOCs)[49], photosensitizers[50], and solid-state polymer-based molecular oxygen sensors[51].

Iridium (III), a d^6 third-row transition metal, exhibits large ligand field splitting (Δ_0); heavy metals are also associated with increased spin-orbit coupling between triplet and singlet excited states, which facilitates rapid intersystem crossing (ISC).[19, 35] The C^N cyclometalating ligands used for the complexes in this project further increase Δ_0 due to the σ-donor action of the Ir-C bonds and the heterocyclic ring acting as a π^*acceptor.[52] The resulting lowest energy state is a mixture of ^{3}MLCT and ^{3}LC transitions. Because a large proportion of the optoelectronic properties is due to ligand structure, it follows that the properties of the complex can be easily tuned by altering the ligand, such as the variations to bipyridine shown in Figure 1. This is confirmed by extensive literature precedent, which details complexes with emission ranging from near-UV and blue to red and near-IR.[44, 53-55]

Tuning the photophysical properties of these complexes requires shifting the energy of the HOMO, LUMO, or both. Generally, the HOMO is thought to be influenced by the aryl rings/Ir-C bonds and the LUMO influenced by the heterocyclic rings.[52] It has also been shown that for complexes of the form Ir(C^N)$_2$(N^N), the HOMO is centered on the C^N ligands and metal center while the LUMO is typically centered on the N^N or N^O ligand.[56] Synthesizing the complex with C^N ligands containing electron-withdrawing groups (e.g., -F, -CF$_3$, -CN) is typically used to blueshift emission;[45] this approach has been combined with the use of N^O ligands (e.g. picolinate) to further stabilize the HOMO.[52] Red-shifted emission is typically achieved by extending the aromatic system of the N^N ligand (e.g., replacing 2,2' bipyridine with 2,2' biquinoline) or attaching electron donating groups such as MeO [Fig. 1a] to the C^N ligand.[45, 53, 54, 57]

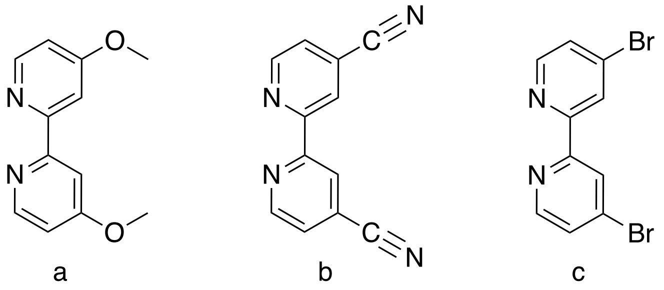

Figure 1: Example N^N ligands with electron density-altering functional groups. a) 4,4'-Methoxybipyridine. b) 4,4'-Cyanobipyridine. c) 4,4'-Bromobipyridine

Many of the properties that make these complexes ideal for light-emitting devices are ideal characteristics of biological imaging agents. Long fluorescence lifetimes, resistance to photobleaching, and emission in the visible region allow for sensitive measurement *in vivo*.[39] [Ir(dfppy)$_2$(biqinoline)]$^+$ and similar compounds were found to be effective phosphorescent dyes in cells with emissions ranging from blue to red.[55] It's also possible to conjugate biomolecules (e.g., biotin, galactose, peptide) to one of the cyclometalated ligands to form labeling reagents[58]. Although most of the complexes are distributed throughout the cytoplasm alone[55, 59], structural changes such as charge and functional groups may be used to localize the complexes to a desired area (e.g., mitochondria).[58] For hypoxia sensing, it is ideal for the probe to be uniformly distributed throughout the cell and tumor. Cationic complexes have been utilized more frequently do to their increased cellular uptake, but the uptake of neutral complexes like those with N^O ligands can be improved with function groups that increase the amphiphilicity of the complexes.[59] There is ample evidence that iridium (III) complexes can function as effective intracellular sensors for gaseous molecules, ions, or amino acids.[59]

This chapter will detail the synthesis and characterization of cationic and neutral iridium (III) complexes that contain two cyclometalated C^N ligand and an ancillary ligand (N^N or N^O) with uncoordinated nitrogen (s). The goal is to show that these external nitrogens can be converted to N-oxides accompanied by a tuning of photophysical properties. There is precedent for utilizing iridium complexes as hypoxia sensors, including one [Ir(btph)$_2$(acac)] complex relying solely on the quenching of phosphorescence[60] [Fig. 2] and a larger sensor containing a phosphorescent iridium subunit and a fluorescent organic subunit joined by a rigid linker.[29]

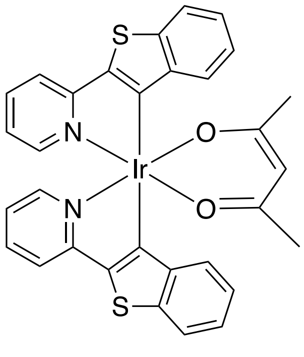

Figure 2: Ir(III)(btph)$_2$(acac) probe for hypoxia sensing.[60]

While these studies were promising, there is still a gap to be filled in terms of optimizing the optical properties and cellular affinity/localization. Several novel cyclometalated iridium (III) complexes were synthesized and characterized using NMR and X-ray crystallography. Figure 3 shows a series of cationic iridium complexes of the form $[Ir(C\hat{}N)_2(N\hat{}N)]^+$; Figure 4 shows a series of neutral complexes of the form $Ir(C\hat{}N)_2(N\hat{}O)$. Except for $[Ir(dfppy)_2(biquinoline)]\ PF_6$ [Fig.3 complex 1] and $Ir(dfppy)_2(picolinate)$ [Fig.4 complex 5], no previous synthesis has been reported for the complexes detailed in this chapter. Due to the lack of similar ^{13}C and 2D NMR data available for these complexes, full spectroscopic characterization and elemental analysis is ongoing for many of these complexes. Two N-oxide congeners of their respective complexes were also synthesized [Fig. 4, complexes 6a-7b]; these complexes were more fully characterized and will be discussed in greater detail.

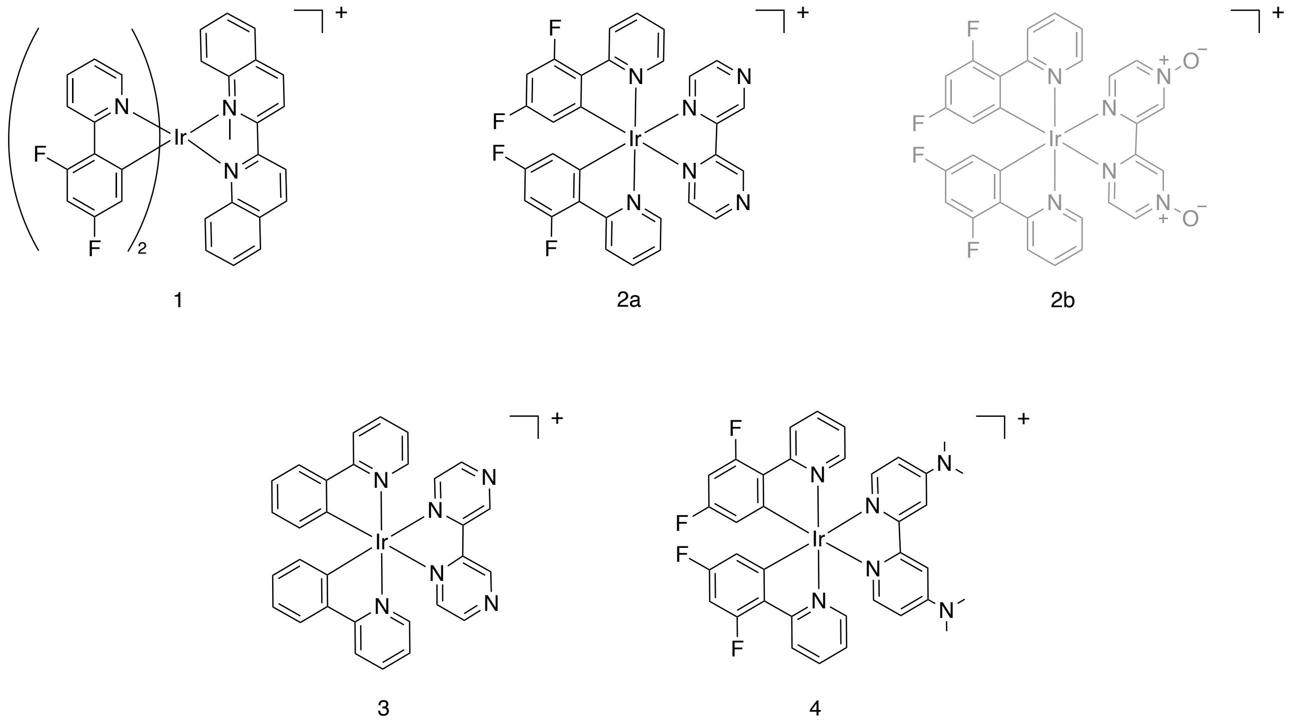
1

2a

2b

3

4

Figure 3: Cationic cyclometalated Ir (III) complexes.

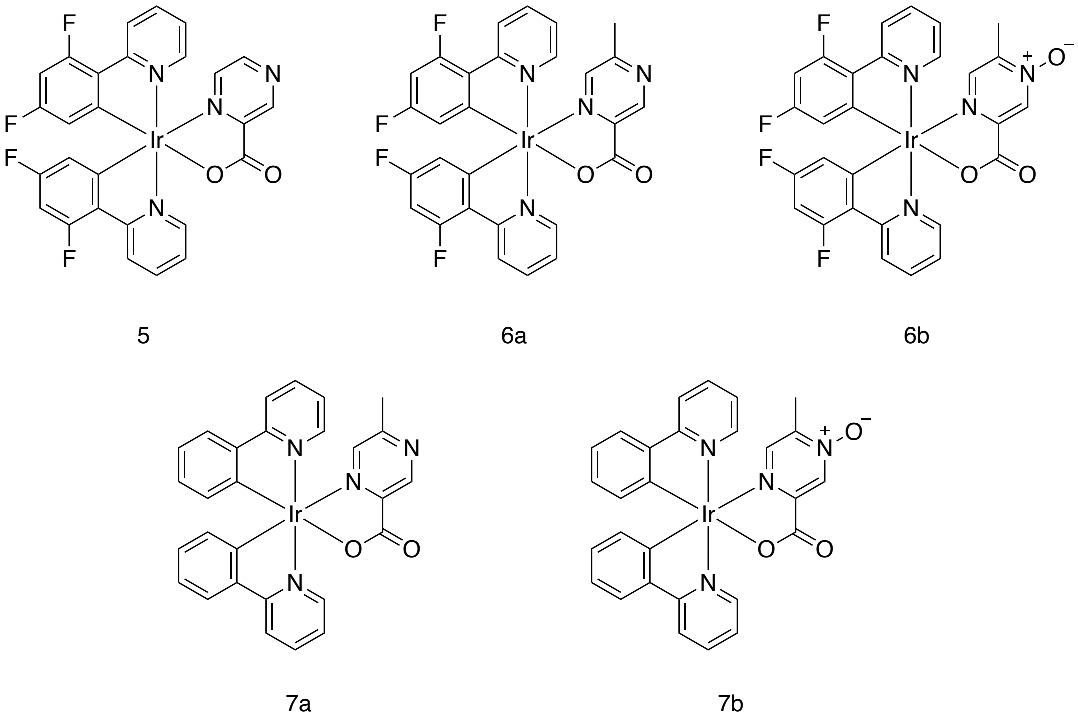
5

6a

6b

7a

7b

Figure 4: Neutral cyclometalated Ir(III) Complexes

Experimental

Materials

All reactions were performed inside a fume hood. Solvents used as received. $IrCl_3{\bullet}H_2O$ and chelating ligands were purchased from Sigma Aldrich and Fischer Scientific. Reagents were stored at room temperature or in the refrigerator according to label instructions. Unless otherwise noted, glassware was oven-dried before use. Solvent was evaporated with a Buchi Rotovapor Iridium dimer starting material was synthesized according to literature procedure.[61]

Measurements and Instrumentation

NMR spectra were obtained on a JEOL ECX 400 MHz spectrometer and referenced against TMS using residual proton signals (^1H NMR) or the ^{13}C resonances of the deuterated solvent (^{13}C NMR). Single crystal X-ray diffraction was used to determine crystal structures, and the structures were refined using the Bruker SHELXTL Software Package. UV-Vis absorbance measurements were conducted in CH_2Cl_2 using a Cary 60 UV-Vis spectrophotometer at room temperature. Emission data was collected using a Cary Eclipse Fluorospectrophotometer in CH_2Cl_2.

Preparation of [(dfppy)$_2$Ir(μ-Cl)]$_2$[61]

$IrCl_3 \cdot H_2O$ (1.010g, 3.38 mmol) and 2-2,4-difluorophenylpyridine (1.4805g, 7.74 mmol) were added to a dry flask with EtOEtOH (30mL) and H_2O (10 mL). The black, heterogenous mixture refluxed under N_2 for 20 h. After which time, a yellow, heterogenous mixture resulted and was allowed to cool to RT. The yellow solid was collected by vacuum filtration, washed with 3x10mL H_2O and 3x10mL Et_2O and dried *in vacuo*. Yield: 1.3934g (68%). ^1H NMR (400 MHz, Chloroform-*d*) δ 9.12 (ddd, J = 5.8, 1.7, 0.7 Hz, 4H), 8.31 (d, J = 8.6 Hz, 4H), 7.83 (m, 4H), 6.83 (ddd, J = 7.3, 5.8, 1.4 Hz, 4H), 6.34 (m, 4H), 5.28 (m, 4H). Preparation of [(ppy)$_2$Ir(μ-Cl)]$_2$ followed an identical procedure.

General Preparation for Cationic Ir(C^N)$_2$(N^N)' complexes[62]***(GP1)***

[(C^N)$_2$Ir(μ-Cl)]$_2$ and 2.2 molar equivalents of N^N were added to dry flask with ethylene glycol. Yellow, heterogenous mixture was refluxed at 150 °C under N_2 for 16-20h. A saturated NH_4PF_6 solution was added to cooled mixture (10-15 mL) to precipitate product. The mixture was vacuum filtered and washed with H_2O (3x15mL) and Et_2O (3x15mL). Solid was dried *in vacuo.*

[Ir(dfppy)$_2$(biquinoline)] PF_6 (1)

Prepared according to **GP1** using [(dfppy)$_2$Ir(μ-Cl)]$_2$ (0.2435g, 0.200 mmol); biq (0.1136g, 0.440 mmol); Yield: 0.3601g (91%) Compound was found to contain significant impurities after several failed crystal experiments. A TLC plate in 5% MeOH/CH_2Cl_2 showed a distinct orange band; an SiO_2 column eluted with 5% MeOH/CH_2Cl_2 used to purify compound.

Seven orange fractions were collected and combined; solvent was evaporated, and product was dried in vacuo. Yield: 0.1573g. Orange crystals were grown by vapor diffusion of hexanes in CH_2Cl_2. ^1H NMR (400 MHz, DMSO-d_6) δ 9.01 (d, *J* = 8.9 Hz, 2H), 8.98 (d, *J* = 8.8 Hz, 2H), 8.20 (m, 2H), 8.16 (m, 2H), 8.03 (m, 2H), 7.98 (td, *J* = 7.8, 1.5 Hz, 2H), 7.69 (m, 2H), 7.66 (m, 2H), 7.39 (ddd, *J* = 8.7, 6.9, 1.5 Hz, 2H), 7.17 (ddd, *J* = 7.3, 5.8, 1.4 Hz, 2H), 6.98 (ddd, *J* = 12.1, 9.4, 2.4 Hz, 2H), 5.69 (dd, *J* = 8.6, 2.4 Hz, 2H).

[Ir(dfppy)$_2$(bipyrazine)] PF_6 (2a)

P Prepared according to **GP1** using [(dfppy)$_2$Ir(μ-Cl)]$_2$ (0.2432g, 0.200 mmol); bpz (0.0696, 0.440 mmol); Yield: 0.3267g (93%) ^1H NMR (400 MHz, DMSO-d_6) δ 10.26 (s, 2H), 8.91 (d, *J* = 3.1 Hz, 2H), 8.29 (d, *J* = 8.5 Hz, 2H), 8.06 (t, *J* = 8.0 Hz, 2H), 7.98 (d, *J* = 3.1 Hz, 2H), 7.82 (d, *J* = 5.8 Hz, 2H), 7.22 (t, *J* = 6.8 Hz, 2H), 7.02 (ddd, *J* = 12.2, 9.4, 2.4 Hz, 2H), 5.56 (dd, *J* = 8.4, 2.4 Hz, 2H).

[Ir(ppy)$_2$(bipyrazine)] PF_6 (3)

Prepared according to **GP1** [(ppy)$_2$Ir(μ-Cl)]$_2$ (0.100g, 0.093 mmol); bpz (0.0334g, 0.211 mmol); ^1H NMR (400 MHz, DMSO-d_6) δ 8.91 (d, *J* = 3.0 Hz, 4H), 8.27 (m, 4H), 7.98 (d, *J* = 8.0 Hz, 4H), 7.94 (d, *J* = 7.3 Hz, 4H), 7.86 (dd, *J* = 3.1, 1.2 Hz, 4H), 7.75 (m, 4H), 7.14 (m, 4H), 7.05 (t, *J* = 7.5 Hz, 4H), 6.94 (m, 4H), 6.13 (m, 4H).

[Ir(dfppy)$_2$((NMe)$_2$bipyrazine)] PF_6 (4)

Prepared according to **GP1** using [(dfppy)$_2$Ir(μ-Cl)]$_2$ (0.1012g, 0.083 mmol); (NMe)$_2$bpy (0.0442, 0.182 mmol); Yield: 0.3267g (93%) ^1H NMR (400 MHz, Acetonitrile-d_3) δ 8.3 (d, *J* = 8.5 Hz, 2H), 7.9 (m, 2H), 7.8 (dd, *J* = 5.9, 1.6 Hz, 2H), 7.5 (d, *J* = 2.8 Hz, 2H), 7.4 (d, *J* = 6.7 Hz, 2H), 7.1 (ddd, *J* = 7.4, 5.8, 1.5 Hz, 2H), 6.6 (ddd, *J* = 12.2, 9.4, 2.4 Hz, 2H), 6.6 (dd, *J* = 6.8, 2.8 Hz, 2H), 5.7 (dd, *J* = 8.7, 2.4 Hz, 2H), 3.1 (s, 12H).

General Procedure for Neutral N^O Iridium Complexes[63] ***(GP2)***

$Ir_2(C^\wedge N)_2(\mu\text{-}Cl)_2$, 3 molar equivalents N^O ligand, and 6 molar equivalents K_2CO_3 were added to an oven-dried pressure tube with CH_2Cl_2. N_2 was bubbled into the solution to remove oxygen. The pressure tube was quickly sealed, and the reaction mixture was heated to 60°C in an oil bath and refluxed overnight. Solvent was evaporated from the cooled mixture. The solid product was purified using an SiO_2 column, eluted with 5% MeOH/CH_2Cl_2. Fractions matching the luminescent bands on the TLC of the crude mixture were combined, and excess solvent was evaporated to form a solid. Hexanes were added to the solid, and the mixture was sonicated for further purification. Hexanes were evaporated, and the product was dried *in vacuo*.

Ir(dfppy)$_2$(5Me-pz-COO) (6a)

Prepared according to **GP2** using [(dfppy)$_2$Ir(μ-Cl)]$_2$ (0.2021g, 0.166 mmol); 5-Methyl-2-carboxyl pyrazine (0.0688g, 0.498 mmol); K_2CO_3 (0.1373g, 0.993 mmol) ^{1}H NMR (400 MHz, Chloroform-*d*) δ 9.37 (d, *J* = 1.3 Hz, 1H), 8.70 (ddd, *J* = 5.7, 1.6, 0.8 Hz, 1H), 8.31 (dt, *J* = 8.1, 1.9 Hz, 1H), 8.27 (m, 1H), 7.83 (m, 1H), 7.81 (m, 1H), 7.55 (dd, *J* = 1.3, 0.6 Hz, 1H), 7.41 (ddd, *J* = 5.8, 1.6, 0.8 Hz, 1H), 7.23 (ddd, *J* = 7.3, 5.8, 1.4 Hz, 1H), 7.02 (ddd, *J* = 7.3, 5.8, 1.4 Hz, 1H), 6.51 (ddd, *J* = 12.4, 9.2, 2.4 Hz, 1H), 6.42 (ddd, *J* = 12.5, 9.2, 2.4 Hz, 1H), 5.81 (dd, *J* = 8.5, 2.4 Hz, 1H), 5.49 (dd, *J* = 8.7, 2.4 Hz, 1H), 2.58 (s, 3H).

Ir(dfppy)$_2$(5Me-pzO-COO) (6b)

Prepared according to **GP2** using [(dfppy)$_2$Ir(μ-Cl)]$_2$ (0.4203g, 0.346 mmol); 5-Methyl-2-carboxyl pyrazine oxide (0.1620g, 1.05 mmol); K_2CO_3 (0.2870g, 2.08 mmol); Yield ^{1}H NMR (400 MHz, Chloroform-*d*) δ 8.80 (s, 1H), 8.64 (ddd, *J* = 5.8, 1.7, 0.8 Hz, 1H), 8.27 (m, 1H), 8.24 (m, 1H), 7.81 (m, 1H), 7.77 (m, 1H), 7.62 (ddd, *J* = 5.8, 1.7, 0.8 Hz, 1H), 7.49 (m, 1H), 7.22

(ddd, *J* = 7.3, 5.8, 1.4 Hz, 1H), 7.04 (ddd, *J* = 7.4, 5.8, 1.4 Hz, 1H), 6.46 (ddd, *J* = 12.3, 9.1, 2.4 Hz, 1H), 6.38 (ddd, *J* = 12.5, 9.1, 2.4 Hz, 1H), 5.76 (dd, *J* = 8.5, 2.4 Hz, 1H), 5.47 (dd, *J* = 8.7, 2.4 Hz, 1H), 2.32 (s, 3H).This seems like an important compound. Is it known and that is why you limited the procedure? My guess is this is new compound and needs significantly more detail

Ir(ppy)$_2$(5Me-pz-COO) (7a)

Prepared according to **GP2** using [(ppy)$_2$Ir(μ-Cl)]$_2$ (0.5001g, 0.466 mmol); 5-Methyl-2-carboxyl pyrazine (0.1936g, 1.40 mmol); K_2CO_3 (0.3870g, 2.80 mmol); yield: 87%. ^{1}H NMR (400 MHz, Chloroform-*d*) δ 9.35 (d, *J* = 1.3 Hz, 1H), 8.73 (ddd, *J* = 5.8, 1.6, 0.8 Hz, 1H), 7.90 (dt, *J* = 8.2, 1.2 Hz, 1H), 7.86 (dt, *J* = 8.2, 1.2 Hz, 1H), 7.76 (m, 1H), 7.73 (m, 1H), 7.62 (dd, *J* = 7.7, 1.4 Hz, 1H), 7.59 (dd, *J* = 7.8, 1.4 Hz, 1H), 7.54 (dd, *J* = 1.3, 0.6 Hz, 1H), 7.46 (ddd, *J* = 5.8, 1.6, 0.7 Hz, 1H), 7.17 (ddd, *J* = 7.3, 5.8, 1.4 Hz, 1H), 6.98 (m, 1H), 6.94 (dd, *J* = 7.5, 1.3 Hz, 1H), 6.87 (td, *J* = 7.5, 1.2 Hz, 1H), 6.82 (td, *J* = 7.4, 1.4 Hz, 1H), 6.76 (td, *J* = 7.4, 1.4 Hz, 1H), 6.39 (dd, *J* = 7.6, 1.2 Hz, 1H), 6.12 (dd, *J* = 7.6, 1.2 Hz, 1H), 2.50 (s, 3H).

Ir(ppy)$_2$(5Me-pzO-COO) (7b)

Prepared according to **GP2** using [(dfppy)$_2$Ir(μ-Cl)]$_2$ (0.5000g, 0.466 mmol); 5-Methyl-2-carboxyl pyrazine oxide (0.2163g, 1.40 mmol); K_2CO_3 (0.0.3887g, 2.81 mmol); Yield: 70.3% ^{1}H NMR (400 MHz, Chloroform-*d*) δ 8.85 (s, 1H), 8.73 (ddd, *J* = 5.8, 1.6, 0.8 Hz, 1H), 7.91 (m, 1H), 7.87 (m, 1H), 7.78 (m, 1H), 7.76 (m, 1H), 7.65 (ddd, *J* = 5.8, 1.6, 0.8 Hz, 1H), 7.62 (dd, *J* = 7.7, 1.4 Hz, 1H), 7.59 (dd, *J* = 7.8, 1.4 Hz, 1H), 7.49 (t, *J* = 0.7 Hz, 1H), 7.20 (ddd, *J* = 7.3, 5.8, 1.4 Hz, 1H), 7.03 (ddd, *J* = 7.3, 5.8, 1.4 Hz, 1H), 6.95 (td, *J* = 7.5, 1.2 Hz, 1H), 6.88 (td, *J* = 7.5, 1.2 Hz, 1H), 6.82 (td, *J* = 7.4, 1.4 Hz, 1H), 6.76 (td, *J* = 7.4, 1.4 Hz, 1H), 6.38 (dd, *J* = 7.7, 1.2 Hz, 1H), 6.12 (dd, *J* = 7.7, 1.2 Hz, 1H), 2.31 (s, 3H).

Direct Oxidation of Nitrogen using m-CPBA

Ir(dfppy)$_2$(bpz) prepared according to **GP1** was dissolved in CH_2Cl_2. 3 molar equivalents *m*-CPBA were added to solution. Mixture was stirred for 3 h. TLC was performed in 5% MeOH/CH_2Cl_2 to determine if new product was formed. Solvent was evaporated from mixture to produce solid. Crude ^{1}H NMR data of the complexes is shown below.

Ir(dfppy)$_2$(bpzO)

^{1}H NMR (400 MHz, DMSO-d$_6$) δ 8.91 (d, J = 3.0 Hz, 2H), 8.29 (d, J = 8.4 Hz, 2H), 8.06 (td, J = 7.9, 1.6 Hz, 2H), 7.98 (dd, J = 3.0, 1.3 Hz, 2H), 7.82 (dd, J = 6.0, 1.5 Hz, 2H), 7.22 (ddd, J = 7.2, 5.7, 1.3 Hz, 2H), 7.03 (m, 2H), 5.56 (dd, J = 8.4, 2.4 Hz, 2H), 4.45 (s, 2H).

Ir(dfppy)$_2$(bpzO)

^{1}H NMR (400 MHz, DMSO-d$_6$) δ 8.91 (d, J = 3.0 Hz, 2H), 8.29 (d, J = 8.4 Hz, 2H), 8.07 (q, J = 8.8, 8.0 Hz, 2H), 7.99 (dd, J = 3.0, 1.3 Hz, 2H), 7.82 (m, 2H), 7.22 (m, 2H), 7.01 (m, 2H), 5.56 (dd, J = 8.4, 2.4 Hz, 2H).

Ir(dfppy)$_2$(bpzO) ES-57 (2b)

^{1}H NMR (400 MHz, DMSO-d$_6$) δ 10.25 (d, J = 1.3 Hz, 2H), 8.91 (d, J = 3.0 Hz, 2H), 8.29 (d, J = 8.5 Hz, 2H), 8.06 (td, J = 7.8, 1.5 Hz, 2H), 7.98 (dd, J = 3.0, 1.3 Hz, 2H), 7.82 (m, 2H), 7.22 (ddd, J = 7.4, 5.8, 1.4 Hz, 2H), 7.03 (ddd, J = 12.2, 9.4, 2.4 Hz, 2H), 5.56 (dd, J = 8.5, 2.4 Hz, 2H).

Crystallography Data Collection

All attempted crystal experiments employed layering or vapor-vapor diffusion where the complex was dissolved in CH_2Cl_2 and crystallized with hexanes or Et_2O. All crystal structures shown in this report were obtained through collaboration with Dr. Colin McMillen at Clemson University. Single crystal X-ray diffraction was used to determine crystal structures, and the structures were refined using the Bruker SHELXTL Software Package.

Photophysical Data Collection

To make solutions sufficient for absorption and emission experiments, 0.0054g of complexes 7a and 7b were dissolved in CH_2Cl_2, and the solution was diluted to 100 mL in a volumetric flask. A 1:5 dilution was performed to bring the final concentrations to approximately 0.083 mM. Standard quartz cuvettes were used to take absorption and emission measurements using the instruments detailed previously.

Results and Discussion

Synthesis

The facile synthesis of cyclometalated iridium complexes was one of the influential factors when considering what type of compounds to use for this project. Representative synthetic schemes for the cationic [Figure 5] and neutral [Figure 6] are shown below. While no alteration to literature procedure was required for the cationic complexes[62], the neutral N^O complexes presented a challenge. Earlier syntheses refluxed the Ir dimer and N^O ligand with ethoxy ethanol and Na_2CO_3.[64] Despite various combinations of extraction and column chromatography conditions, excess solvent continued to appear in the NMR spectra in greater concentrations than the product and other expected impurities such as H_2O. An alternative procedure using acetone was found in the literature[63], and this was adapted into the one shown in Figure and detailed in the experimental section.

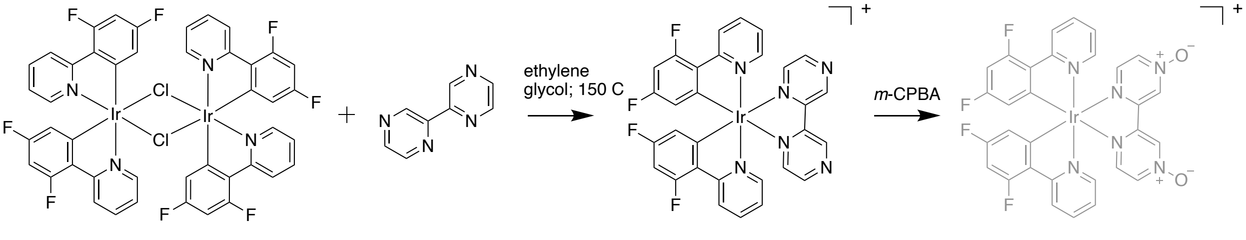

Figure 5: Synthesis of Cationic Ir(C^N)2(N^N) Complexes

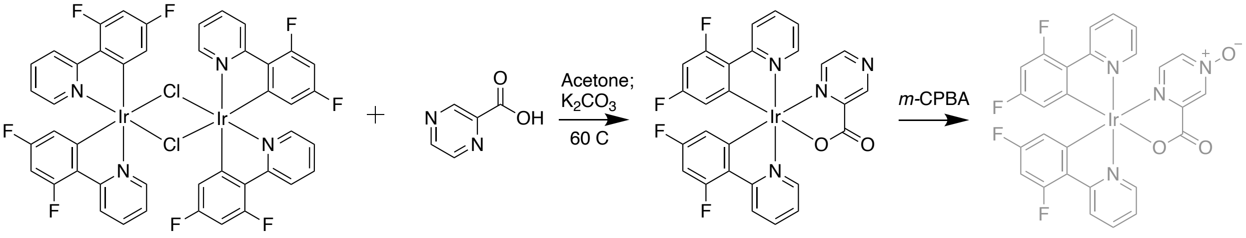

Figure 6: Synthesis of Neutral Ir(C^N)2(N^O)

The first strategy utilized to make the N-oxide congeners of the complexes was the direct oxidation of the external nitrogen using *m*-CPBA.[Fig.7] Conversion of pyridine into pyridine oxide using CH_2Cl_2 and *m*-CPBA was found in the literature, and this method was applied to several compounds as detailed in the experimental section. While the NMR spectra of the *m*-CPBA experiments did not qualitatively look identical to the original compound, the peak shifts in the aromatic region had identical values, meaning that this method is not suitable for making N-oxides.

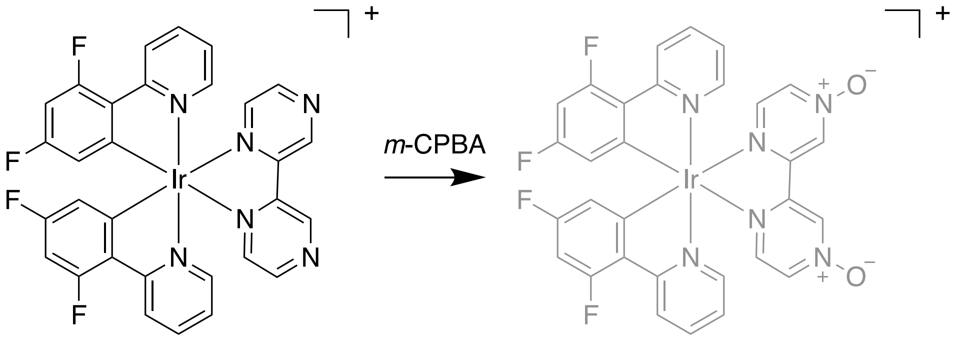

Figure 7: Attempted Preparation of Complex 2b using *m*-CPBA.

An alternative and ultimately successful strategy was the synthesis of iridium complexes using ligands that already contained and N-oxide group. The nature of the ligands used for these complexes dictated that the N-oxide must be located in a different position than the chelating atoms, ensuring the formation of only one complex. 4-oxo-5-methylpyrazine-2-carboxylic acid, also known as Acipimox, is a drug molecule limitedly used to lower fat content in the blood. For the purposes of this project, the position of the carboxylic acid group rendered it similar in chelating structure to the pyrazine carboxylic acid we had already use to synthesize Ir(dfppy)$_2$(picolinate). The ligand without the oxygen group was also commercially available. Using these two ligands, we were able to synthesize two neutral iridium complexes and their N-oxide congeners according to **GP2**, which allowed us to characterize the effects of the N-oxide on some of the physical properties.

Characterization

Several cationic [Ir(C^N)$_2$(N^N)]$^+$ were successfully synthesized and characterized by NMR, X-ray crystallography, and Cyclic Voltammetry. These complexes were straightforward to characterize by NMR due to the symmetry of the molecule. The ^{1}H and ^{13}C NMR spectra show the correct number of peaks in the aromatic range to confirm the synthesis of complex 2 [Fig. 8-9]. Although it was not needed to confirm the identity of the compound, multiple 2D spectra (COSY and HSQC) were collected to further investigate these compounds. [Fig. 9-10] If the N-oxide congener of this complex was synthesized, the 2D spectra would be helpful for determining which peak we would expect to see shifted due to the oxygen. The crystal structure of complex 2 is shown in figure 12. The nitrogen of the phenyl pyridine ligands are located approximate 180° from each other, which is consistent with structure found in the literature containing these C^N ligands.[52,55] Although the isomeric forms of these complexes were not of initial concern, the crystal structure complex 4 shows that the heterocyclic nitrogens coordinated to the metal remain in the same configuration between compounds.[Fig. 13] Table 1 compares the crystal parameters of the two structures shown in Figures 11 and 12.

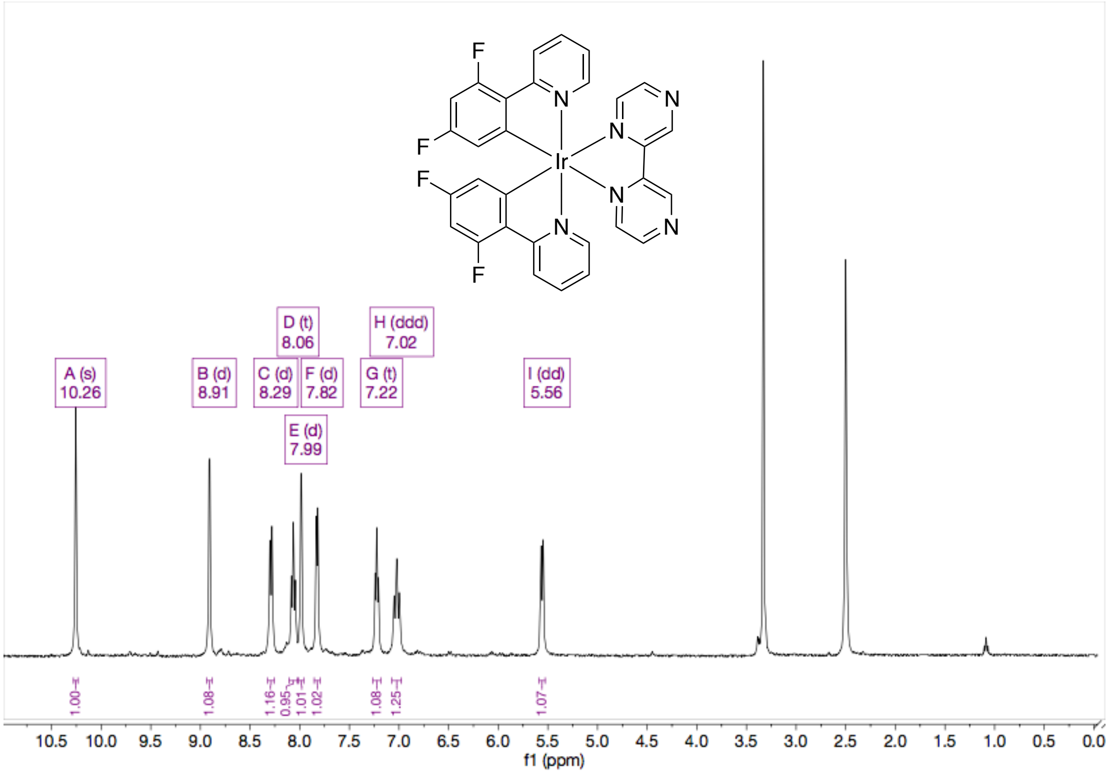

Figure 8: ^{1}H NMR of complex 2a in d6-DMSO

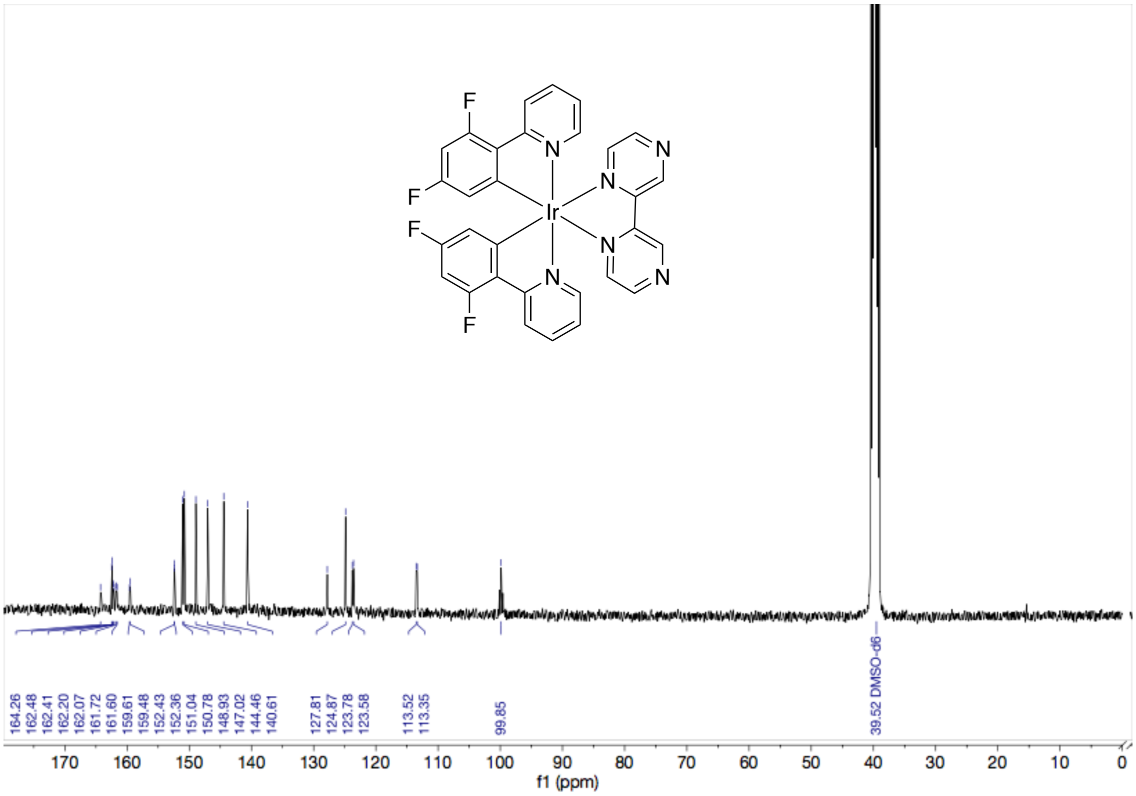

Figure 9: ^{13}C NMR of complex 2a in d6-DMSO

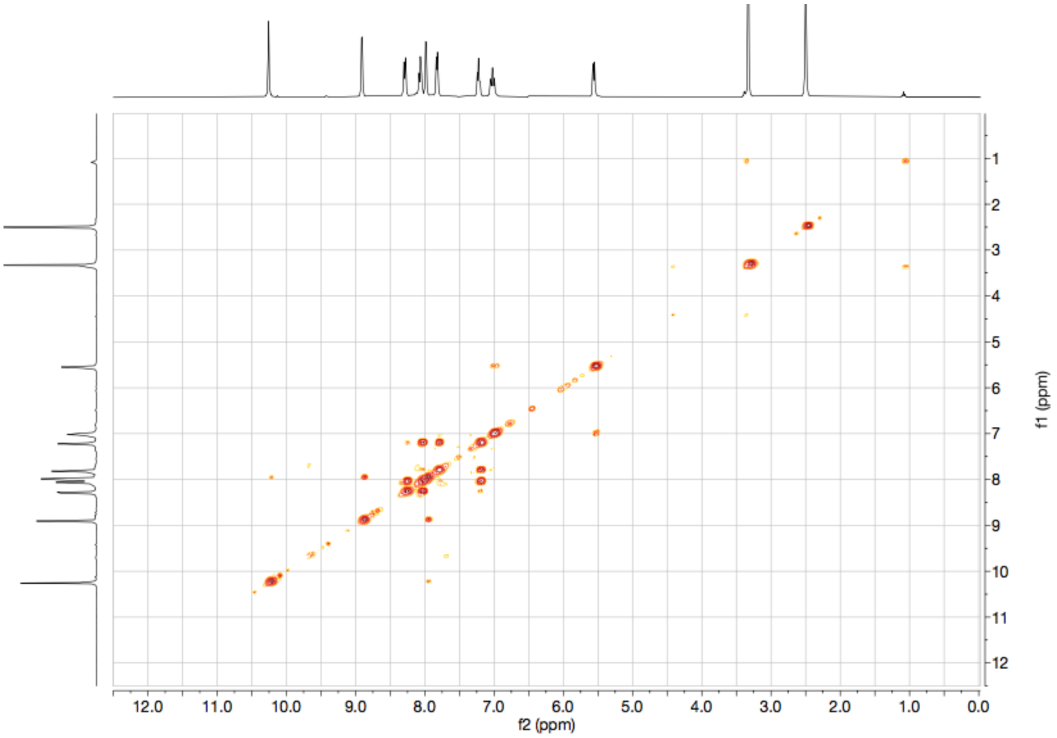

Figure 10: COSY Spectrum of complex 2a in d6-DMSO

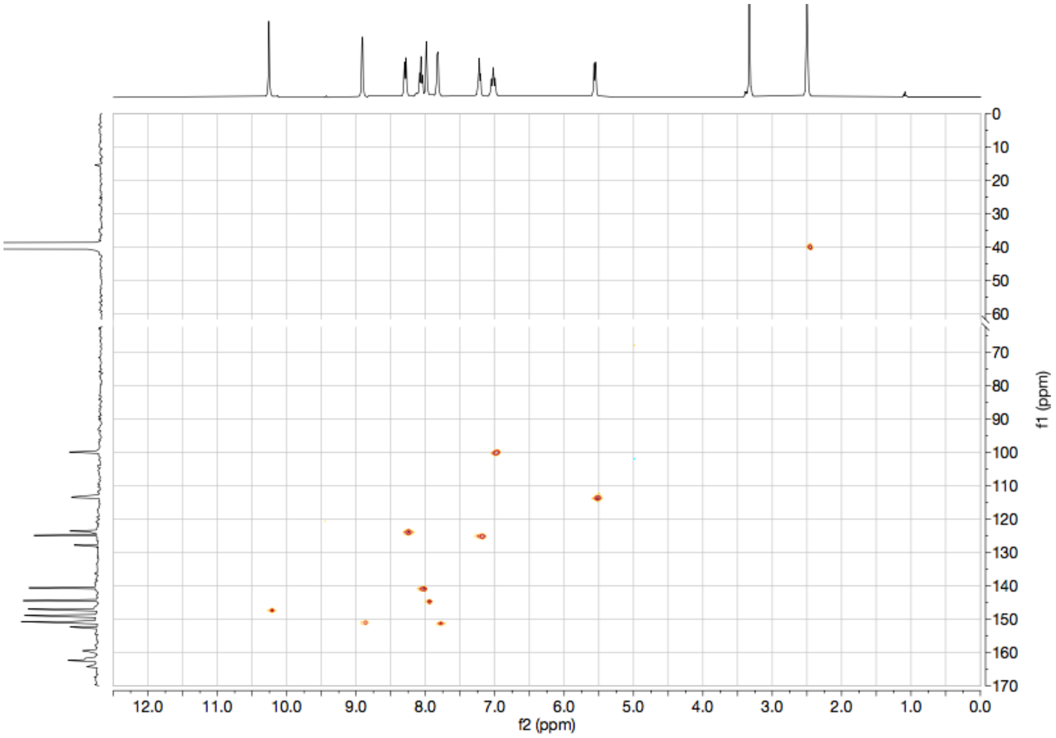

Figure 11: HSQC Spectrum of complex 2a in d6-DMSO

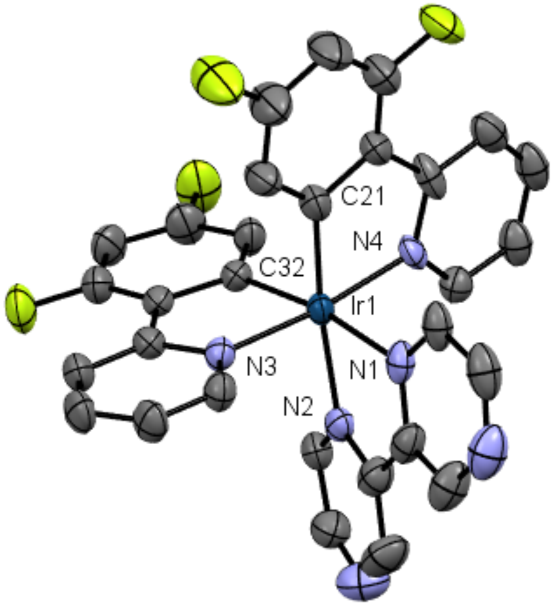

Figure 12: Single-crystal X-ray crystal structure of complex 2a. Hydrogen atoms and solvent molecules omitted for clarity

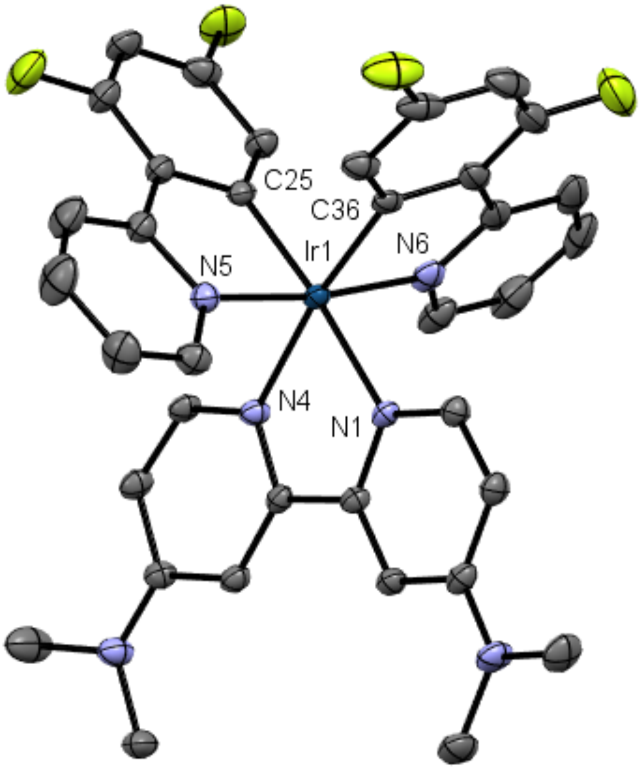

Figure 13: Single-crystal X-ray crystal structure of complex 4. Hydrogen atoms and solvent molecules omitted for clarity

Table 1: X-ray crystallography data for cationic complexes 2a and 4.

Complex #	2a	4
Empirical formula	$C_{32.5}H_{24}ClF_{10}IrN_6O_{0.5}P$	$C_{37}H_{32}Cl_2F_{10}IrN_6P$
Formula weight	955.2	1044.75
Temperature/K	100(2)	100(2)
Crystal system	triclinic	triclinic
Space group	P-1	P-1
a/Å	13.8002(6)	8.6227(9)
b/Å	14.3504(6)	13.5061(13)
c/Å	17.3147(8)	16.6738(15)
α/°	72.193(2)	104.272(3)
β/°	89.145(2)	94.651(4)
γ/°	89.584(2)	90.132(4)
Volume/$Å^3$	3264.3(3)	1875.2(3)
Z	4	2
$\rho_{calc}g/cm^3$	1.944	1.85
μ/mm^{-1}	4.316	3.834
F(000)	1856	1024
Crystal size/mm^3	0.201 × 0.122 × 0.065	0.281 × 0.264 × 0.078
Radiation	MoKα (λ = 0.71073)	MoKα (λ = 0.71073)
2Θ range for data collection/°	4.19 to 50.998	4.47 to 55.88
Index ranges	$-16 \leq h \leq 16, -17 \leq k \leq 17, -20 \leq l \leq 20$	$-11 \leq h \leq 11, -17 \leq k \leq 17, -21 \leq l \leq 21$
Reflections collected	68954	63741
Independent reflections	12132 [R_{int} = 0.0374, R_{sigma} = 0.0239]	8981 [R_{int} = 0.0401, R_{sigma} = 0.0224]
Data/restraints/parameters	12132/139/982	8981/0/518
Goodness-of-fit on F^2	1.1	1.123
Final R indexes [I>=2σ (I)]	R_1 = 0.0404, wR_2 = 0.0839	R_1 = 0.0242, wR_2 = 0.0561
Final R indexes [all data]	R_1 = 0.0513, wR_2 = 0.0944	R_1 = 0.0274, wR_2 = 0.0587
Largest diff. peak/hole / e $Å^{-3}$	2.04/-1.50	1.53/-1.11

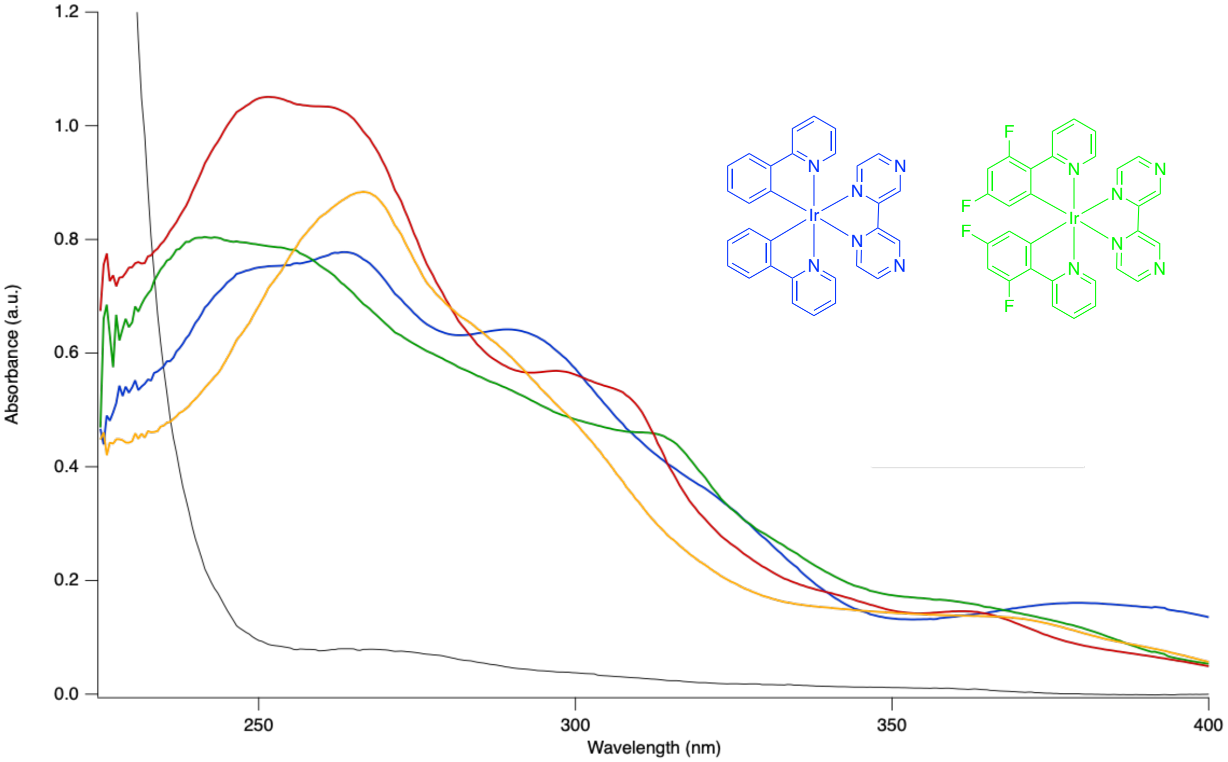

Figure 14: Absorption Spectra of Cationic Ir(III) Complexes

UV-Vis absorbance was measured for several of the cationic iridium complexes. [Fig. 14] Despite not yet successfully synthesizing the N-oxide congener for these molecules, the absorbance data was collected to determine if our compounds were qualitatively showing spectra consistent with literature. The complexes represented by the blue and green lines differ only the two fluorines on the C^N ligand. The green line represents the fluorinated complex, which shows the predicted blue-shifted absorption. The highest intensity absorbance peak around 250 nm is typically assigned to the ligand-centered (LC) transition, but the second and possibly third bands are attributed to MLCT, LLCT, or a mixture. Better resolution of peaks is needed to accurately calculate extinction coefficients, and emission data is needed to further characterize the photophysical shift resulting from various ligand structures.

Neutral N-oxide Complexes

According to **GP2**, four Ir(C^N)$_2$(N^O) complexes were synthesized successfully and characterized by ^{1}H NMR [Fig.15-18]. Generally, the asymmetry of the N^O ligands resulted in a peak for every individual proton on the molecule except for the methyl group. The expected number of peaks in the aromatic region were found in each spectrum. Since two of these complexes contain the N-oxide on the pyrazine-based ligand, the first analysis of N-oxide tuning was examining changes in shift values that might have resulted from the differing compounds. Upon closer inspection, the only significant peak different was the unexplained singlet close to 9.5 ppm.

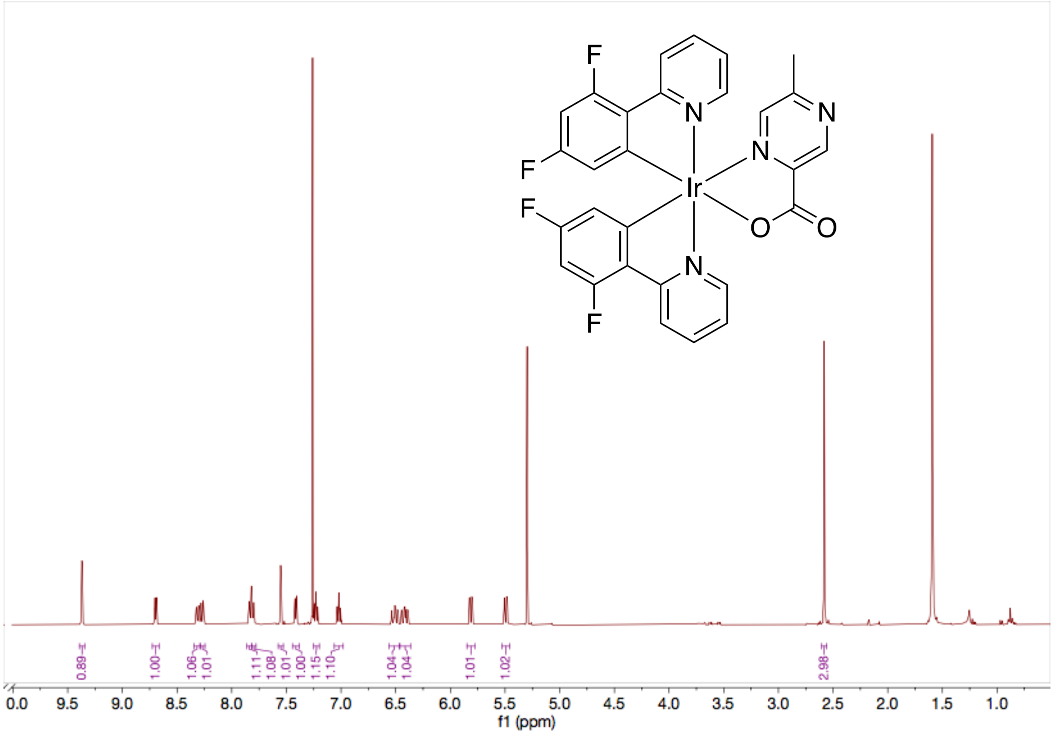

Figure 15: ^{1}H NMR of complex 6a in $CDCl_3$

The remainder of the complexes had almost identical chemical shifts to their N-oxide congener. This indicates that the success of an N-oxide reaction is not best determined by NMR alone.

However, crystals were grown with each of these complexes, which meant the presence of the N-oxide could be visualized. The work of fully characterizing these four complexes with ^{13}C and 2D NMR is ongoing.

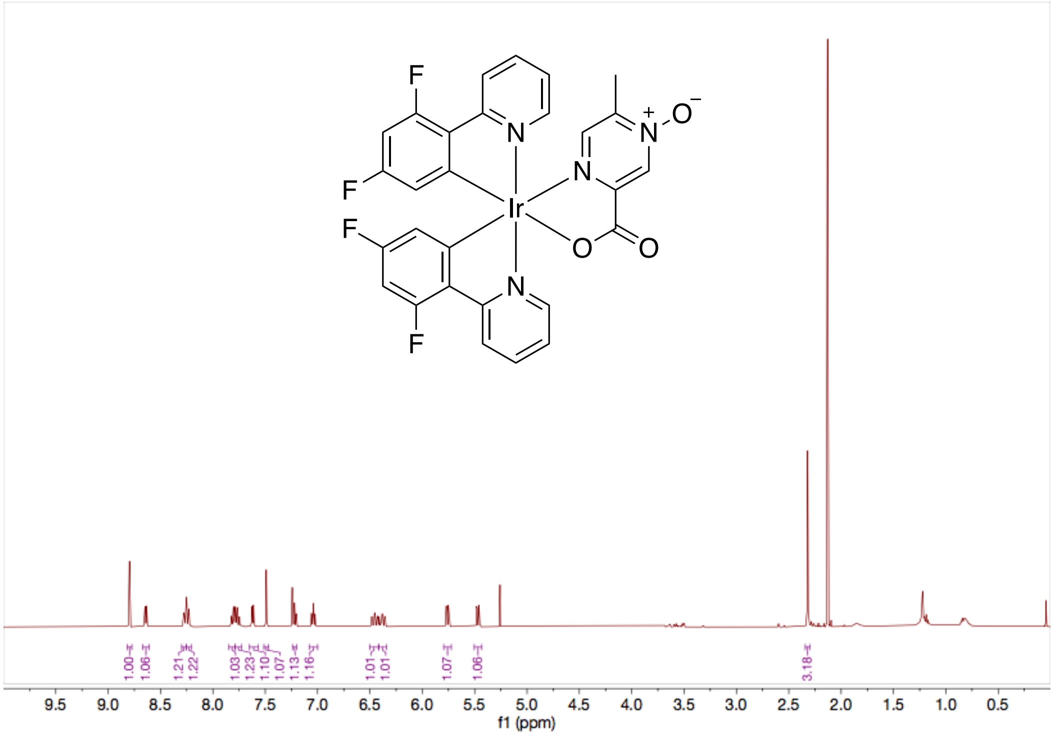

Figure 16: ^{1}H NMR of complex 6b in $CDCl_3$

The crystal structures complexes 7a and 7b are included in the main section. The remaining NMR spectra and crystal structures can be found in Appendix X. Figures 22-23 show the C^N ligands in the same positions as in the cationic complexes with the N^O disrupting the symmetry.

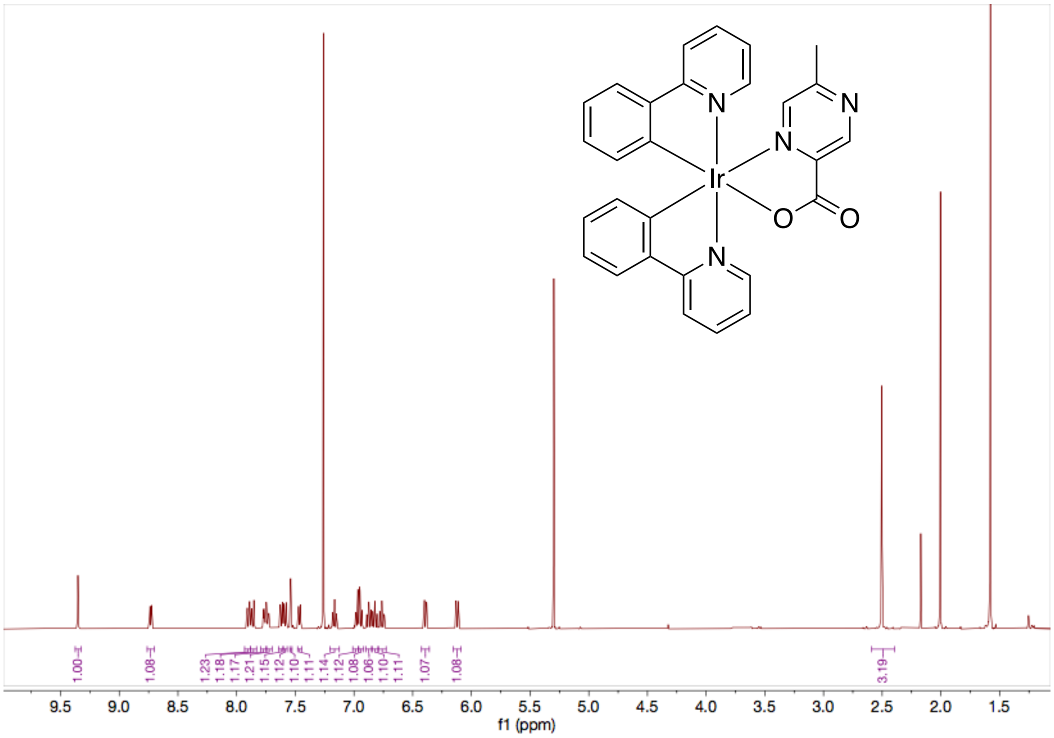

Figure 17: ^{1}H NMR of complex 7a in $CDCl_3$

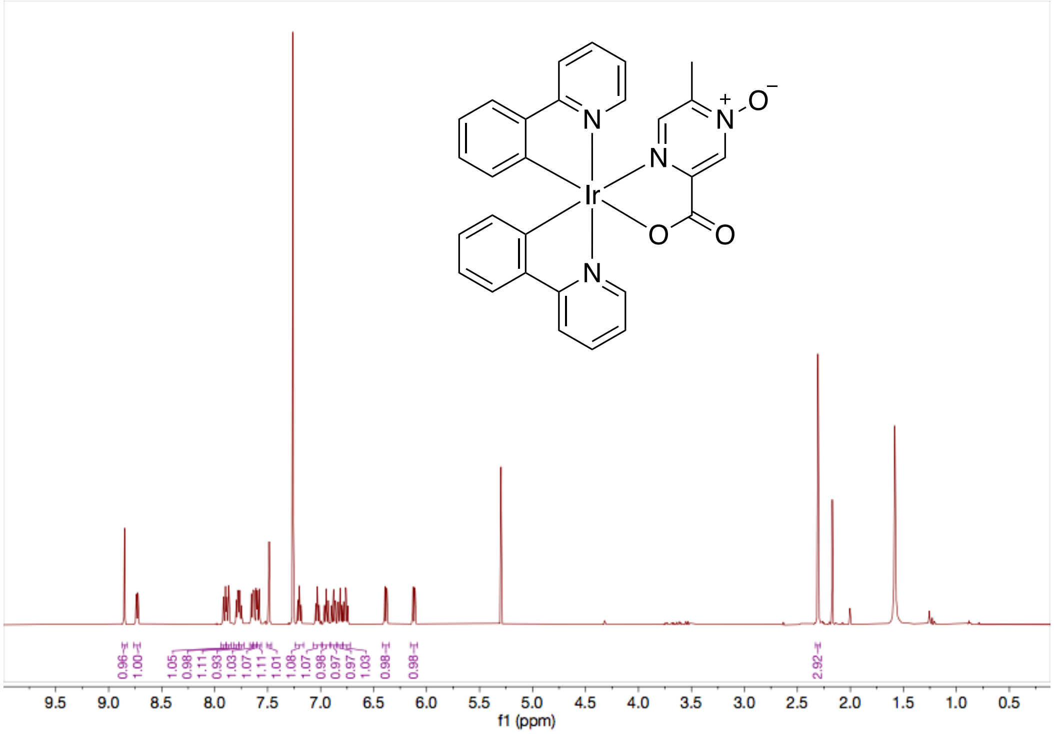

Figure 18: ^{1}H NMR of complex 7b in $CDCl_3$

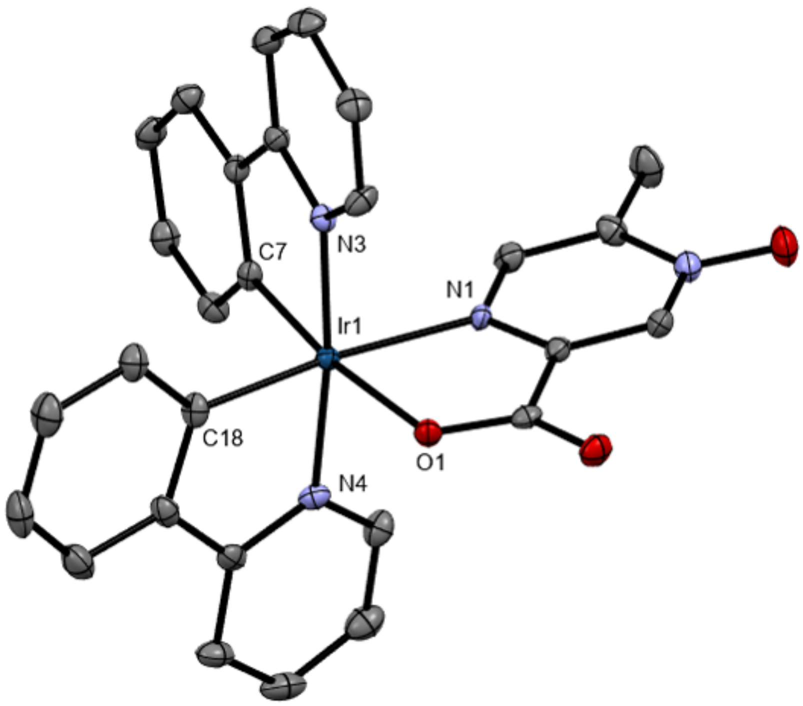

Figure 22: Single-crystal X-ray crystal structure of complex 7b. Hydrogen atoms and solvent molecules omitted for clarity

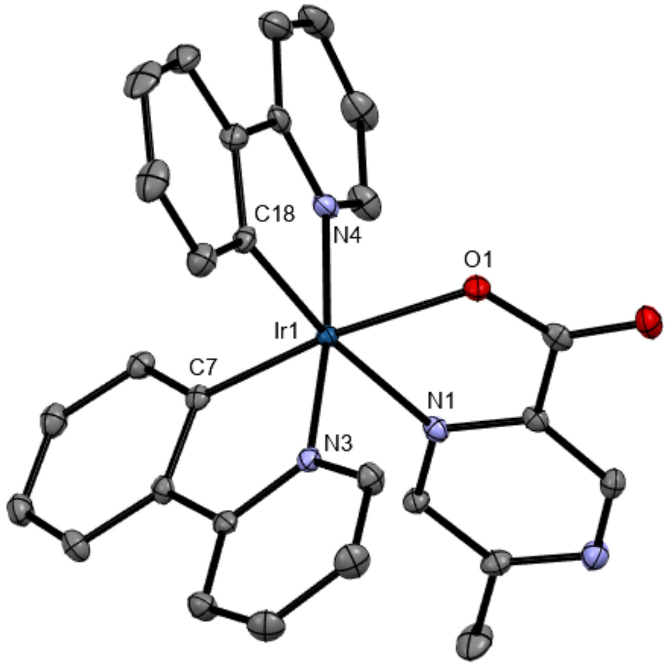

Figure 23: Single-crystal X-ray crystal structure of complex *7*a. Hydrogen atoms and solvent molecules omitted for clarity.

Table 4: X-ray crystallography data for neutral complexes 7a and 7b

Complex #	7a	7b
Empirical formula	$C_{30}H_{25}Cl_4IrN_4O_2$	$C_{30}H_{25}Cl_4IrN_4O_3$
Formula weight	807.54	823.54
Temperature/K	100(2)	100(2)
Crystal system	monoclinic	monoclinic
Space group	$P2_1$	$P2_1$
a/Å	9.3682(6)	9.3656(5)
b/Å	16.9395(10)	16.9853(8)
c/Å	9.4088(5)	9.5139(5)
α/°	90	90
β/°	91.347(2)	91.2046(18)
γ/°	90	90
Volume/Å^3	1492.69(15)	1513.11(13)
Z	2	2
ρ_{calc}g/cm^3	1.797	1.808
μ/mm^{-1}	4.866	4.804
F(000)	788	804
Crystal size/mm^3	0.223 × 0.209 × 0.165	0.177 × 0.152 × 0.054
Radiation	MoKα (λ = 0.71073)	MoKα (λ = 0.71073)
2Θ range for data collection/°	4.35 to 60.12	4.282 to 59.232
Index ranges	$-13 \leq h \leq 13$, $-23 \leq k \leq 23$, $-13 \leq l \leq 13$	$-13 \leq h \leq 13$, $-23 \leq k \leq 23$, $-13 \leq l \leq 13$
Reflections collected	33335	32766
Independent reflections	8622 [R_{int} = 0.0370, R_{sigma} = 0.0406]	8406 [R_{int} = 0.0374, R_{sigma} = 0.0440]
Data/restraints/parameters	8622/1/372	8406/1/381
Goodness-of-fit on F^2	0.946	1.038
Final R indexes [I>=2σ (I)]	R_1 = 0.0164, wR_2 = 0.0376	R_1 = 0.0204, wR_2 = 0.0439
Final R indexes [all data]	R_1 = 0.0175, wR_2 = 0.0396	R_1 = 0.0236, wR_2 = 0.0463
Largest diff. peak/hole / e Å^{-3}	0.77/-0.70	1.50/-1.16
Flack Parameter	0.015(3)	0.009(3)

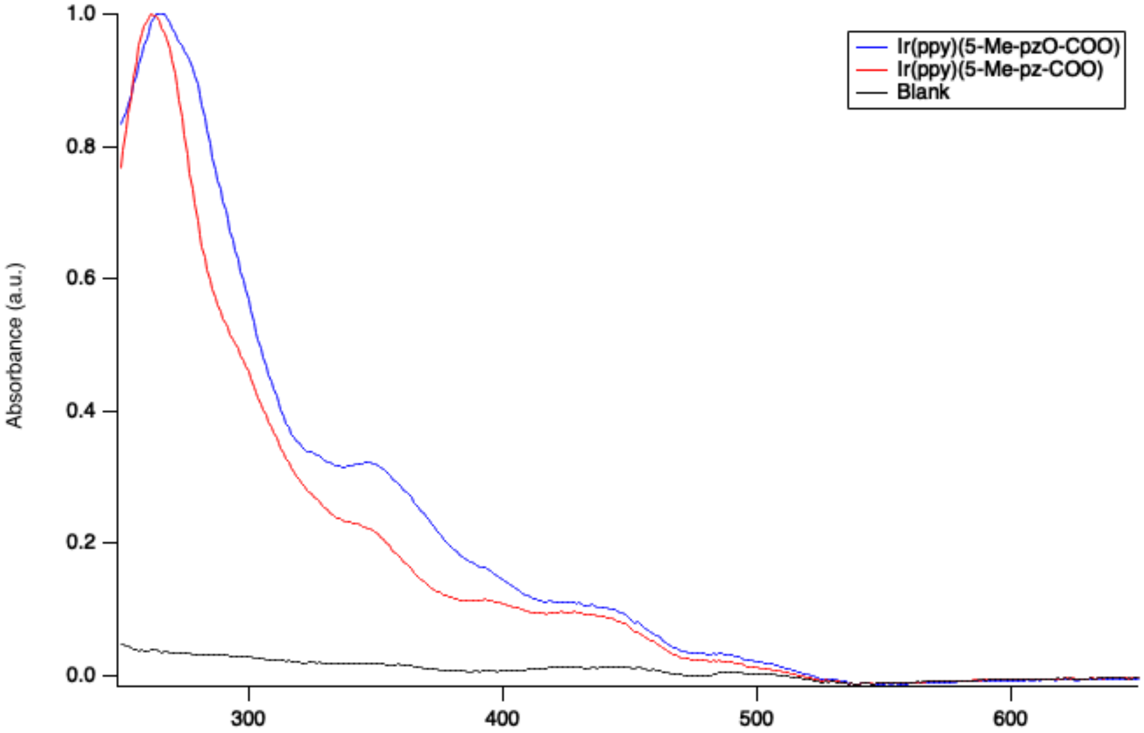

Figure 19: UV-Vis absorbance spectra from complex 7a (red) and complex 7b (blue).

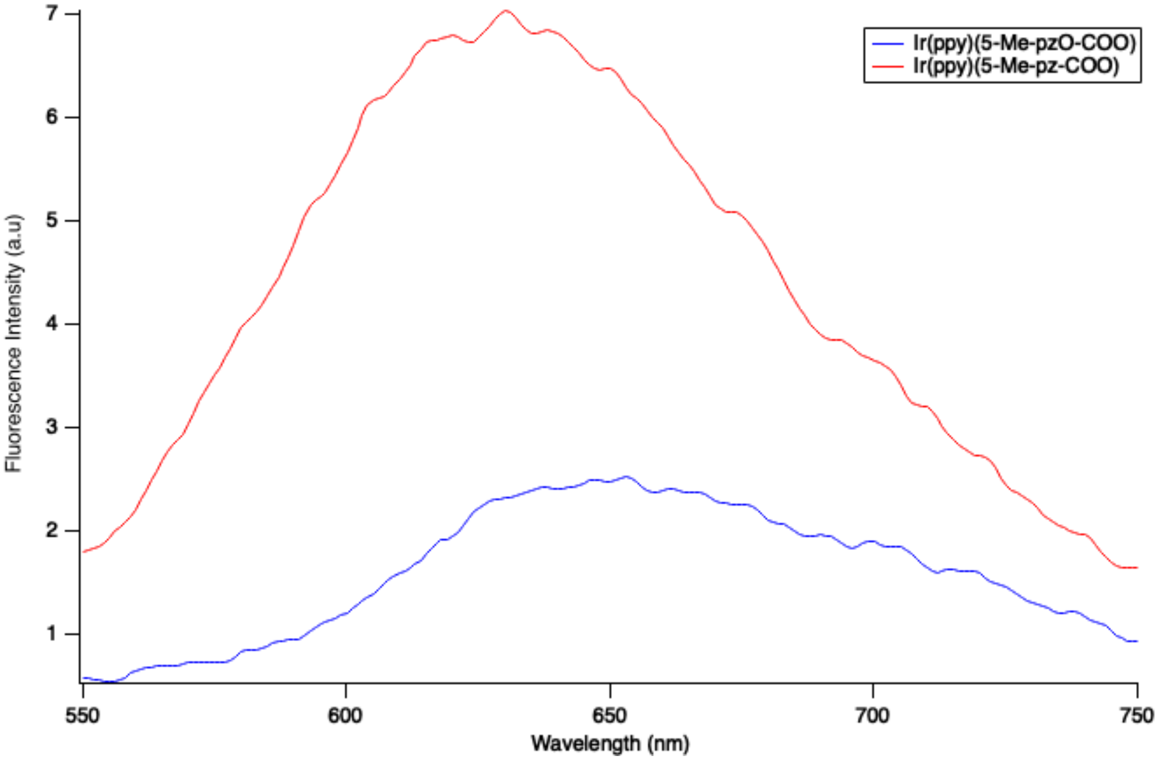

Figure 20: Emission at 280 nm for complex 7a (red) and complex 7b (blue).

Initial absorbance and emission spectra appeared similar to those reported in literature. The largest absorbance band at 263 nm is most likely due to the LC transition while the smaller, broader bands result from MLCT or a mixture of states. [Fig. 19] Because the smaller peaks were less-resolved, it was not possible to calculate accurate extinction coefficients from these data. The absorbance data in Table 2 show that the presence of the N-oxide does not significantly alter the absorbance spectra.

Table 2: UV-Vis Absorbance Data for 7a and 7b.

Complex #	Peak 1 (nm)	Abs (a.u.)	Peak 2 (nm)	Abs (a.u.)	Peak (nm)	Abs (a.u.)
7a	263	1.0	348	0.32	445	0.1
7b	265	1.0	348	0.25	445	0.8

The emission spectrum shows that the fluorescence of the complex is significantly quenched by the presence of the N-oxide. [Fig. 20] The N-oxide complex also showed an approximately 20nm red shift in emission although the broadness of the peak makes this difficult to calculate. [Table 3] This result is promising as it shows the ability of the N-oxide to tune the emission of the complex; however, a greater shift is desirable for ratiometric imaging applications. A larger shift upon interaction with cellular oxygen conditions would result in more sensitive detection of changing conditions.

Table 3: Fluorescence Data for 7a and 7b at Excitation Wavelength 263 nm.

Complex #	Emission Wavelength (nm)	Fluorescence Intensity (a.u.)
7a	629	7.2
7b	653	2.7

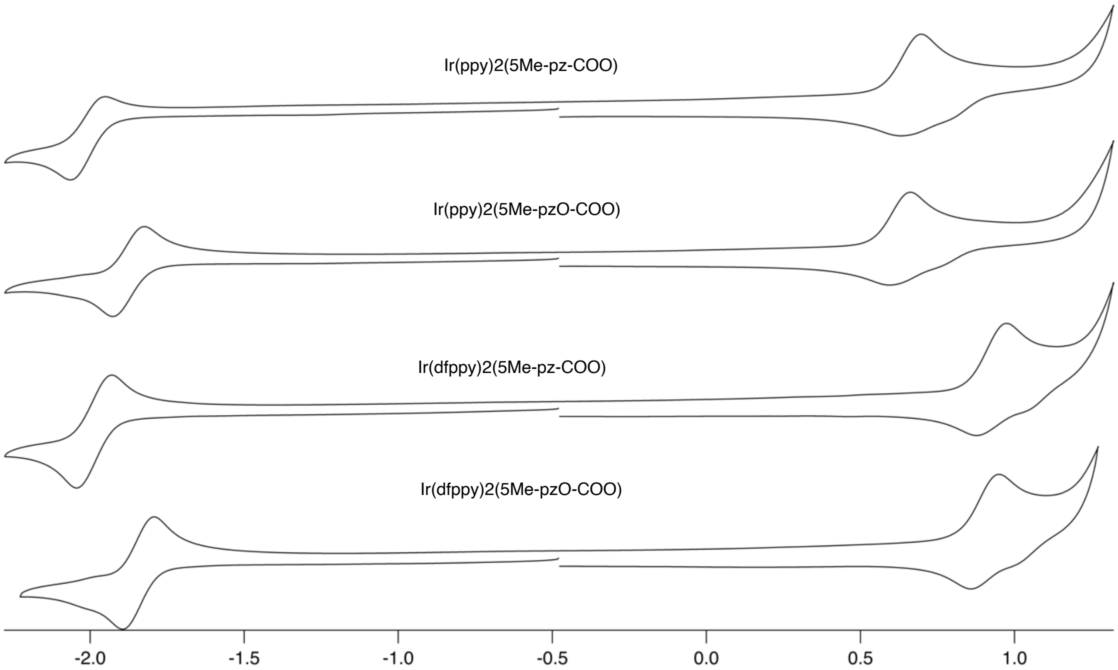

Figure 21: Cyclic Voltammogram of Ir(III) complexes and N-oxide congeners

The four complexes were studied by cyclic voltammetry in order to explore their electrochemical properties [Fig. 21] For both sets of complexes, the N-oxide congener increases reduction potential. Since this peak represents the ligand-centered reduction, the increase in reduction potential show the electron-withdrawing properties of the N-oxide. The cathodic potential does not shift significantly with the N-oxide. However, it was increased for the fluorinated complexes. As a withdrawing group, fluorine will pull electron density away from the metal, making it more difficult to oxidize. Reports of electrochemical data of similar Ir(III) complexes show that the first oxidation wave corresponds the HOMO, which~~,~~ consists of orbital contributions from the C^N ligands and the metal center. These data give further evidence to the stabilization of the HOMO by electron-withdrawing groups on the C^N ligands. The cyclic voltammogram shows that these complexes can be tuned by different groups on either set of ligands, which will help inform the optimization of ligand design for future photophysical tuning applications.

Conclusions

We have shown that cyclometalated Ir (III) complexes containing chelating ligands with external nitrogens can be efficiently synthesized. Initial characterization results comparing complexes with their N-oxide congeners show that the N-oxide does tune the photophysical and electrochemical properties of the complex. Future work on these complexes should include thorough quantification of the absorbance and emission data of a wider range of these complexes. With respect to the ability of these complexes to act as hypoxia probes, the quenching of fluorescence by the N-oxide suggests that the probe might function best in an off/on mechanism. The N-oxide probe would be synthesized and then cleaved under hypoxic conditions to turn the signal “on’. Additionally, optimization of ligand design could increase the difference between the two emission wavelengths for more sensitive ratiometric measurements. To determine the viability of this mechanism, different solutions could be screened against an N-oxide complex, including cell-like solution, to determine the conditions of N-oxide cleavage. Looking further ahead, cellular uptake and cytotoxicity studies will be necessary to test the viability of these complexes as cellular probes. The are many potential directions of this project. Since the complexes are easily synthesized with different ligand structures, many different molecules and structures within cells could potentially be targeted.

References

43. Lamansky, S.; Djurovich, P.; Murphy, D.; Abdel-Razzaq, F.; Kwong, R.; Tsyba, I.; Bortz, M.; Mui, B.; Bau, R.; Thompson, M. E., Synthesis and Characterization of Phosphorescent Cyclometalated Iridium Complexes. *Inorganic chemistry* **2001,** *40* (7), 1704-1711.10.1021/ic0008969

44. Park, H. R.; Ha, Y., Comparison of Emission Characteristics with 4-, 5-, 6-Membered Iridium Complexes for OLEDs. *Molecular Crystals and Liquid Crystals* **2012,** *563* (1), 246-256.10.1080/15421406.2012.689729

45. Housecroft, C. E.; Constable, E. C., Over the LEC rainbow: Colour and stability tuning of cyclometallated iridium(III) complexes in light-emitting electrochemical cells. *Coordination Chemistry Reviews* **2017,** *350*, 155-177.https://doi.org/10.1016/j.ccr.2017.06.016

46. Li, T.-Y.; Wu, J.; Wu, Z.-G.; Zheng, Y.-X.; Zuo, J.-L.; Pan, Y., Rational design of phosphorescent iridium(III) complexes for emission color tunability and their applications in OLEDs. *Coordination Chemistry Reviews* **2018,** *374*, 55-92.https://doi.org/10.1016/j.ccr.2018.06.014

47. You, Y.; Kim, K. S.; Ahn, T. K.; Kim, D.; Park, S. Y., Direct Spectroscopic Observation of Interligand Energy Transfer in Cyclometalated Heteroleptic Iridium(III) Complexes: A Strategy for Phosphorescence Color Tuning and White Light Generation. *The Journal of Physical Chemistry C* **2007,** *111* (10), 4052-4060.10.1021/jp0702550

48. Su, H.-C.; Chen, H.-F.; Fang, F.-C.; Liu, C.-C.; Wu, C.-C.; Wong, K.-T.; Liu, Y.-H.; Peng, S.-M., Solid-State White Light-Emitting Electrochemical Cells Using Iridium-Based Cationic Transition Metal Complexes. *Journal of the American Chemical Society* **2008,** *130* (11), 3413-3419.10.1021/ja076051e

49. Liu, Z.; Bian, Z.; Bian, J.; Li, Z.; Nie, D.; Huang, C., Acetonitrile-Vapor-Induced Color and Luminescence Changes in a Cyclometalated Heteroleptic Iridium Complex. *Inorganic Chemistry* **2008,** *47* (18), 8025-8030.10.1021/ic702141h

50. Bevernaegie, R.; Wehlin, S. A. M.; Piechota, E. J.; Abraham, M.; Philouze, C.; Meyer, G. J.; Elias, B.; Troian-Gautier, L., Improved Visible Light Absorption of Potent Iridium(III) Photo-oxidants for Excited-State Electron Transfer Chemistry. *Journal of the American Chemical Society* **2020,** *142* (6), 2732-2737.10.1021/jacs.9b12108

51. Di Marco, G.; Lanza, M.; Mamo, A.; Stefio, I.; Di Pietro, C.; Romeo, G.; Campagna, S., Luminescent Mononuclear and Dinuclear Iridium(III) Cyclometalated Complexes Immobilized in a Polymeric Matrix as Solid-State Oxygen Sensors. *Analytical Chemistry* **1998,** *70* (23), 5019-5023.10.1021/ac980234p

52. Deaton, J. C.; Castellano, F. N., Archetypal Iridium(III) Compounds for Optoelectronic and Photonic Applications. In *Iridium(III) in Optoelectronic and Photonics Applications*, 2017; pp 1-69.

53. Hasan, K.; Bansal, A. K.; Samuel, I. D. W.; Roldán-Carmona, C.; Bolink, H. J.; Zysman-Colman, E., Tuning the Emission of Cationic Iridium (III) Complexes Towards the Red Through Methoxy Substitution of the Cyclometalating Ligand. *Scientific Reports* **2015,** *5* (1), 12325.10.1038/srep12325

54. Yu, G.-X.; Lin, C.-H.; Liu, Y.-X.; Yi, R.-H.; Chen, G.-Y.; Lu, C.-W.; Su, H.-C., Efficient and Saturated Red Light-Emitting Electrochemical Cells Based on Cationic Iridium(III) Complexes with EQE up to 9.4 %. *Chemistry – A European Journal* **2019,** *25* (60), 13748-13758.https://doi.org/10.1002/chem.201902887

55. Zhao, Q.; Yu, M.; Shi, L.; Liu, S.; Li, C.; Shi, M.; Zhou, Z.; Huang, C.; Li, F., Cationic Iridium(III) Complexes with Tunable Emission Color as Phosphorescent Dyes for Live Cell Imaging. *Organometallics* **2010,** *29* (5), 1085-1091.10.1021/om900691r

56. Ladouceur, S.; Fortin, D.; Zysman-Colman, E., Enhanced Luminescent Iridium(III) Complexes Bearing Aryltriazole Cyclometallated Ligands. *Inorganic Chemistry* **2011,** *50* (22), 11514-11526.10.1021/ic2014013

57. Schneidenbach, D.; Ammermann, S.; Debeaux, M.; Freund, A.; Zöllner, M.; Daniliuc, C.; Jones, P. G.; Kowalsky, W.; Johannes, H.-H., Efficient and Long-Time Stable Red Iridium(III) Complexes for Organic Light-Emitting Diodes Based on Quinoxaline Ligands. *Inorganic Chemistry* **2010,** *49* (2), 397-406.10.1021/ic9009898

58. Lo, K. K.-W., Luminescent Rhenium(I) and Iridium(III) Polypyridine Complexes as Biological Probes, Imaging Reagents, and Photocytotoxic Agents. *Accounts of Chemical Research* **2015,** *48* (12), 2985-2995.10.1021/acs.accounts.5b00211

59. Zhang, K. Y.; Liu, S.; Zhao, Q.; Li, F.; Huang, W., Phosphorescent Iridium(III) Complexes for Bioimaging. In *Luminescent and Photoactive Transition Metal Complexes as Biomolecular Probes and Cellular Reagents*, Lo, K. K.-W., Ed. Springer Berlin Heidelberg: Berlin, Heidelberg, 2015; pp 131-180.

60. Zhang, S.; Hosaka, M.; Yoshihara, T.; Negishi, K.; Iida, Y.; Tobita, S.; Takeuchi, T., Phosphorescent Light–Emitting Iridium Complexes Serve as a Hypoxia-Sensing Probe for Tumor Imaging in Living Animals. *Cancer Research* **2010,** *70* (11), 4490-4498.10.1158/0008-5472.CAN-09-3948

61. Penconi, M.; Cazzaniga, M.; Panzeri, W.; Mele, A.; Cargnoni, F.; Ceresoli, D.; Bossi, A., Unraveling the Degradation Mechanism in FIrpic-Based Blue OLEDs: II. Trap and Detect Molecules at the Interfaces. *Chemistry of Materials* **2019,** *31* (7), 2277-2285.10.1021/acs.chemmater.8b04502

62. Guo, W.; Ding, H.; Gu, C.; Liu, Y.; Jiang, X.; Su, B.; Shao, Y., Potential-Resolved Multicolor Electrochemiluminescence for Multiplex Immunoassay in a Single Sample. *Journal of the American Chemical Society* **2018,** *140* (46), 15904-15915.10.1021/jacs.8b09422

63. Lian, P.; Wei, H.; Zheng, C.; Nie, Y.; Bian, J.; Bian, Z.; Huang, C., Synthesis, characteristics and photoluminescent properties of novel Ir–Eu heteronuclear complexes containing 2-carboxyl-pyrimidine as a bridging ligand. *Dalton Transactions* **2011,** *40* (20), 5476-5482.10.1039/C0DT01592J

64. You, Y.; Park, S. Y., Inter-Ligand Energy Transfer and Related Emission Change in the Cyclometalated Heteroleptic Iridium Complex: Facile and Efficient Color Tuning over the Whole Visible Range by the Ancillary Ligand Structure. *Journal of the American Chemical Society* **2005,** *127* (36), 12438-12439.10.1021/ja052880t

Chapter 4: Synthesis and Characterization of Tri-carbonyl Rhenium Complexes

Introduction

Tris-carbonyl rhenium complexes have been studied since the useful unique electronic state properties were first characterized in the 1970's.[65] These complexes have been employed for various inorganic applications such as electrocatalytic CO_2 reduction, photochemistry, and two-photon excitation.[66-68] Similar to the platinum and iridium complexes discussed previously, the physical and chemical properties of these Re complexes can be easily tuned by changing the ligand attached to the metal center.[39] Complexes of the form fac-Re(N^N)(CO_3)Cl have documented ^{3}MLCT and LLCT excited states, the fluorescence of which can be exploited for imaging applications.[58, 69] The effort to synthesize rhenium complexes for biological imaging is not new[70, 71], but our N-oxide approach presents a new method to tune the properties of these compounds. These complexes have the additional advantage of being IR active as a result of the CO ligands, providing an alternative way to measure changes caused by altering another ligand (e.g. N-oxide formation). Our approach to synthesizing new rhenium imaging agents involved the use of a known synthetic route[72], during which the $Re(CO)_3$(N^N)X starting material is mixed with silver triflate and the halogen is replaced by the triflate ion; in a second step, an aromatic N-ligand replaces the triflate

[Scheme 1].

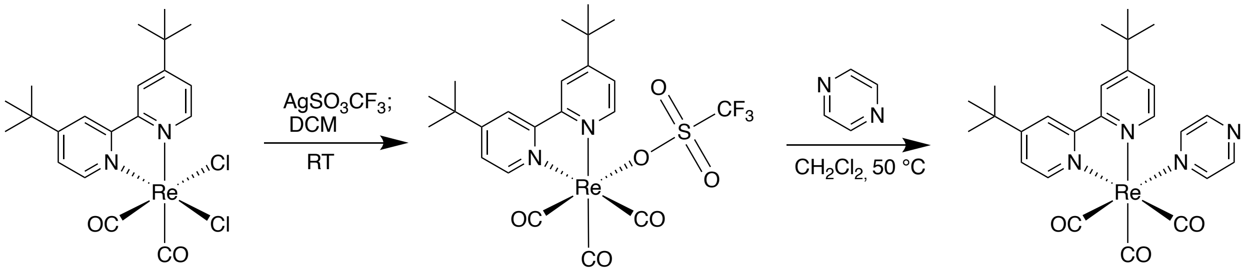

Scheme 1: Synthetic route for tris-carbonyl rhenium complexes.

To make our potential imaging agents, we used monodentate N-ligands with external nitrogens. To form the N-oxide congeners, N-oxide ligands were obtained and synthesized using the original route.

Experimental

Materials

Unless otherwise noted, all products were synthesized inside the glovebox and purified under a fume hood. Distilled solvents were used for all procedures performed inside the glovebox. All other solvents were used as received. Solvent evaporation performed using a Buchi rotovapor. Reagents including silver triflate, N-ligands, and 1,10-phenanthroline were used as purchased and stored according to label instructions. $Re(CO)_3(^t bbpy)Cl$ and $Re(CO)_3(phen)Cl$ were prepared according to previously reported procedure.[72]

Measurements

NMR spectra were obtained on a JEOL ECX 400 MHz spectrometer and referenced against TMS using residual proton signals (^1H NMR) or the ^{13}C resonances of the deuterated solvent (^{13}C NMR). Single crystal X-ray diffraction was used to determine crystal structures, and the structures were refined using the Bruker SHELXTL Software Package.

Preparation of $Re(phen)(CO)_3Cl$[72]

$Re(CO)_5Cl$ (0.5437g; 1.50 mmol) and 1,10-phenanthroline (0.2724g; 1.51 mmol) were added to dry flask along with 50 mL toluene and refluxed under N_2 atmosphere at 120 °C for 3 h. Yellow, heterogenous mixture was allowed to cool, vacuum filtered, and washed 3x10 mL with diethyl ether. Yellow solid was dried *in vacuo*. Yield: 0.4927g, 67%. ^1H NMR (400 MHz, Acetonitrile-d_3) δ 9.39 (dd, $J = 5.1, 1.4$ Hz, 2H), 8.77 (dd, $J = 8.3, 1.4$ Hz, 2H), 8.18 (s, 2H), 7.97 (dd, $J = 8.3, 5.1$ Hz, 2H).

Preparation of Re(^{t}bbpy)(CO)$_3$(pyrazine)[72]

Re(^{t}bbpy)(CO)$_3$Cl (0.1012g; 0.177mmol) and $AgSO_3CF_3$ (0.0538g; 0.209 mmol) were weighed in separate vials and brought into glovebox. Re complex dissolved in CH_2Cl_2 (5mL) and transferred to vial containing $AgSO_3CF_3$. CH_2Cl_2 (5mL) used to rinse out remaining Re compound. Vial containing yellow, heterogenous mixture sealed and left to stir for 1 h. Inside glovebox, mixture filtered through celite plug and washed with 2x10mL CH_2Cl_2. Pyrazine (PZ) (0.0138g; 0.172 mmol) weighed into vials and brought into glovebox. CH_2Cl_2 (5mL) used to dissolve PZ; solution was transferred to filter flask with Re mixture. Homogenous yellow mixture transferred to pressure tube, which was sealed and taken out of glovebox. Mixture heated to 50°C and refluxed overnight. Mixture was purified using SiO_2 column eluted with 5% MeOH/ CH_2Cl_2. 3 yellow fractions were collected, and solvent was evaporated. Product sonicated with Et_2O and filtered. ^{1}H NMR (400 MHz, Chloroform-*d*) δ 8.84 (dd, J = 5.9, 0.6 Hz, 2H), 8.72 (m, 2H), 8.58 (d, J = 2.0 Hz, 2H), 8.27 (m, 2H), 7.65 (dd, J = 5.9, 2.0 Hz, 2H), 1.56 (s, 2H), 1.50 (s, 9H).

Preparation of Re(^{t}bbpy)(CO)$_3$(pyrazine oxide)

Re(^{t}bbpy)(CO)$_3$Cl (0.1006g; 0.175 mmol) and $AgSO_3CF_3$ (0.0451g; 0.176 mmol) were weighed in separate vials and brought into glovebox. Re complex dissolved in CH_2Cl_2 (3mL) and transferred to vial containing $AgSO_3CF_3$. CH_2Cl_2 used to rinse out remaining Re compound; solution brought to a total volume of 10mL. Vial containing yellow, heterogenous mixture sealed and left to stir for 1 h. Lack of liquid N_2 prevented the solution from being filtered inside the glovebox. Instead, yellow solution was vacuum filtered inside a fume hood, using dried CH_2Cl_2 that was purged with N_2. Pyrazine oxide (0.072g; 0.179 mmol) was dissolved in 5mL dried CH_2Cl_2 and added to filtrate. Solution was transferred to a pressure tube, and the mixture was refluxed at 50°C overnight. Solution allowed to cool, and solvent evaporated. ^{1H} NMR taken in $CDCl_3$ indicated that the desired product formed despite procedure changes. Mixture was purified using SiO_2 column eluted with CH_2Cl_2 (100 mL) and 5% MeOH/ CH_2Cl_2 (200 mL). Three yellow fractions (#7-9) were collected, and solvent was evaporated. Product redissolved in CH_2Cl_2 and added to chilled hexanes. Precipitate filtered and dried *in vacuo*. ^1H NMR (400 MHz, Chloroform-*d*) δ 8.85 (dd, *J* = 5.9, 0.6 Hz, ^{2H}), 8.54 (d, *J* = 1.9 Hz, 2H), 8.09 (m, 2H), 8.00 (m, 2H), 7.66 (dd, *J* = 5.9, 2.0 Hz, 2H), 1.49 (s, 9H).

Attempted preparation of pyrazine oxide

Pyrazine (0.4013g; 5.01 mmol) and *m*-CPBA (1.4738g; 8.54 mmol) were added to flask with dried CH_2Cl_2 (10mL) and stirred under Ar for 20 h. CH_2Cl_2 (20mL) added to white, heterogenous mixture, which was filtered to separate white crystalline precipitate and colorless filtrate. Precipitate was found to be *m*-CPBA starting material. Filtrate dried with $MgSO_4$, filtered, and solvent was evaporated to form white solid. TLC in 1% MeOH/ CH_2Cl_2 and 5% MeOH/ CH_2Cl_2. White solid purified using SiO_2 column, loaded with CH_2Cl_2 and eluted with 5% MeOH/ CH_2Cl_2. Fractions 6-8 collected, and solvent was evaporated. Product sonicated with hexanes (40mL), filtered, and dried *in vacuo.* Extraction of 100mg of product dissolved in CH_2Cl_2 (10mL) with 3x30mL washes of $NaHCO_3$ was performed to remove excess *m*-CPBA. Upon further analysis, all product was lost in aqueous layer.

Preparation of Re(^{t}bbpy)$(CO)_3$(pyrazine oxide)

Re(^{t}bpy)$(CO)_3$Cl (0.1154g; 0.201 mmol) and $AgSO_3CF_3$ (0.0531g; 0.207mmol) were weighed in separate vials and brought into glovebox. Rhenium complex dissolved in CH_2Cl_2 (5mL) and transferred to vial containing $AgSO_3CF_3$. CH_2Cl_2 (5mL) used to rinse out remaining Re compound. Vial containing yellow, heterogenous mixture sealed and left to stir for 1 h. Inside glovebox, mixture filtered through celite plug and washed with 2x10mL CH_2Cl_2. Pyrazine oxide (PZO) (0.0222g; 0.231 mmol) weighed into vials and brought into glovebox. CH_2Cl_2 (5mL) used to dissolve pyrazine oxide; solution was transferred to filter flask with Re mixture. Homogenous yellow mixture transferred to pressure tube, which was sealed and taken out of glovebox. Mixture heated to 50°C and refluxed overnight. Mixture was purified using SiO_2 column eluted with CH_2Cl_2 (50mL), 1% MeOH/ CH_2Cl_2 (100mL), then 5% MeOH/ CH_2Cl_2 (200 mL). Four yellow fractions were collected, and solvent was evaporated. Product sonicated with Hexanes and filtered. ^1H NMR (400 MHz, Chloroform-*d*) δ 8.85 (d, *J* = 5.9 Hz, 2H), 8.53 (d, *J* = 1.9 Hz, 2H), 8.10 (m, 2H), 8.00 (m, 2H), 7.67 (dd, *J* = 5.9, 1.9 Hz, 2H), 1.49 (s, 9H).

Preparation of Re(phen)(CO)$_3$(pyrazine)

Re(phen)$(CO)_3$Cl (0.1011g; 0.208 mmol) and $AgSO_3CF_3$ (0.0587g; 0.229 mmol) were weighed in separate vials and brought into glovebox. Re complex dissolved in CH_2Cl_2 (5mL) and transferred to vial containing $AgSO_3CF_3$. CH_2Cl_2 (5mL) used to rinse out remaining Re compound. Vial containing yellow, heterogenous mixture sealed and left to stir for 1 h. Inside glovebox, mixture filtered through celite plug and washed with 2x10mL CH_2Cl_2. Pyrazine (PZ) (0.01670g; 0.209 mmol) weighed into vials and brought into glovebox. CH_2Cl_2 (5mL) used to dissolve PZ; solution was transferred to filter flask with Re mixture. Homogenous yellow mixture transferred to pressure tube, which was sealed and taken out of glovebox. Mixture heated to 50°C and refluxed overnight. Mixture was purified using SiO_2 column eluted with CH_2Cl_2 (50mL), 1% MeOH/ CH_2Cl_2 (100mL), then 5% MeOH/ CH_2Cl_2 (200 mL). 4 yellow fractions were collected, and solvent was evaporated. Product sonicated with Et_2O and filtered. ^1H NMR (400 MHz, DMSO-d_6) δ 9.70 (dd, *J* = 5.1, 1.4 Hz, 2H), 9.05 (dd, *J* = 8.3, 1.4 Hz, 2H), 8.34 (s, 2H), 8.32 (m, 2H), 8.24 (dd, *J* = 8.3, 5.1 Hz, 2H), 8.12 (m, 2H).

Preparation of Re(phen)(CO)$_3$(DMAP)

Re(phen)(CO)$_3$Cl (0.1006g; 0.207 mmol) and AgSO$_3$CF$_3$ (0.0539g; 0.210 mmol) were weighed in separate vials and brought into glovebox. Re complex dissolved in CH$_2$Cl$_2$ (5mL) and transferred to vial containing AgSO$_3$CF$_3$. CH$_2$Cl$_2$ (5mL) used to rinse out remaining Re compound. Vial containing yellow, heterogenous mixture sealed and left to stir for 1 h. Inside glovebox, mixture filtered through celite plug and washed with 2x10mL CH$_2$Cl$_2$. Dimethyl amino pyridine (DMAP) (0.0282g; 0.231 mmol) weighed into vials and brought into glovebox. CH$_2$Cl$_2$ (5mL) used to dissolve DMAP; solution was transferred to filter flask with Re mixture. Homogenous yellow mixture transferred to pressure tube, which was sealed and taken out of glovebox. Mixture heated to 50°C and refluxed overnight. Mixture was purified using SiO$_2$ column eluted with 5% MeOH/ CH$_2$Cl$_2$. 4 yellow fractions were collected, and solvent was evaporated. Product sonicated with Et$_2$O, filtered, and dried *in vacuo*. Yellow crystals obtained through layering of CH$_2$Cl$_2$, acetone, and hexanes in an NMR tube. ^{1}H NMR (400 MHz, Chloroform-*d*) δ 9.47 (dd, J = 5.1, 1.4 Hz, 2H), 8.86 (dd, J = 8.3, 1.4 Hz, 2H), 8.22 (s, 2H), 8.12 (dd, J = 8.3, 5.1 Hz, 2H), 7.54 (m, 2H), 6.25 (m, 2H), 2.87 (s, 3H).

Crystallography Data Collection

All attempted crystal experiments employed layering or vapor-vapor diffusion where the complex was dissolved in CH$_2$Cl$_2$ and crystallized with hexanes of Et$_2$O. All crystal structures shown were determined and refined in collaboration with Dr. Colin McMillen at Clemson University.

Results and Discussion

Four Re(I)(N^N)(CO)3N complexes were successfully synthesized and characterized by ^{1}H NMR. The complexes detailed in this chapter did not have previously published crystal structures or ^{13}C NMR spectra available to comparison. Thus, synthetic and NMR characterization are the only data to report thus far. Although little deviation from literature procedure was necessary to make the complexes, the purification process required large amounts of solvent for the small amount of product made. Yields were not calculated for majority of the complexes because so little product was able to be isolated from the filter paper from the last step of purification. Due to the volume of different products made, only three representative complexes will be discussed in detail; the remaining tabulated NMR spectra can be found in Appendix B.

The number of distinct peaks shown on each NMR spectra confirm the symmetry of the rhenium complexes. The successful synthesis of Re$^{(t}$bbpy)(CO)$_3$(pyrazine) and its N-oxide congener Re(^{t}bbpy)(CO)$_3$(pyrazine oxide) allows us to compare the effects of the additional oxygen. In Figure 3, peaks A and E are de-shielded, most likely corresponding to the hydrogens on the pz-O ligand; this is expected due to the electron-withdrawing effects of the oxygen. Peaks A and E were also calculated to be doublets, with matches with the simpler coupling interactions expected on the pyrazine ligand compared to ^{t}bbpy. The synthesis of Re(^{t}bbpy)(CO)$_3$(pyrazine oxide) was attempted twice, but the second synthesis (see Experimental; Appendix B) used a synthesized version of the PZ-O ligand with significant impurities (see *Attempted Preparation of pyrazine oxide).* Thus, the complex synthesized with the pure ligand should be used for analysis.

A synthetic challenge during this project was the separation of the Re starting material from the desired product. Although excess ligand eluted quickly, the Re(N^N)(CO)$_3$Cl band stayed close to the product band in the column. Because of this, large amounts of eluent were required for sufficient separation. In addition, other studies have isolated the Re complex intermediate with the triflate ion, but the procedure we used did not contain and intermediate purification step; therefore, additional impurities on the NMR Spectra could be attributed to this problem. Looking at the enhanced section in Figure 4, we clearly see 4 peaks corresponding to the Re(CO)$_3$(phen)(Cl) starting material, smaller than our product peaks but almost identical multiplicities, exhibiting poor purification.

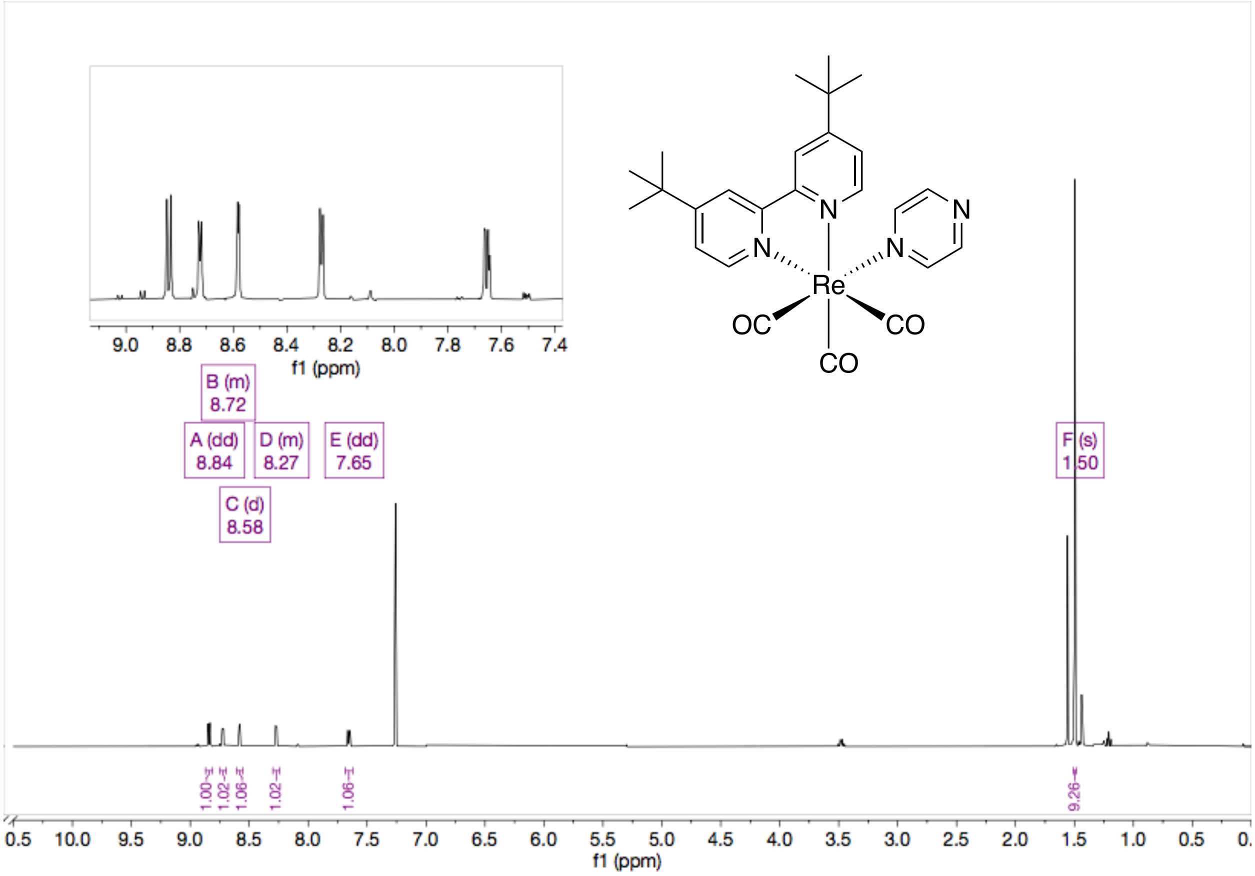

Figure 5: 1H NMR of Re(^{t}bbpy)(CO)$_3$(pyrazine) in CDCl$_3$

As mentioned in the introduction, these syntheses produce small yields that were difficult to separate from starting material; this presents a major hurdle to further characterization.

Also of note is the *fac* confirmation of the rhenium complexes as shown in Figure 5. The bond angle shown in Table 1 show an octahedral complex where there is a roughly 90° angle between the DMAP ligand and the phenanthroline ligand. We obtained no data to suggest that a proportion of a different confirmation was being formed; this aligns with the complexes synthesize in the literature. The position of the N-ligand in relation to the phenanthroline and ^{t}bbpy ligands should encourage the existence of LLCT excited states in these complexes that may be tuned with an N-oxide. Since a crystal structure of the N-oxide complex has not yet been obtained, it unclear if the Re is bound to the nitrogen or the oxygen end of the ligand.

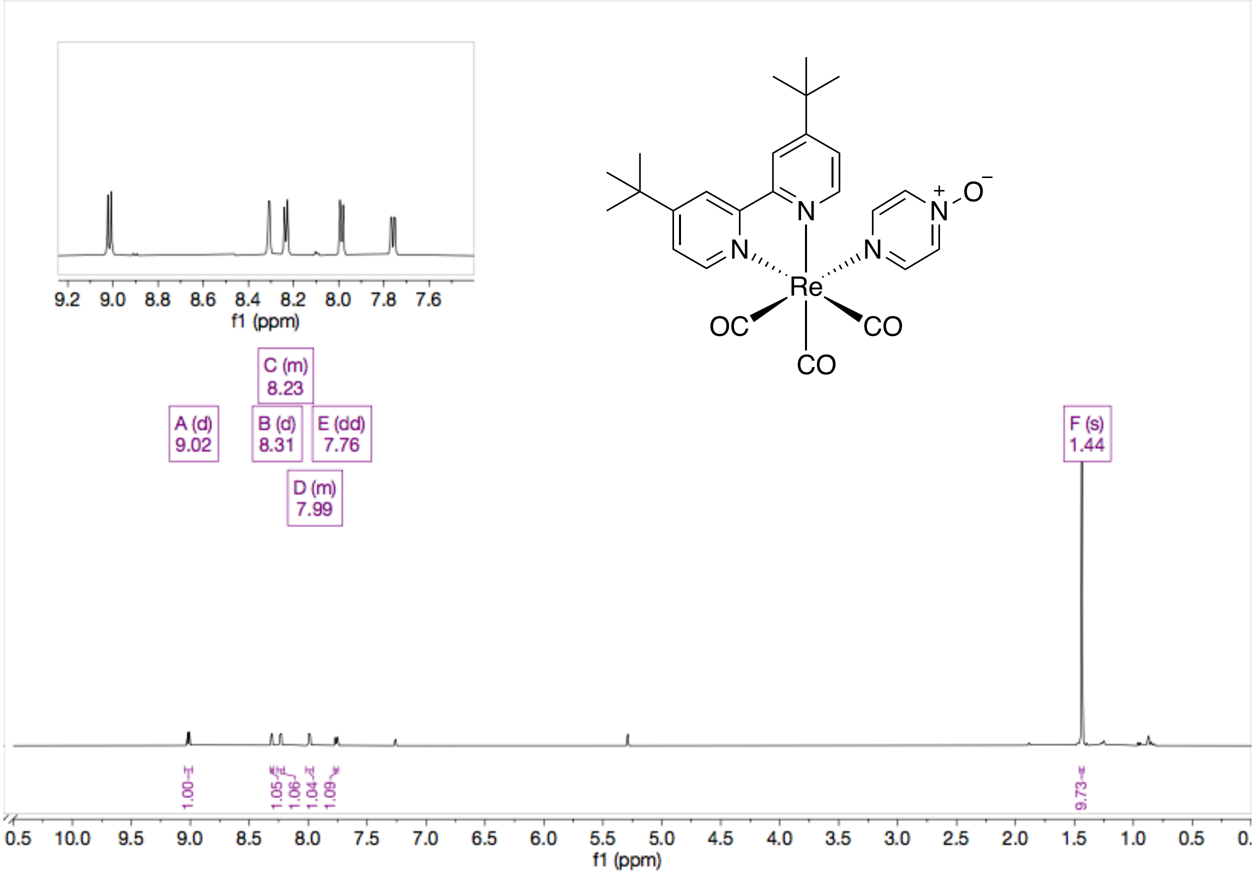

Figure 6: ^{1}H NMR of Re(^{t}bbpy)(CO)$_3$(pyrazine oxide) in CDCl$_3$

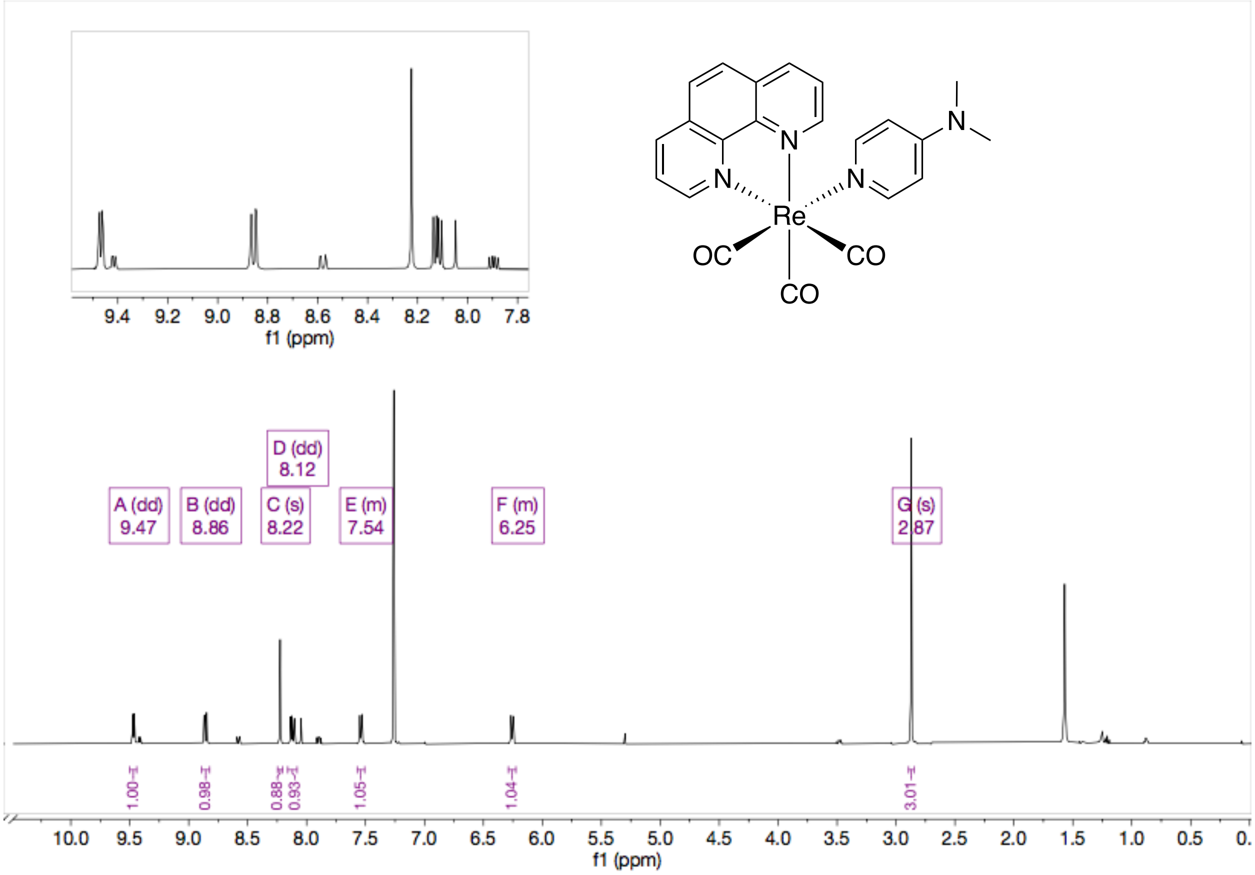

Figure 7: ^{1}H NMR of Re(CO)$_3$(phen)(DMAP)

Table 1: Crystallography Bond Angle for Re(CO)$_3$(phen)(DMAP)

Bond	Angle	Bond	Angle
C2-Re1-C3	86.68(16)	C2-Re1-C1	88.56(16)
C3-Re1-C1	89.34(16)	C2-Re1-N4	99.18(14)
C3-Re1-N4	173.70(14)	C1-Re1-N4	93.11(14)
C2-Re1-N3	174.81(13)	C3-Re1-N3	97.63(14)
C1-Re1-N3	94.35(14)	N4-Re1-N3	76.40(11)
C2-Re1-N1	92.67(13)	C3-Re1-N1	93.22(13)
C1-Re1-N1	177.22(14)	N4-Re1-N1	84.23(11)
N3-Re1-N1	84.24(11)	C6-Re2-C5	88.99(15)
C6-Re2-C4	89.79(15)	C5-Re2-C4	88.20(14)

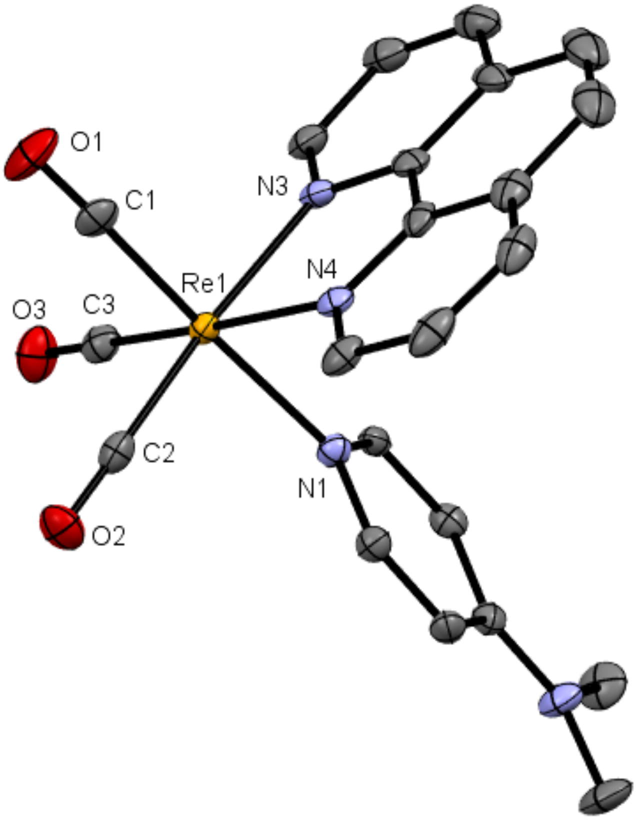

Figure 8: Single-crystal X-ray crystal structure of $Re(CO)_3$(phen)(DMAP). Hydrogen atoms and solvent molecule omitted for clarity.

Table 2. Crystal data and structure refinement for $Re(CO)_3$(phen)(DMAP)	
Identification code	d8-5378-C22H18N4O3Re-SO3CF3-CH2Cl2
Empirical formula	$C_{23.33}H_{18.67}Cl_{0.67}F_3N_4O_6ReS$
Formula weight	749.98
Temperature/K	100(2)
Crystal system	monoclinic
Space group	$P2_1/c$
a/Å	10.8561(9)
b/Å	17.6837(13)
c/Å	40.272(4)
α/°	90
β/°	91.981(3)
γ/°	90
Volume/Å^3	7726.6(11)
Z	12
ρ_{calc}g/cm^3	1.934

μ/mm^{-1}	4.937
F(000)	4368.0
Crystal size/mm^3	0.188 × 0.162 × 0.074
Radiation	MoKα (λ = 0.71073)

Conclusion

Although the successful synthesis of these rhenium complexes along with N-oxide congeners is a promising step towards new imaging agents, much more optimization of the synthesis and purification needs to be completed to make enough product to characterize. Since rhenium is quite expensive metal, efficient use of the starting material is vital to the success of this project. Preliminary NMR show that N-oxides may have different properties than their counterparts, but more characterization is needed to determine whether they can be tuned enough for imaging applications. Future work on this project will involve extensive UV-Vis, Fluorescence, and CV characterization. Computational calculations would also be a useful for analysis of the different electronic states tuned by the N-oxide.

References

65. Wrighton, M.; Morse, D. L., Nature of the lowest excited state in tricarbonylchloro-1,10-phenanthrolinerhenium(I) and related complexes. *Journal of the American Chemical Society* **1974,** *96* (4), 998-1003.10.1021/ja00811a008

66. Franco, F.; Cometto, C.; Garino, C.; Minero, C.; Sordello, F.; Nervi, C.; Gobetto, R., Photo- and Electrocatalytic Reduction of CO2 by [Re(CO)3{α,α′-Diimine-(4-piperidinyl-1,8-naphthalimide)}Cl] Complexes. *European Journal of Inorganic Chemistry* **2015,** *2015* (2), 296-304.https://doi.org/10.1002/ejic.201402912

67. Wenger, O. S.; Henling, L. M.; Day, M. W.; Winkler, J. R.; Gray, H. B., Photoswitchable Luminescence of Rhenium(I) Tricarbonyl Diimines. *Inorganic Chemistry* **2004,** *43* (6), 2043-2048.10.1021/ic030324z

68. Bronner, C.; Wenger, O. S., Proton-coupled electron transfer between 4-cyanophenol and photoexcited rhenium(I) complexes with different protonatable sites. *Inorg Chem* **2012,** *51* (15), 8275-83.10.1021/ic300834c

69. Coleman, A.; Brennan, C.; Vos, J. G.; Pryce, M. T., Photophysical properties and applications of Re(I) and Re(I)–Ru(II) carbonyl polypyridyl complexes. *Coordination Chemistry Reviews* **2008,** *252* (23), 2585-2595.https://doi.org/10.1016/j.ccr.2008.07.001

70. Ranasinghe, K.; Handunnetti, S.; Perera, I. C.; Perera, T., Synthesis and characterization of novel rhenium(I) complexes towards potential biological imaging applications. *Chem Cent J* **2016,** *10*, 71-71.10.1186/s13065-016-0218-4

71. Amoroso, A. J.; Coogan, M. P.; Dunne, J. E.; Fernández-Moreira, V.; Hess, J. B.; Hayes, A. J.; Lloyd, D.; Millet, C.; Pope, S. J. A.; Williams, C., Rhenium fac tricarbonyl bisimine complexes: biologically useful fluorochromes for cell imaging applications. *Chemical Communications* **2007,** (29), 3066-3068.10.1039/B706657K

72. Guerrero, J.; Piro, O. E.; Wolcan, E.; Feliz, M. R.; Ferraudi, G.; Moya, S. A., Photochemical and Photophysical Reactions of fac-Rhenium(I) Tricarbonyl Complexes. Effects from Binucleating Spectator Ligands on Excited and Ground State Processes. *Organometallics* **2001,** *20* (13), 2842-2853.10.1021/om000784p

Appendix A: Additional Iridium Characterization

The large number of compounds synthesized in this project has produced even larger amounts of data to collect and analyze. As mentioned previously, the compounds detailed in this report were new compounds without published NMR spectra and crystal structures. Thus, much of the data shown here and in the main chapters will be further analyzed for future publications. The NMR spectra and crystal structures shown are important for future analysis, but for conciseness they were omitted from the main Results and Discussion.

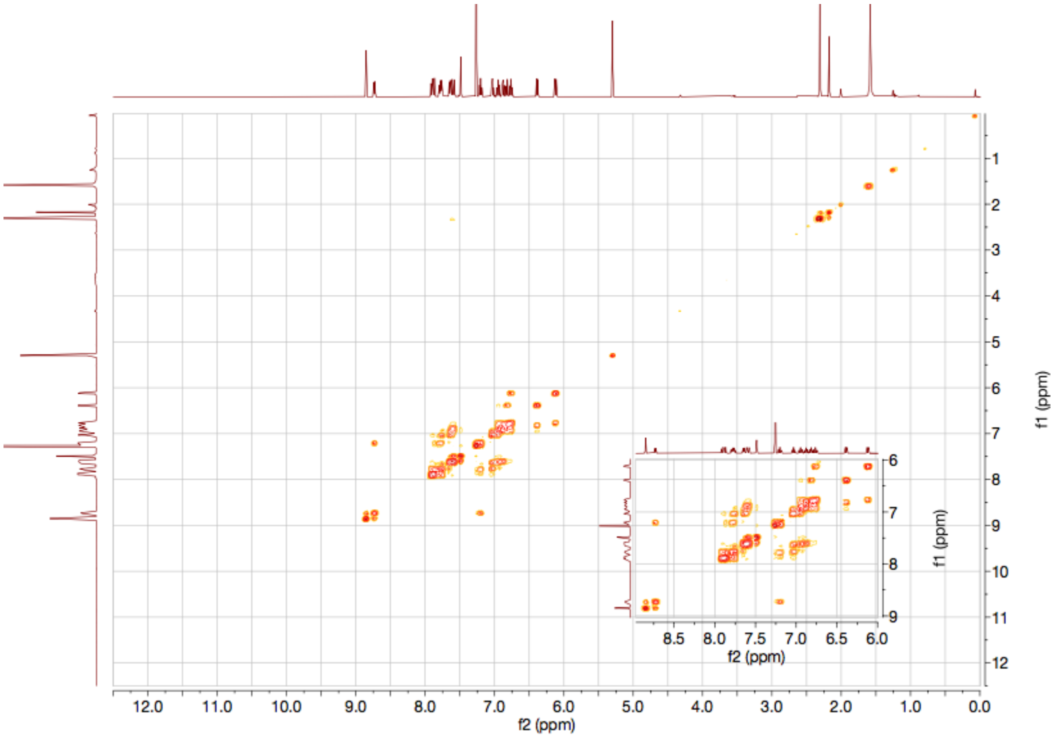

Figure 9: COSY Spectrum of 7b in $CDCl_3$

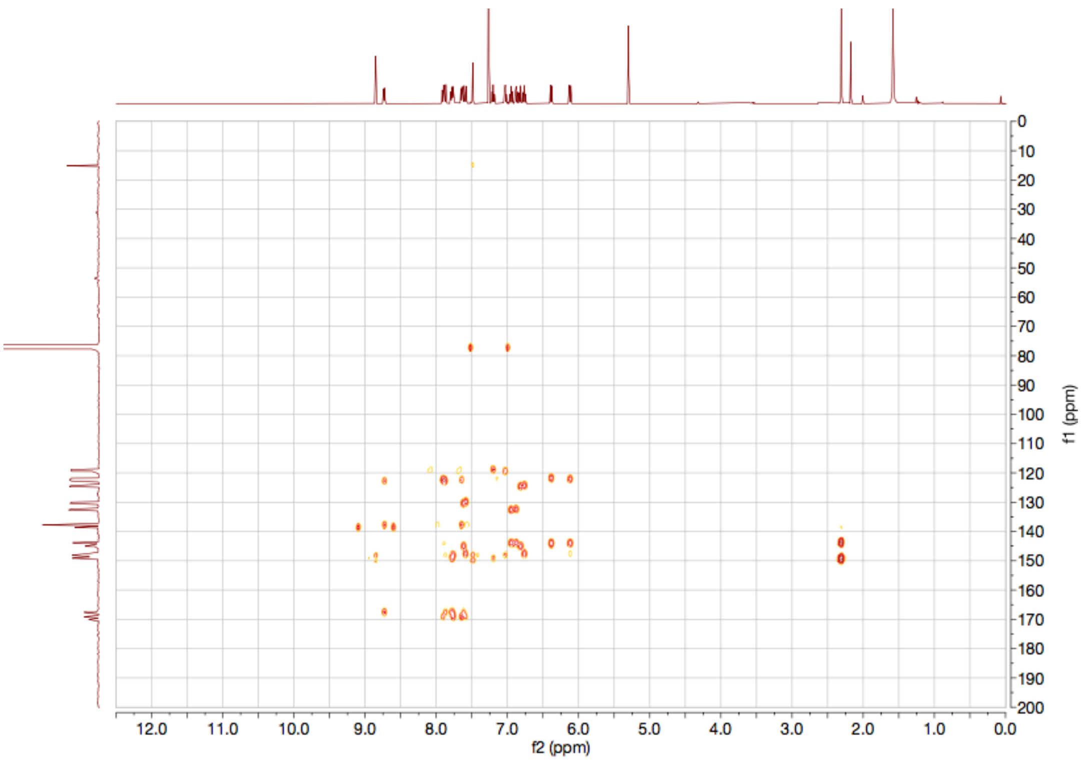

Figure 10: HMBC of 7b CDCl3

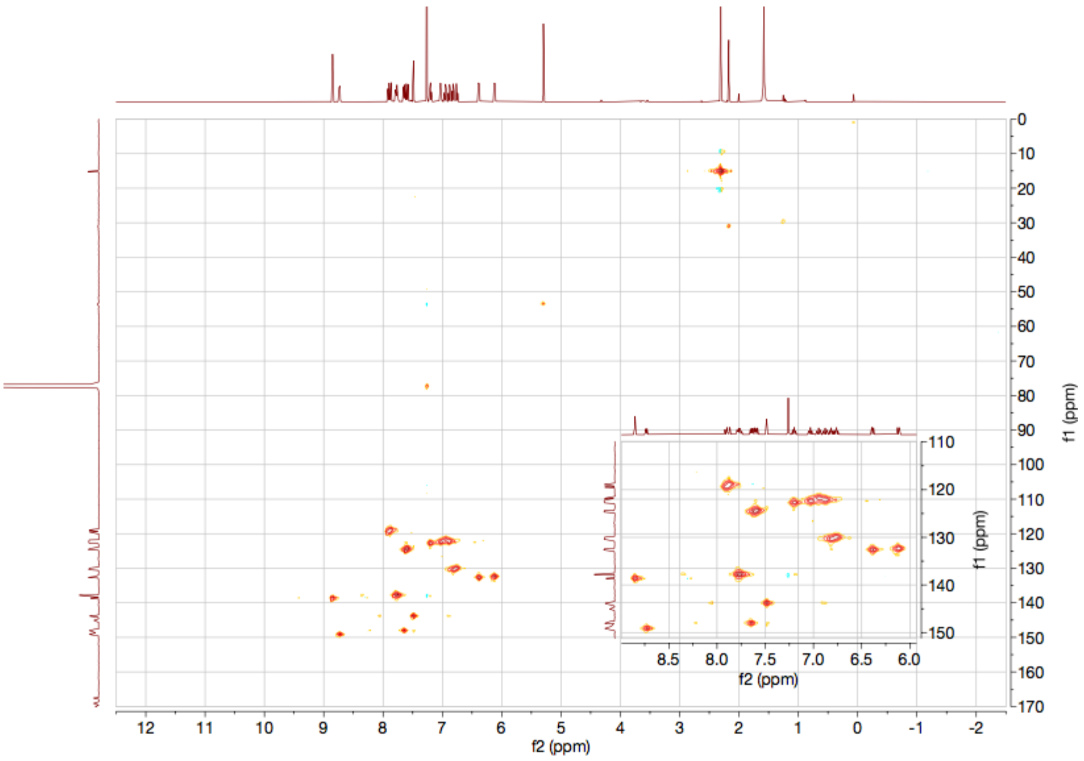

Figure 11:HSQC Spectrum of 7b CDCl3

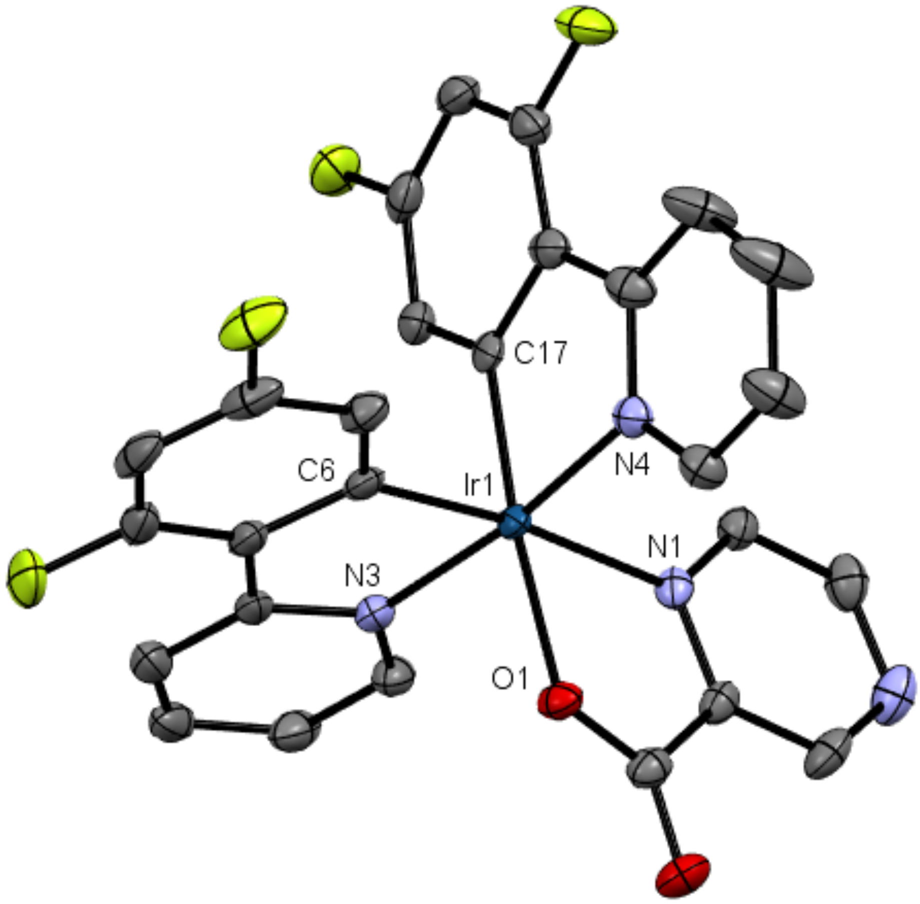

Figure 12: Single crystal X-ray crystal structure of complex 5. Hydrogen atoms and solvent molecules omitted for clarity.

Table 1: Crystal data and structure refinement for complex 5

Identification code	d8-5402-C27H15F4IrN4O2-CIF
Empirical formula	$C_{27}H_{15}F_4IrN_4O_2$
Formula weight	695.63
Temperature/K	100(2)
Crystal system	triclinic
Space group	P-1
a/Å	8.8150(6)
b/Å	12.0339(10)
c/Å	22.3146(17)
α/°	87.528(3)
β/°	79.542(3)
γ/°	89.854(3)
Volume/Å^3	2325.6(3)
Z	4
ρ_{calc}g/cm^3	1.987
μ/mm^{-1}	5.808
F(000)	1336.0
Crystal size/mm^3	0.122 × 0.081 × 0.077
Radiation	MoKα (λ = 0.71073)
2Θ range for data collection/°	4.7 to 52.998
Index ranges	$-11 \leq h \leq 11$, $-15 \leq k \leq 15$, $-28 \leq l \leq 28$
Reflections collected	81813
Independent reflections	9631 [R_{int} = 0.0475, R_{sigma} = 0.0234]
Data/restraints/parameters	9631/0/685
Goodness-of-fit on F^2	1.191
Final R indexes [I>=2σ (I)]	R_1 = 0.0214, wR_2 = 0.0419
Final R indexes [all data]	R_1 = 0.0283, wR_2 = 0.0464
Largest diff. peak/hole / e Å^{-3}	1.22/-0.94

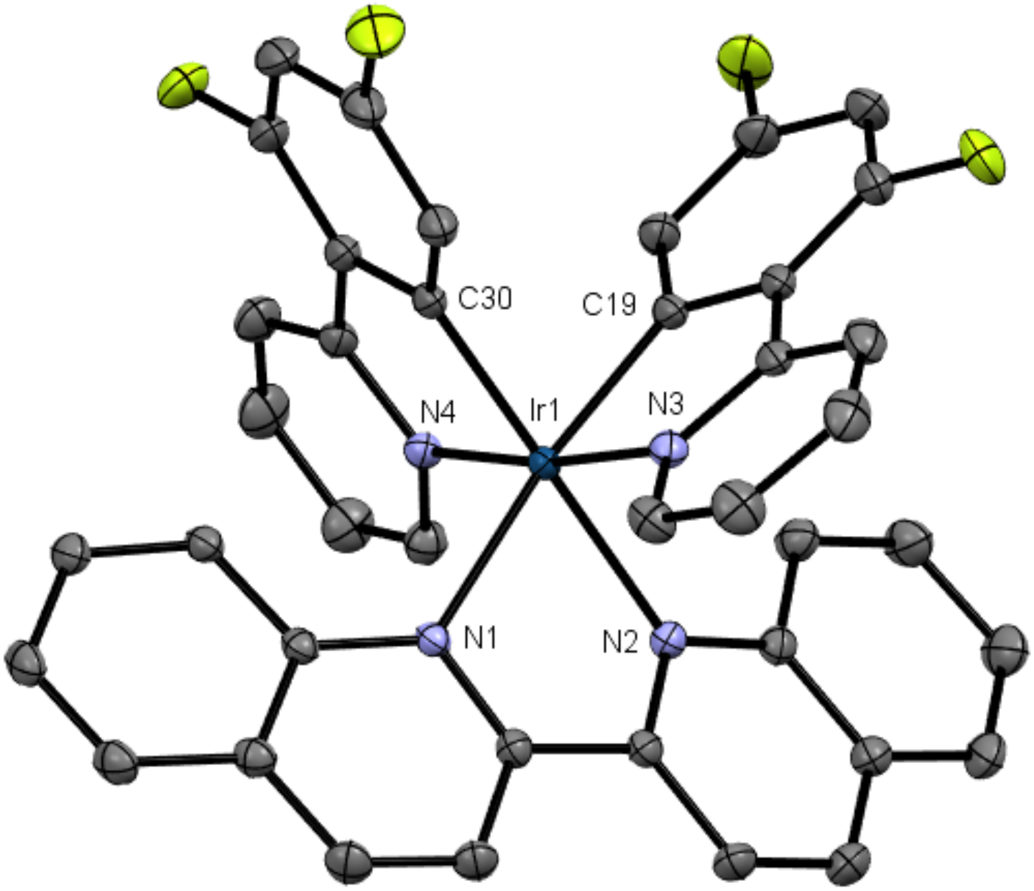

Figure 13: Single Crystal X-ray crystal structure of complex 1. Hydrogen atoms and solvent molecules omitted for clarity.

Table 2: Crystal data and structure refinement for complex 1

Identification code	d8-5322-C40H24N4F4Ir-PF6-2CH2Cl2
Empirical formula	$C_{42}H_{28}Cl_4F_{10}IrN_4P$
Formula weight	1143.65
Temperature/K	100(2)
Crystal system	monoclinic
Space group	$P2_1/n$
a/Å	9.9245(4)
b/Å	30.5895(13)
c/Å	13.5866(6)
α/°	90
β/°	98.3863(16)
γ/°	90
Volume/Å^3	4080.6(3)
Z	4
ρ_{calc}g/cm^3	1.862
μ/mm^{-1}	3.658
F(000)	2232.0
Crystal size/mm^3	0.184 × 0.172 × 0.091
Radiation	MoKα (λ = 0.71073)
2Θ range for data collection/°	4.356 to 59.22
Index ranges	$-13 \le h \le 13$, $-42 \le k \le 42$, $-18 \le l \le 18$
Reflections collected	104178
Independent reflections	11441 [$R_{int} = 0.0423$, $R_{sigma} = 0.0207$]
Data/restraints/parameters	11441/0/559
Goodness-of-fit on F^2	1.096
Final R indexes [I>=2σ (I)]	$R_1 = 0.0230$, $wR_2 = 0.0513$
Final R indexes [all data]	$R_1 = 0.0276$, $wR_2 = 0.0545$
Largest diff. peak/hole / e Å^{-3}	1.48/-1.58

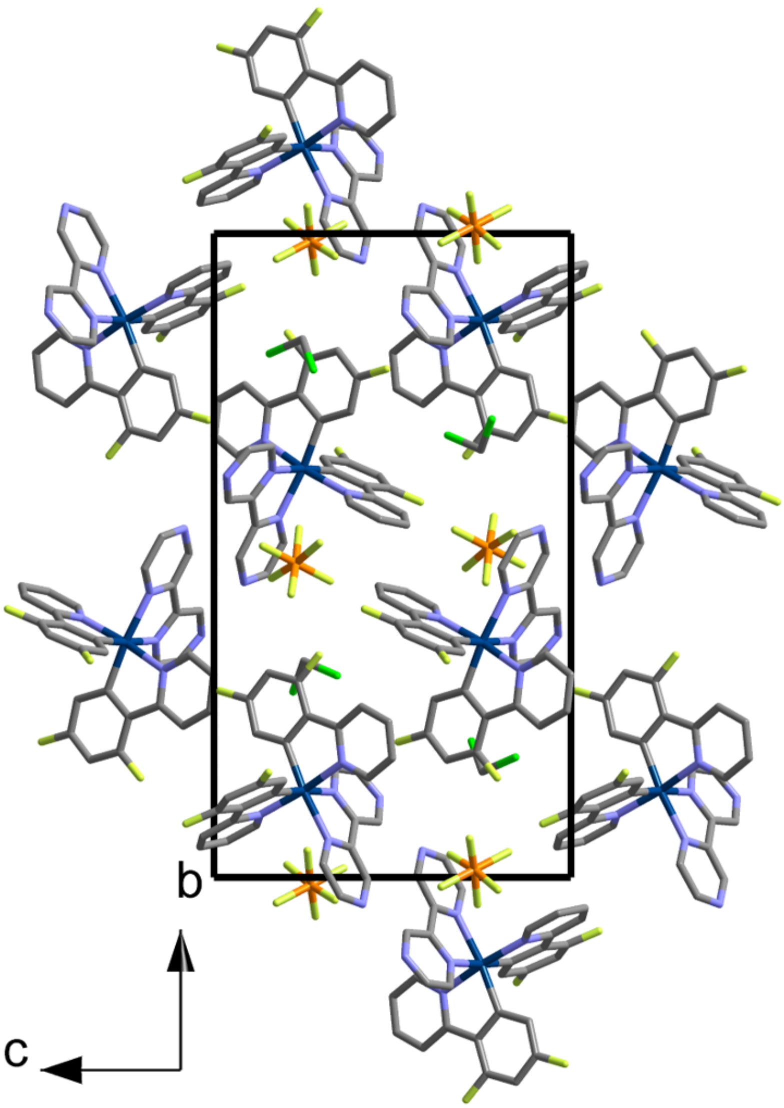

Figure 14: Crystal Structure of attempted N-oxide reaction of complex 2b. Hydrogen atoms and solvent molecules omitted for clarity. Only the packing structure of this complex was able to be refined.

Table 3: Crystal data and structure refinement for complex 2b	
Identification code	d8-5375_a-C30H18F4IrN6-PF6-CH2Cl2
Empirical formula	$C_{31}H_{20}Cl_2F_{10}IrN_6P$
Formula weight	960.60
Temperature/K	100(2)
Crystal system	monoclinic
Space group	$P2_1/c$
a/Å	9.6985(8)
b/Å	24.7164(18)
c/Å	13.7261(9)
α/°	90
β/°	93.775(3)
γ/°	90
Volume/$Å^3$	3283.2(4)
Z	4
$\rho_{calc}g/cm^3$	1.943
μ/mm^{-1}	4.370
F(000)	1856.0
Crystal size/mm^3	0.173 × 0.112 × 0.033
Radiation	MoKα (λ = 0.71073)
2Θ range for data collection/°	4.208 to 50.998
Index ranges	$-11 \leq h \leq 11$, $-29 \leq k \leq 29$, $-16 \leq l \leq 16$
Reflections collected	56722
Independent reflections	6099 [$R_{int} = 0.0468$, $R_{sigma} = 0.0229$]
Data/restraints/parameters	6099/0/460
Goodness-of-fit on F^2	1.067
Final R indexes [I>=2σ (I)]	$R_1 = 0.0409$, $wR_2 = 0.0865$
Final R indexes [all data]	$R_1 = 0.0498$, $wR_2 = 0.0938$
Largest diff. peak/hole / e $Å^{-3}$	1.81/-1.15

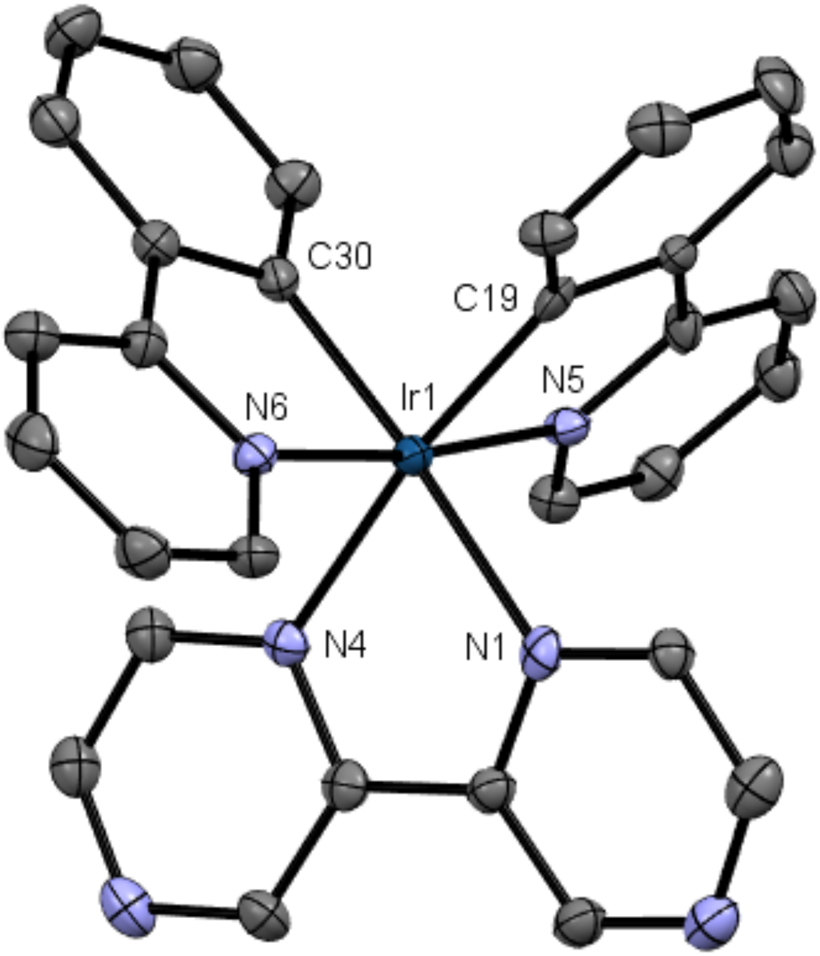

Figure 15: Single-crystal X-ray crystal structure of complex 3. Hydrogen atoms and solvent molecules omitted for clarity.

Table 4: Crystal data and structure refinement for complex 3

Identification code	d8-5346-C30H22IrN6-PF6
Empirical formula	$C_{30}H_{22}F_6IrN_6P$
Formula weight	803.70
Temperature/K	100(2)
Crystal system	orthorhombic
Space group	Pbca
a/Å	10.8324(4)
b/Å	16.0987(6)
c/Å	31.5748(10)
α/°	90
β/°	90
γ/°	90
Volume/Å^3	5506.3(3)
Z	8
ρ_{calc}g/cm^3	1.939
μ/mm^{-1}	4.983
F(000)	3120.0
Crystal size/mm^3	0.137 × 0.122 × 0.056
Radiation	MoKα (λ = 0.71073)
2Θ range for data collection/°	4.712 to 51.998
Index ranges	$-13 \le h \le 13$, $-19 \le k \le 19$, $-38 \le l \le 38$
Reflections collected	53413
Independent reflections	5404 [R_{int} = 0.0576, R_{sigma} = 0.0273]
Data/restraints/parameters	5404/0/397
Goodness-of-fit on F^2	1.219
Final R indexes [I>=2σ (I)]	R_1 = 0.0319, wR_2 = 0.0599
Final R indexes [all data]	R_1 = 0.0478, wR_2 = 0.0707
Largest diff. peak/hole / e Å^{-3}	2.74/-1.65

Appendix B: Additional Rhenium Spectra

As mentioned previously, the compounds detailed in this report were new compounds without published NMR spectra and crystal structures. Thus, much of the data shown here and in the main chapters will be further analyzed for future publications. The NMR spectra and crystal structures shown are important for future analysis, but for conciseness they were omitted from the main Results and Discussion.

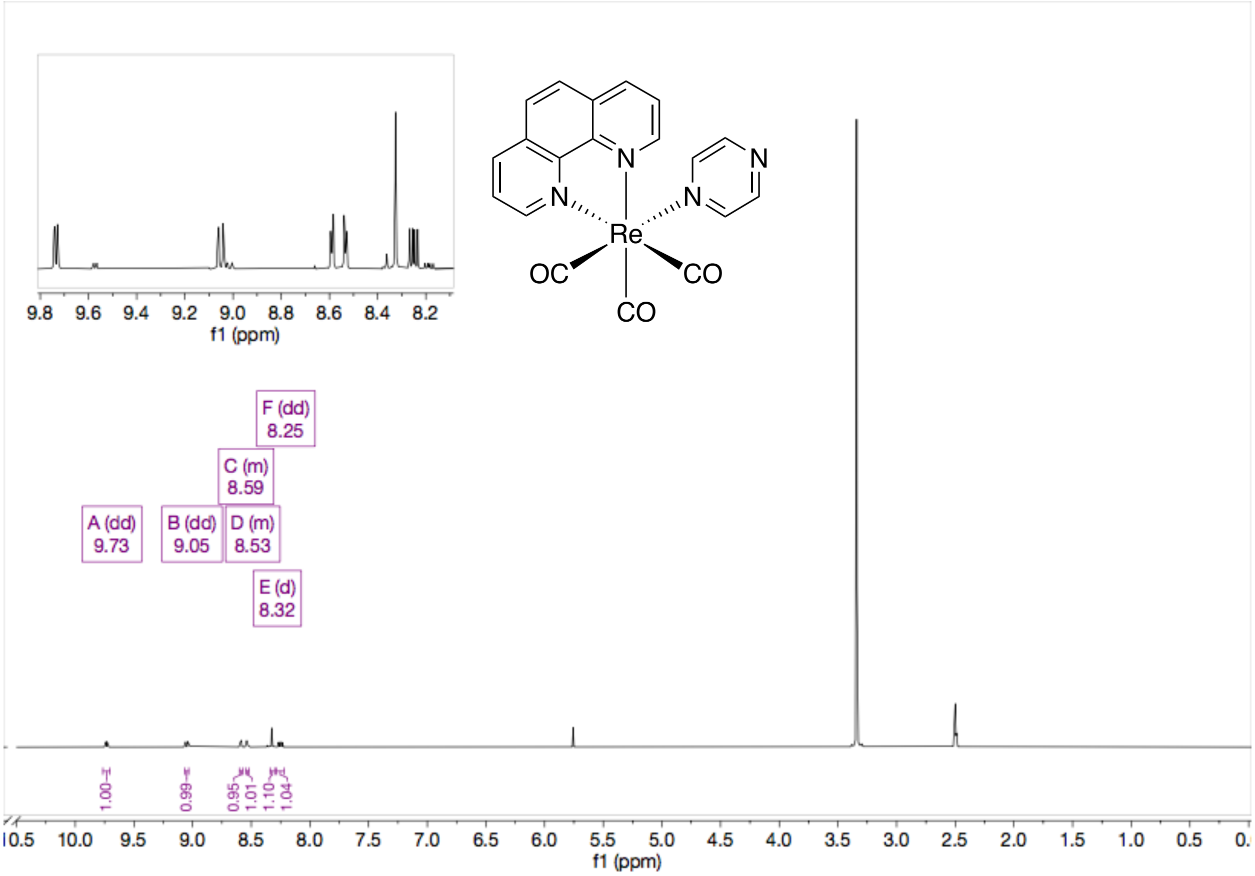

Figure 1: Re(CO)$_3$(phen)(pz) in d6-DMSO

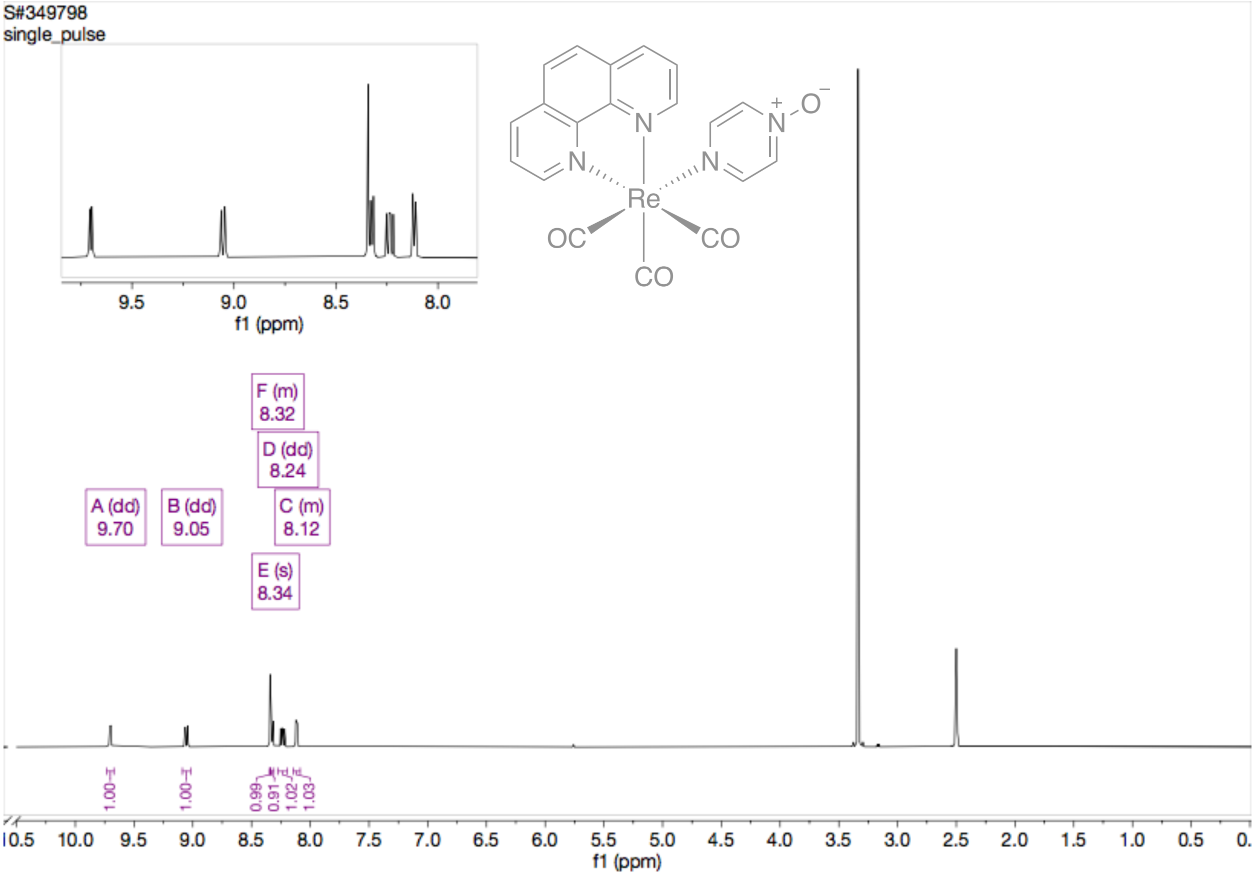

Figure 2: NMR of Re(CO)$_3$(phen)(pz-O) in d6-DMSO

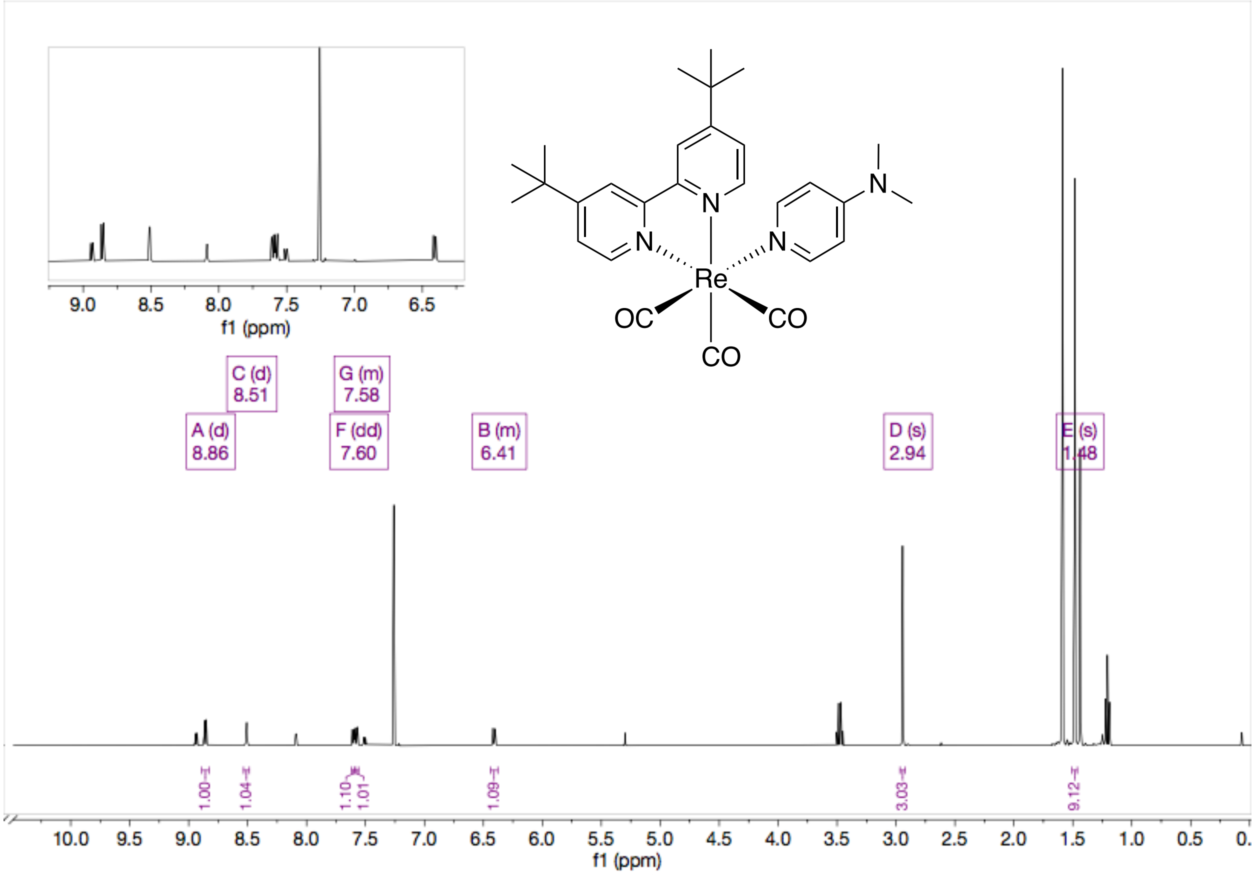

Figure 3: NMR of Re(CO)3(^{t}bbpy)(DMAP) in CDCl$_3$

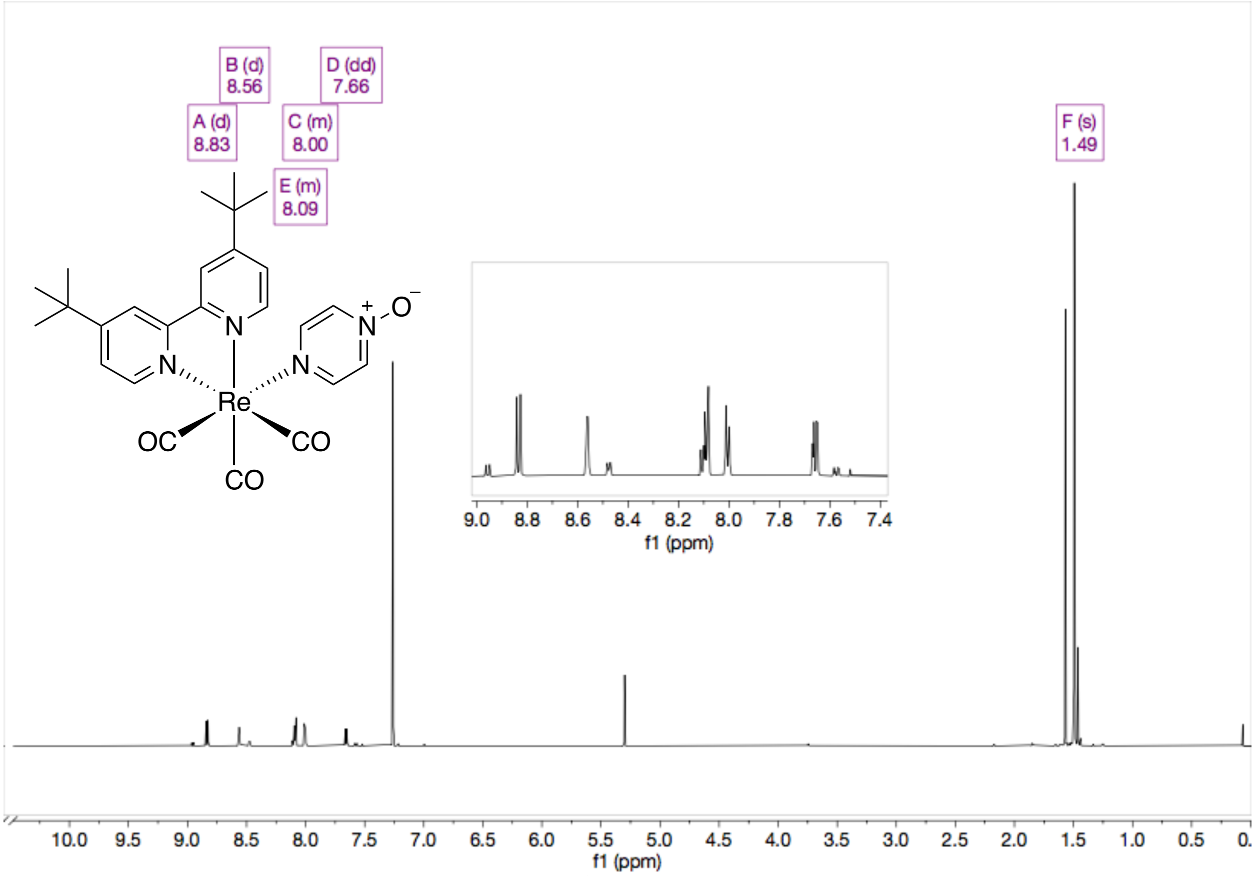

Figure 4: NMR of Re(CO)$_3$(^{t}bbpy)(pz-O) in CDCl$_3$ (Attempted)

Acknowledgements

Advisor

I would like to thank my thesis and research advisor, Dr. Jared Pienkos, for the opportunity to work on this project and continue research since the Fall of 2020. I have learned so much, but I also have been challenged to become a more independent scientist. The skills and passion for research I have gained throughout this project were instrumental in my decision to attend graduate. Undergraduate research has been the highlight of my time at UTC.

Faculty

I would like to thank Dr. James Patton for assisting me with much of the analytical data collection detailed in this report through both class instruction and individual training. I would also like to thank Dr. Colin McMillen at Clemson University for all of his help with crystal structure determination.

Students

There are many students that I could thank for general encouragement and comraderie during my undergraduate research experience, but, I would like to especially acknowledge Sarah McDarmont, India Toth, Bre-Anna Willis, and Brandon Nessell for their contributions to this project.

Funding

SEARCH Grant

RCA Award

Grote Endowment